BAŞKENT UNIVERSITY
INSTITUTE OF SCIENCE AND ENGINEERING
DEPARTMENT OF BIOMEDICAL ENGINEERING
DOCTOR OF PHILOSOPHY IN BIOMEDICAL ENGINEERING

SEGMENTATION ON BRAIN MR IMAGES BY USING DEEP LEARNING
NETWORK AND 3D MODELLING

BY

GÖKAY KARAYEĞEN

DOCTOR OF PHILOSOPHY THESIS

ANKARA - 2021

BAŞKENT UNIVERSITY
INSTITUTE OF SCIENCE AND ENGINEERING
DEPARTMENT OF BIOMEDICAL ENGINEERING
DOCTOR OF PHILOSOPHY IN BIOMEDICAL ENGINEERING

**SEGMENTATION ON BRAIN MR IMAGES BY USING DEEP LEARNING
NETWORK AND 3D MODELLING**

BY

GÖKAY KARAYEĞEN

DOCTOR OF PHILOSOPHY THESIS

ADVISOR

ASSOC. PROF. DR. MEHMET FEYZİ AKŞAHİN

ANKARA - 2021

BAŞKENT UNIVERSITY

INSTITUTE OF SCIENCE AND ENGINEERING

This study, which was prepared by Gökay Karayeğen has been approved in partial fulfillment of the requirements for the degree of DOCTOR OF PHILOSOPHY in Biomedical Engineering Department by the following committee.

Date of Thesis Defense: 10 / 06 / 2021

Thesis Title: Segmentation On Brain MR Images By Using Deep Learning Network And 3d Modelling

Examining Committee Members	**Signature**
Prof. Dr. Mustafa DOĞAN (Chairman)	……………………
Assoc. Prof. Dr. Mehmet Feyzi AKŞAHİN (Member /Advisor)	……………………
Assoc. Prof. Dr. Derya YILMAZ (Member)	……………………
Assist. Prof. Dr. Emre SÜMER (Member)	…………………….
Assist. Prof. Dr. Erdem Orhan HABERAL (Member)	…………………….

APPROVAL

Prof. Dr. Ömer Faruk ELALDI

Director, Institute of Science and Engineering

Date: … / … /2021

BAŞKENT ÜNİVERSİTESİ
FEN BİLİMLER ENSTİTÜSÜ
DOKTORA TEZ ÇALIŞMASI ORİJİNALLİK RAPORU

Tarih:08 /06/ 2021

Öğrencinin Adı, Soyadı : Gökay KARAYEĞEN

Öğrencinin Numarası : 21520112

Anabilim Dalı : Biyomedikal Mühendisliği

Programı : Doktora

Danışmanın Unvanı/Adı, Soyadı : Doç. Dr. Mehmet Feyzi AKŞAHİN

Tez Başlığı : Derin Öğrenme ile Beyin MR Görüntüleri Üzerinde Segmentasyon ve 3 Boyutlu Modelleme

Yukarıda başlığı belirtilen Yüksek Lisans/Doktora tez çalışmamın; Giriş, Ana Bölümler ve Sonuç Bölümünden oluşan, toplam 93 sayfalık kısmına ilişkin, 08/06/2021 tarihinde şahsım tarafından Turnitin adlı intihal tespit programından aşağıda belirtilen filtrelemeler uygulanarak alınmış olan orijinallik raporuna göre, tezimin benzerlik oranı % 18'dir. Uygulanan filtrelemeler:

1. Kaynakça hariç
2. Alıntılar hariç
3. Beş (5) kelimeden daha az örtüşme içeren metin kısımları hariç

"Başkent Üniversitesi Enstitüleri Tez Çalışması Orijinallik Raporu Alınması ve Kullanılması Usul ve Esaslarını" inceledim ve bu uygulama esaslarında belirtilen azami benzerlik oranlarına tez çalışmamın herhangi bir intihal içermediğini; aksinin tespit edileceği muhtemel durumda doğabilecek her türlü hukuki sorumluluğu kabul ettiğimi ve yukarıda vermiş olduğum bilgilerin doğru olduğunu beyan ederim.

Öğrenci İmzası:

ONAY

08 /06 /2021

Doç. Dr. Mehmet Feyzi AKŞAHİN

ACKNOWLEDGEMENT

ABSTRACT

Gökay KARAYEĞEN

SEGMENTATION ON BRAIN MR IMAGES BY USING DEEP LEARNING NETWORK AND 3D MODELING

Başkent University Institute of Science and Engineering

Department of Biomedical Engineering

2021

In the last few years, utilizing deep learning techniques for predicting tumor presence on brain MR images became quite common.We offer a semantic segmentation method that uses a convolutional neural network to autonomously segment brain tumors on 3D Brain Tumor Segmentation (BraTS) image data sets using four different imaging modalities in this research (T1, T1C, T2, and Flair). In addition, our research incorporates whole-brain 3D imaging and a comparison of ground truth and anticipated labels in 3D. This method was effectively applied to acquire specific tumor regions and measurements such as height, width, and depth, and images were presented in various planes including sagittal, coronal, and axial. In terms of tumor prediction, the evaluation findings of semantic segmentation performed by a deep learning network are extremely promising. The average prediction ratio was found to be 91.718. The mean IoU (Intersection over Union) score was 86.946 and the mean BF score was 92.938. Finally, the test images' dice scores revealed a considerable resemblance between the ground truth and predicted labels. As a result, semantic segmentation metrics and 3D imaging can both be viewed as useful for effectively diagnosing brain tumors. Calculating the surface areas of the brain, real and predicted labels, and applying this process to all slices is very useful in terms of comparing tumor volume information. As a result, the predicted volume values are very close to the ground truth volume values, showing that this study can determine the presence of tumors by the deep learning method and tumor size by surface area algorithm. In addition, the calculation of the brain tumor volume and 3D modeling will facilitate clear visualization of the tumor site and understanding the size of the tumor.

KEYWORDS: Semantic segmentation, deep learning network, 3D imaging, surface area calculation, volume of tumor

ÖZET

Gökay KARAYEĞEN
DERİN ÖĞRENME İLE BEYİN MR GÖRÜNTÜLERİ ÜZERİNDE SEGMENTASYON VE 3B MODELLEME
Başkent Üniversitesi Fen Bilimleri Enstitüsü
Biyomedikal Mühendisliği Anabilim Dalı
2021

Son yıllarda beyin MR görüntülerinde, tümör varlığının tahmin edilebilmesi için derin öğrenme tekniklerinin kullanımı oldukça yaygınlaşmıştır.Dört farklı görüntüleme modalitesinden (T1, T1C, T2 ve Flair) oluşan 3D Beyin Tümörü Segmentasyonu (BraTS) görüntü veri setlerinde beyin tümörünü otomatik olarak bölümlere ayırmak için konvolüsyonlu sinir ağını kullanarak semantik segmentasyon yöntemi sunulmaktadır. Ek olarak, piksel sınıflandırılması için 'arka plan' ve 'tümör' olmak üzere iki sınıf belirlenmiştir. Semantik segmentasyon sonuçlarının değerlendirilmesi için de ortalama IoU ve ortalama BFscore gibi metriklerden faydalanılmıştır. Ayrıca, kullanılan veri setindeki gerçek (ground truth) etiketleri ile oluşturulan ağın son katmanında elde edilen tahmin etiketlerinin karşılaştırılması, dice katsayısı kullanılarak karşılaştırılmıştır. Her iki etiket grubu kullanılarak, içerisinde tümörün yer aldığı 3 boyutlu beyin MR görüntüleri oluşturulmuştur. Sonuç olarak, test görüntüsü üzerinde yüksek oranda tümör tahmini gerçekleştirilmiştir. Oluşturulan 3 boyutlu beyin görüntüleri, tümörün genişlik, yükseklik ve derinliği hakkında cerrahlara planlama açısından görsel bir katkı sağlayabilir. Beyin, gerçek ve tahmin edilen etiketlerin yüzey alanlarının hesaplanması ve bu işlemin bütün kesitlere uygulanması tümör hacim bilgilerinin karşılaştırılması anlamında oldukça faydalıdır. Sonuç olarak tahmin edilen hacim değerlerinin, gerçek hacim değerlerine oldukça yakın olması, bu çalışmanın tümör varlığını derin öğrenme metodu ile tümör hacmin ise yüzey alanı algoritması ile tespit edilebileceğini göstermiştir. Bu çalışma, beyin tümörlerinin otomatik olarak tespit edilmesini sağladığı için, beyin tümör teşhislerinde önemli bir avantaj sağlayabilir. Ek olarak, beyin tümörünün hacminin hesaplanması ve 3 boyutlu modelleme sayesinde, tümör bölgesinin net olarak görüntülenmesi ve tümörün boyutlarının anlaşılmasını kolaylaştıracaktır.

ANAHTAR KELİMLER: Beyin tümörü, semantik segmentasyon, derin öğrenme, 3 boyutlu görüntüleme, yüzey alanı hesaplama, tümör hacmi

TABLE OF CONTENTS

LIST OF FIGURES

Page

LIST OF TABLES

LIST OF ABBREVIATIONS

CT	Computed Tomography
MRI	Magnetic Resonance Imaging
PET-CT	Positron Emission Tomography-Computed Tomography
AR	augmented reality
ROI	Region of Interest
CNN	convolutional artificial neural network
T1	native
T1C	post-contrast T1-weighted
T2	T2-weighted
Flair	T2 Fluid Attenuated Inversion Recovery
NIfTI	Neuroimaging Informatics Technology Initiative
BRATS	Brain Tumor Segmentation
DCNN	Deep Convolutional Neural Network
GBM	glioblastoma multiforme
ALU	arithmetic logic unit
RBMs	restricted Boltzman model
RNNs	recurrent neural networks
ReLU	the linear unit
DRN	deep residual network
VGG	Visual Geometry Group
SGD	stochastic gradient descent
TP	True Positive
FP	False Positive
TN	True Negative
P	Positive
N	Negative
IoU	Intersection over Union

1.INTRODUCTION

Medical imaging provides important research interest and healthcare solutions with image-based applications. Therefore, it is a quite effective field study in terms of diagnosing critical diseases. In addition, medical images have a significant role in surgical planning, radiotherapy and training purposes [1]. To analyze medical images, recent developments in image processing and computer vision technologies offer so many implementations for healthcare systems [2].

Well-known techniques used for image acquisition in biomedical imaging; computed tomography (CT), magnetic resonance imaging (MRI), x-ray, molecular imaging, ultrasonography, photo-acoustic imaging, fluoroscopy, and positron emission tomography-computed tomography (PET-CT) [3]. According to the literature research [4], although the application of deep learning techniques to analyze the images obtained with these techniques has become widespread in recent years, considering the number of publications, studies on MRI, CT, and microscopy is more common. In addition, there are some new technologies to analyze medical images such as virtual and augmented reality.

The images obtained by different medical imaging methods by using augmented reality (AR) technology are important in terms of increasing the accuracy of diagnosis of many diseases and providing radiographic quality. Augmented reality shows the virtual image and real user environment at the same time utilizing viewer tools placed on the head. As far as medical applications are concerned, when situations such as medical imaging that require pre-planning, intraoperative imaging, and physical examination are needed, the real-world view can be the patient's own body [5].

Important stages in the processing of a digital image start with the image acquisition and then continue with processes such as image enhancement, correction, morphological processing, segmentation, object recognition, display and identification, color image processing, and image compression. When it comes to image processing, the image segmentation technique is an important research area due to its wide area of use and applications. The main purpose of image segmentation techniques is to detect objects in an image or to classify an image with different regions and parts [6]. Segmentation aims to divide the pixels contained in an image into groups that are strongly correlated with the objects in the image [7]. One of the most important tasks in biomedical imaging is segmentation. By dividing a medical image into segments, it allows further investigations to be studied in diseases [8]. By dividing a digital image into multiple

segments, it enables the identification of the region of interest in the image (ROI - Region of Interest) or obtaining other relevant information [9]. In the field of medicine, common features obtained after segmentation applied to images generally consist of elements belonging to the same type of tissue or organ. It is a key facilitating technology for medical applications such as segmentation, diagnostics, planning, and routing applied to anatomical structures [10]. In the last few years, these types of image processing techniques began to be applied by deep learning systems with artificial neural networks.

Deep learning approaches have a significant impact on the prediction of tumor existence when medical image segmentation is conducted on MR brain images. Manual segmentation of a brain tumor is a time-consuming procedure that relies on doctors' knowledge and experience. A brain tumor can develop as a result of cancerous or non-cancerous aberrant cell proliferation in the brain, and it can be classed as benign or malignant. Active cells are absent from benign tumors, and they are homogeneous. Active cells are found in malignant tumors, which lack uniformity. [11,12]. There are two types of brain tumors: basic and metastatic (spreading). While basic brain tumors contain brain cells, malignant cells travel to the brain from another afflicted body area in metastatic tumors. Glioma is the most common form of tumor and can range in severity from high-grade glioblastoma to low-grade oligodendroglioma or astrocytoma [13].

1.1. The subject of the study

A benign or malignant brain tumor develops as a result of cancerous or non-cancerous growths of aberrant cells in the brain. Benign tumors are characterized by a uniform structure and the absence of active cells. Malignant tumors are inhomogeneous and include active malignant cells [14,15].

Primary brain tumors and metastatic brain tumors are the two types of brain cancers. Cells are primarily brain cells when it comes to initial brain tumors. Cancerous cells spread from the contaminated bodily part to the brain in metastatic tumors, on the other hand. Gliomas are the most common type of tumor and are classed as high-grade or low-grade tumors[12].

The primary goal of computer-assisted brain tumor diagnosis is to acquire unique clinical information about the tumor's location, existence, and type. It involves methods including segmentation, tumor detection, and classification, as well as the diagnosis of a brain tumor using MR images using software-based applications. Deep learning algorithms are increasingly being used to diagnose brain cancers with greater accuracy and reliability [16].

Although magnetic resonance imaging (MRI) is a useful tool for properly depicting brain structure, factors such as limited spatial resolution, low contrast, inhomogeneity, noise, and object forms have made medical image segmentation a challenge. As a result, completing a good segmentation is critical for making more accurate diagnoses of brain diseases[17,18,19].

For medical image segmentation, a variety of computer-assisted approaches are available. Threshold-based, zone-based, mode-based, and neural network techniques are among them. CNN (convolutional artificial neural network), one of the deep learning approaches, is highly successful for medical segmentation applications in terms of offering high segmentation accuracy, according to current research [20,21,22]. Convolution in deep learning is driven by a multilayer neural network, which has several hidden layers and free parameters. Each MRI input image passes through a series of convolution layers, pooling layers, filters, fully connected layers, and a function for the final decision-making process with this system [23].

In this study, the main objective is to create segmentation algorithms for image processing by using folded artificial neural networks on brain MR images obtained with the MR device, to increase the diagnostic accuracy on these images with the help of artificial intelligence, and to display them with augmented reality technology.

1.2. Contribution of the study

Accurate diagnosis of diseases is vital in medical imaging. A brain tumor is a life-threatening disease that occurs in the human brain. In recent years, deep learning applications have been used for the automatic detection of brain tumors. Contributions of this study include diagnosis with as high accuracy as possible with automatic brain tumor segmentation and 3D imaging of the tumor and calculation of its volume. Thus, it is possible to examine the brain tumor in detail both visually and numerically. These analyzes provide detailed information about the region of the brain tumor and its dimensions, including width, height, and depth. 3D imaging and volume calculation can facilitate diagnosis or surgical planning.

1.3. Content of the study

BRATS (Brain Tumor Segmentation) image data containing MRI brain images on four different modalities were used as the data set. This dataset was downloaded from the website 'http://medicaldecathlon.com/'. There are four different modalities in MR images for each brain image. These are T1 (native), T1C (post-contrast T1-weighted), T2 (T2-weighted), and Flair (T2 Fluid Attenuated Inversion Recovery) [30]. Each MR modality plays a different role in diagnosis. Edema regions are represented on T2 images. Healthy tissues can be distinguished

on T1 images. T1C images are used to distinguish the tumor margin. In addition, edema regions can be distinguished from spinal fluid on FLAIR images [31].

In this study, both preprocessing techniques were applied to all these modalities mentioned and it was aimed to classify the tumors with semantic segmentation technique after being used as input in the deep-learning network. In addition, by applying the semantic segmentation technique with the artificial neural networks used in this study, tumor detection in MR brain images is desired. In this context, the MR image is divided into 2 different class labels as 'background' and 'tumor'.

After the BRATS dataset was downloaded and recorded in folders on a computer, it was read into MATLAB by using proper commands. This type of data has a file format of NIfTI and can be defined as Neuroimaging Informatics Technology Initiative. It uses a single or dual file storage format including (1) a header file (.hdr) involving the metadata and a data file (.img) containing image data and (2) a single file (.nii), which comprises header information followed by image data [32]. The used BRATS brain MR image data includes 257 images and 257 pixel-tag images in total. MR images are 240 * 240 in size and each contains 155 slices.

257 BRATS image data sets were utilized to train the deep learning network utilizing semantic segmentation in this study. Training, validation, and test images were used to predict labels and compare them to ground-truth labels in order to apply semantic segmentation with a deep learning approach. After the training process was completed, 5 different data sets consisting of 155 MR slices per image with tumors were used. Also, 10 different validation data sets were used in the training process.

The main goal is to use 3D MR images and by using the Deep Learning Toolbox feature of MATLAB, training the computer through artificial neural networks, and performing tumor diagnosis in these 3D images, and increasing the diagnostic accuracy percentage.

Furthermore, 3D models were constructed and cropped using MATLAB's 3D image cropping function to better grasp the tumor's entire territory. These images were displayed in three imaging planes: coronal, sagittal, and axial. Furthermore, different type of displays was created which show the brain tumor as a volume inside the brain. These represent the location of the tumor and provide specific information about tumor sizes such as height, width, and depth.

1.4. Purpose of the study

A brain tumor is one of the most common and critical diseases which causes high mortality ratios among patients. It can be described as a group of abnormal cells that are inclined to grow inside and around the brain. These abnormal cells in the human brain can affect brain function structure and behavior. Diagnosing brain tumors accurately can prevent possible deaths and lead to proper treatment. In order to execute an effective brain cancer treatment, several factors such as classification of tumor type, region, dimensions, and borders should be considered [24]. Analyzing the characteristics of the desired region including tissues and tumors can be carried out with magnetic resonance imaging (MRI) technique by using automated applications [25]. MRI scan is a quite sensitive approach that is used to evaluate net magnetization. In brief, a circular coil is placed around the patient's head and it generates electromagnetic waves and transmitted inside the brain. Then, these waves are emitted and a receiver coil is used for measurement. For spatial localization of the signal, a gradient coil is used. Finally, reconstruction of the signal is carried out and a brain image is acquired [26].

For the purpose of analyzing medical images, image segmentation techniques were widely used and they are quite useful to distinguish anatomical structures such as lesions, a tumors from healthy tissues [27]. However, manual segmentation which can be classified as a traditional method is quite time-consuming and depends on physicians' experience. In this regard, to overcome such issues, deep learning networks became common applications recently due to their superiority comparing to manual image segmentation. Using these types of networks can provide more detailed information regarding medical image segmentation, detection, classification, registration, reconstruction, and quality evaluation [28,29].

This study aims to create segmentation algorithms for image processing by using convolutional artificial neural networks on brain MR images, to increase the diagnostic accuracy of these images with the help of artificial intelligence, and to display 3D. Accordingly, it was aimed to classify the tumors with semantic segmentation technique after using MR images as input in the deep-learning network. In addition, 3-dimensional imaging of the brain and tumor region by using segmentation MR sections and labels corresponding to these sections are among the targets.

1.5. Related Works

Several different studies on detecting brain tumors by segmentation of brain MRI images with deep learning techniques have been studied.

In the first study, automated brain tumor segmentation was performed on multi-modality MR images using the pre-trained artificial neural network SegNet. In this study, SegNet, a fully convolutional artificial neural network, was used to 3-dimensional data sets for four different MR modalities, T1, T1C, T2, and Flair, in order to detect brain cancers like necrosis, edema, and developing tumors with automatic segmentation. Separately trained SegNet models were combined with post-neural image processing techniques to further improve tumor segmentation. By integrating the feature map from the convolution layer, it is hoped to create four maximum feature maps. Following this, MR voxels were classified using the decision-making methodology to distinguish between tumor fragments and healthy brain tissue[33] (Figure 1.1). For the total tumor, tumor core, and developing tumor, the proposed methodology yielded three separate F-measure scores of 0.85, 0.81, and 0.79, respectively.
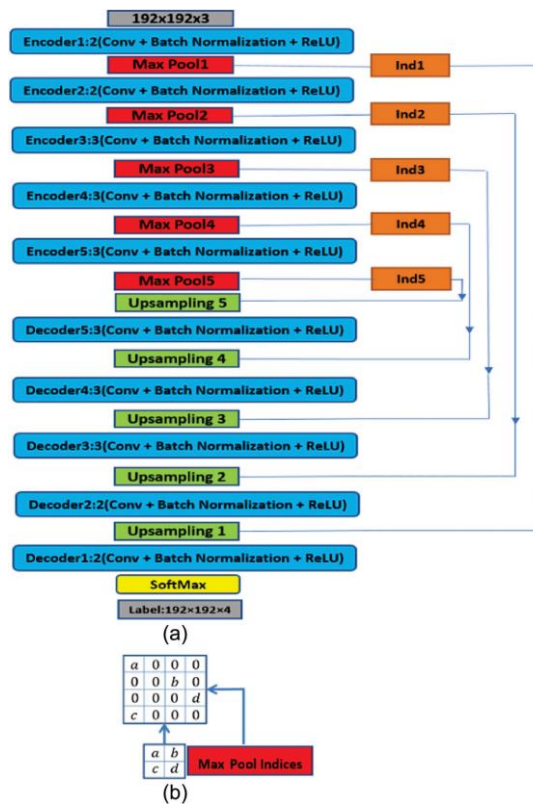
Figure 1.1. Architecture of SegNet [33]

Another study focuses on a model on brain tumor segmentation and prediction of survival rate, again using deep learning and multi-modal MR scans. For the implementation of tumor segmentation, 3 different 3D CNN structures were used to increase the performance of the artificial neural network [34] (Figure 1.2). A decision tree and cross-validation procedures were used to estimate survival after 4.524 radiomic features were retrieved from segmented tumor regions. Short-survivors, mid-survivors, and long-survivors were all classified with 61.0 percent accuracy using the model described.
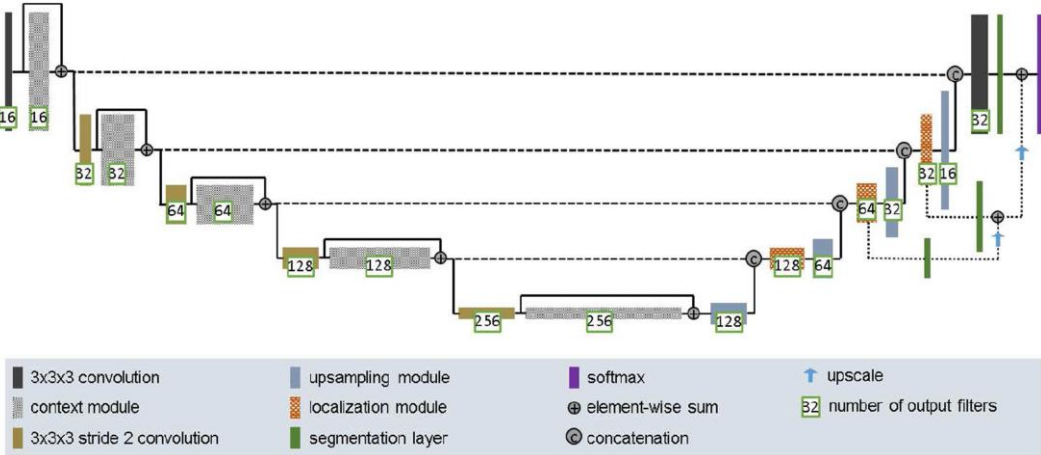
Figure 1.2. Structure of artificial neural network [34]

Another study showed a 3D U-Net structure for segmentation of identifiable subregions such as edema, necrosis, and developing tumor from a radiography view. A strategy is provided that includes weighted pieces from the tumor's border regions to alleviate the problem of class imbalance between tumor and non-tumor pieces/patches This particular structure has a contracting path for learning about the material and a symmetrically growing path for precise localization [35] (Figure 1.3). 285 MRI pictures were trained, validated on 66 patients, and tested on 191 patients using the Deep Convolutional Neural Network (DCNN). The suggested model's dice scores for the overall tumor, tumor core, and expanding tumor are 0.88, 0.83, and 0.75, respectively.

FLAIR
T1
T1ce
T2

Copy and Concatenate

Copy and Concatenate

Copy and Concatenate

Label

▷ 3 x 3 Convolution and Relu
▶ Max pool 2 x 2
▶ Up conv 2 x 2
▶ 1 x 1 Convolution and Relu
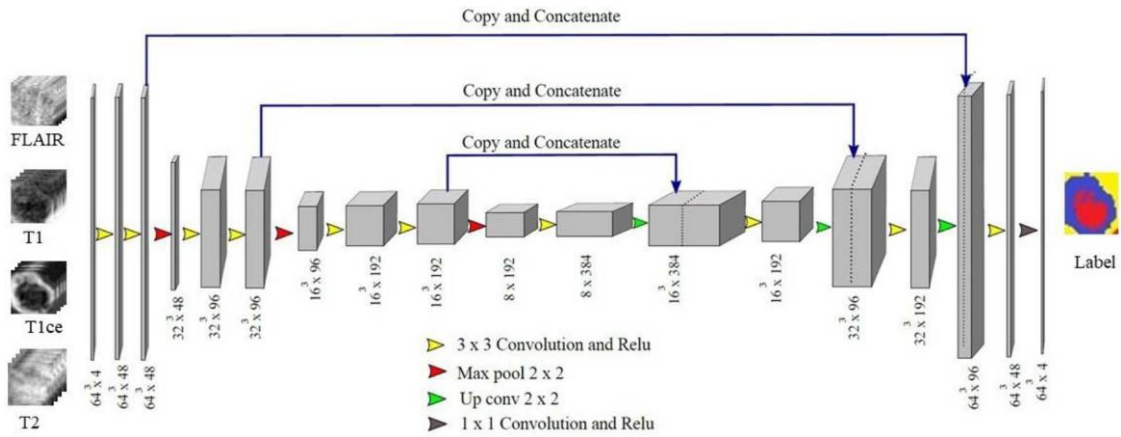
Figure 1.3. Flowchart of 3D U-Net [35]

Another study aimed to improve classification accuracy while lowering the danger of overfitting and allowing for multi-classification. As a result, the system comprises a regularized CNN structure and a modified softmax loss function. [36]. The Block diagram of this proposed system is shown in Figure 1.4. In comparison to other current systems, the proposed model has a greater accuracy of almost 2% and a processing time of 40-50 ms, according to the findings of this study. This approach is additionally influenced by issues such as binary classification, processing speed, and data overfitting.
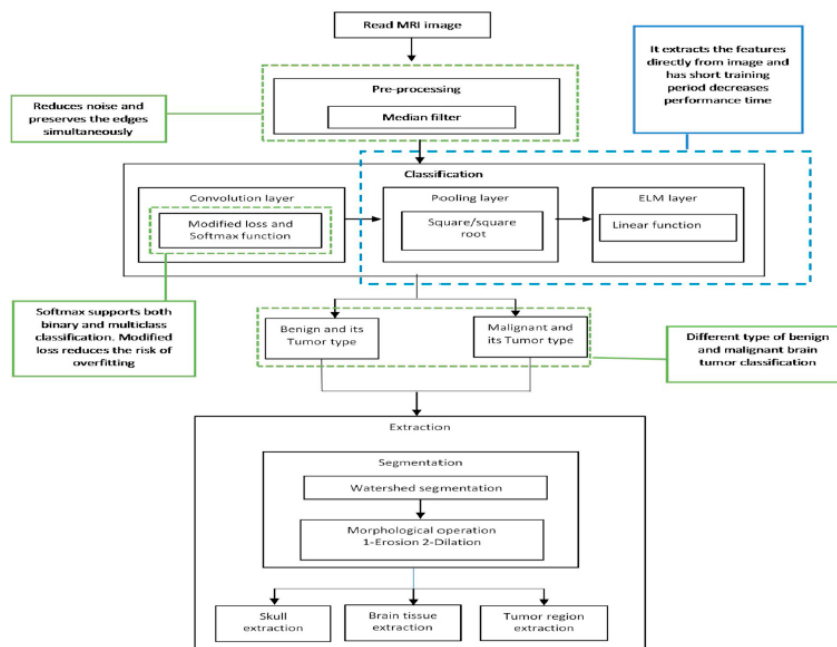
Figure 1.4. Block diagram of the proposed study [36]

Finally, in this study using the deep CNN technique, the prominent segmentation and error correction sections are combined. For processing input data with orthogonal sections, segmentation masks were created, and the erroneous tags were afterward repaired using the Replace and Refine networks. [37] (Figure 1.5). The average Dice value for this approach is 0.9015, and the necessary segmentation time for MRI volume is 14.8 seconds.
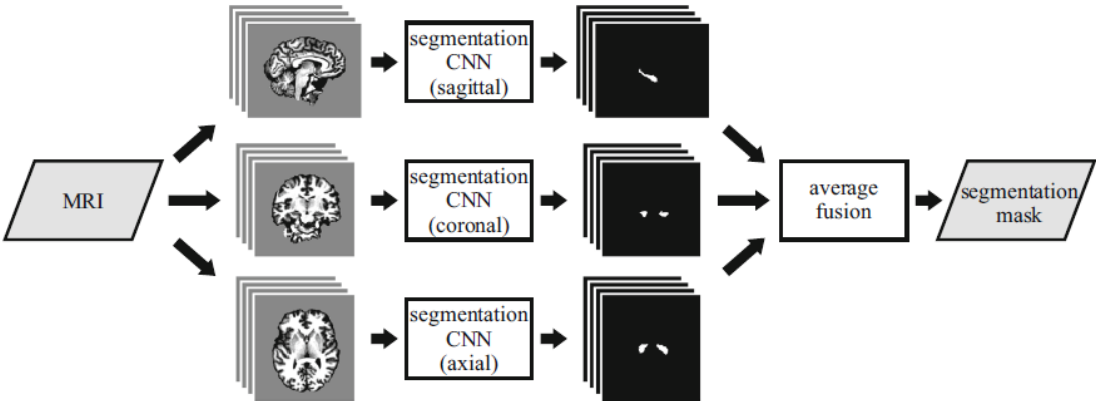
Figure 1.5. Segmentation module structure [37]

The next article proposes a machine learning-based computer-aided and fully automatic glioma brain tumor detection approach. The edges in the noise-removed image are discovered using fuzzy logic, and then contrast adaptive local histogram equalization is used to the edge-detected brain image to enhance the edge pixels. The Gabor transformation is applied to the enhanced brain image, and the features are determined and optimized using the feature optimization technique. The optimized sets are then classified using the ANFIS classification method, which divides the source brain MRI image into glioma and non glioma brain images. Finally, the tumor zones are segmented using the fuzzy C means algorithm on the glioma brain image. Figure 1.6 shows the suggested method's training model [95].
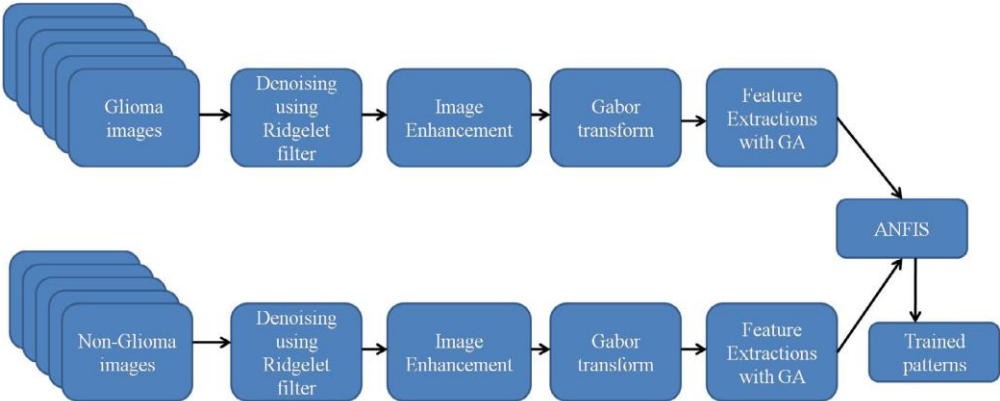
Figure 1.6. Training model for glioma prediction [95]

In the BRATS 2017 dataset, the proposed methodology accurately recognized 156 HGG (high-grade glioma) images out of 158 HGG brain images, with the tumor recognition rate for HGG being around 98.7%, and 55 LGG (low-grade glioma) out of 57 LGG brain pictures, with the TRR for LGG being around 96.4 percent [95].

Another study suggests that a generative adversarial network architecture to present an autonomous data augmentation methodology for synthesizing high-quality brain tumor images, allowing deep learning-based approaches to be trained more competently with the limited preprocessed samples. The tumor segmentation was done using a level set formulation and a geodesic active contour. Different modalities of magnetic resonance imaging brain images acquired from BRATS13 datasets were used to validate the suggested approach. The dice similarity coefficient was 0.942 in simulations, indicating improved performance. The related method is presented in Figure 1.7 [96].
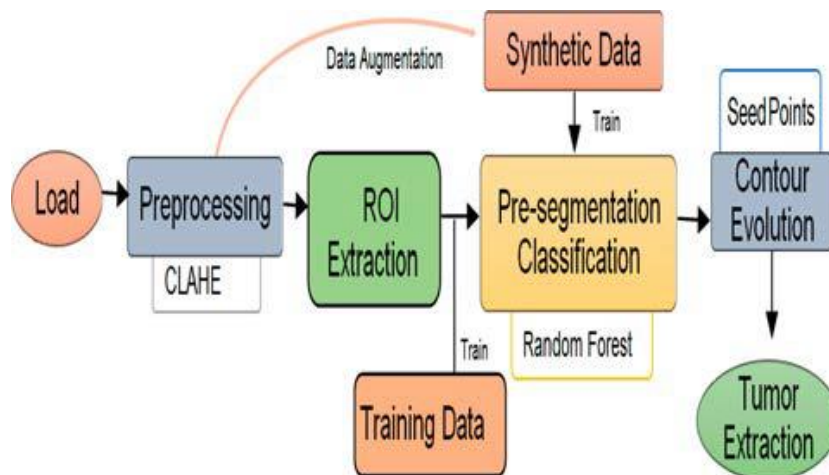
Figure 1.7. A generative adversarial network architecture [96]

Stochastic evolution is a basic data augmentation method that was presented (SE). The concept of SE is derived from our understanding of the degradation of sick tissue and the healing process. To imitate this natural process, the proposed method uses the picture warping technique's local distortion method. In other words, the diseased tissue's irregular deterioration and healing processes are replicated in accordance with the direction of the local distortion, resulting in a natural sample unrecognizable by humans. The proposed SE data augmentation strategy improves the segmentation accuracy of breast masses, prostate, brain tumors, and lung nodules, according to experimental results. The approach also demonstrates its robustness when applied to various picture datasets and imaging modalities [97].

In the next suggested method, a thresholding technique to remove the skull from each input brain image was applied. The brain image is broken into eight blocks when the skull is peeled away. The mean intensities were then computed for each block, and the five blocks with the highest mean intensities were chosen from the eight blocks. Following that, for each skull stripped input brain image, the five maximum mean intensities were used as a seed point for the region growth method, yielding five different areas of interest (ROIs). Finally, in terms of DSS, the final ROI was compared to a variety of state-of-the-art deep learning methods and region-based segmentation techniques. Three separate experimental sets were used to validate the suggested method. The DSS score was 0.89 in the first experimental setup, which used 15 randomly selected brain pictures for testing. The proposed technique which is shown in Figure 1.8 received DSS values of 0.90 and 0.80 for 12 randomly selected and 800 brain pictures, respectively, in the second and third testing setups. For the three experimental setups, the average DSS value was 0.86 [98].
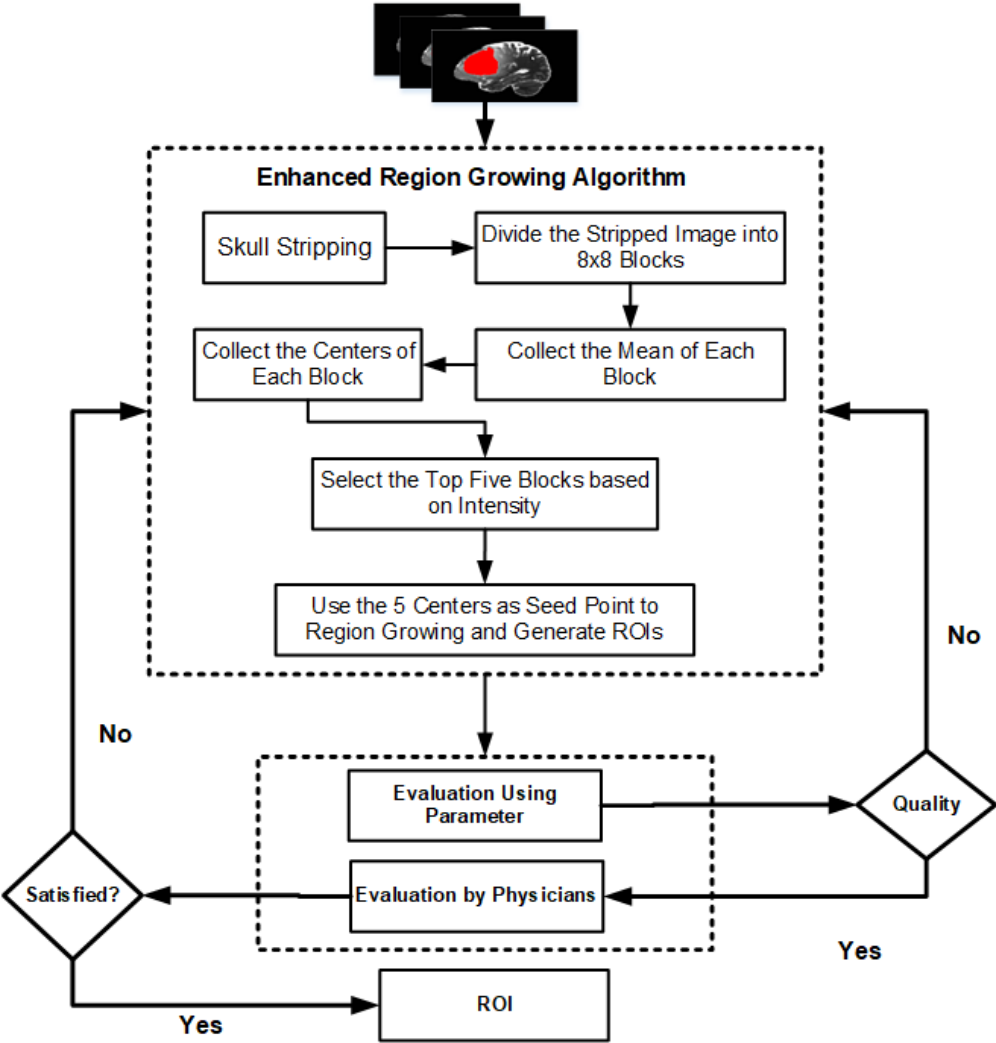
Figure 1.8. Region growing approach [98]

Preprocessing, segmentation, feature extraction, feature selection, and classification are the five stages of the next suggested work (Figure1.9). In the first phase, manual skull stripping is used to recover the region of interest (ROI), and the median filter is used to reduce noise effects. In the second stage, the tumor is segmented using an improved modified region growth algorithm (MRG) that includes both orientation and intensity constraints. In the third step, GLCM-based texture characteristics are extracted. After that, the grasshopper optimization algorithm selects the best attributes (GOA). Finally, the adaptive support vector machine (ASVM) is used to categorize tumor kinds. The outcomes of the experiments are examined using a variety of measures. The suggested method accurately segments and classifies the brain tumor in MR images, according to the results and experiments. Accuracy ratios for three different methods were determined as 0.95, 0.87, and 0.79, respectively [99].
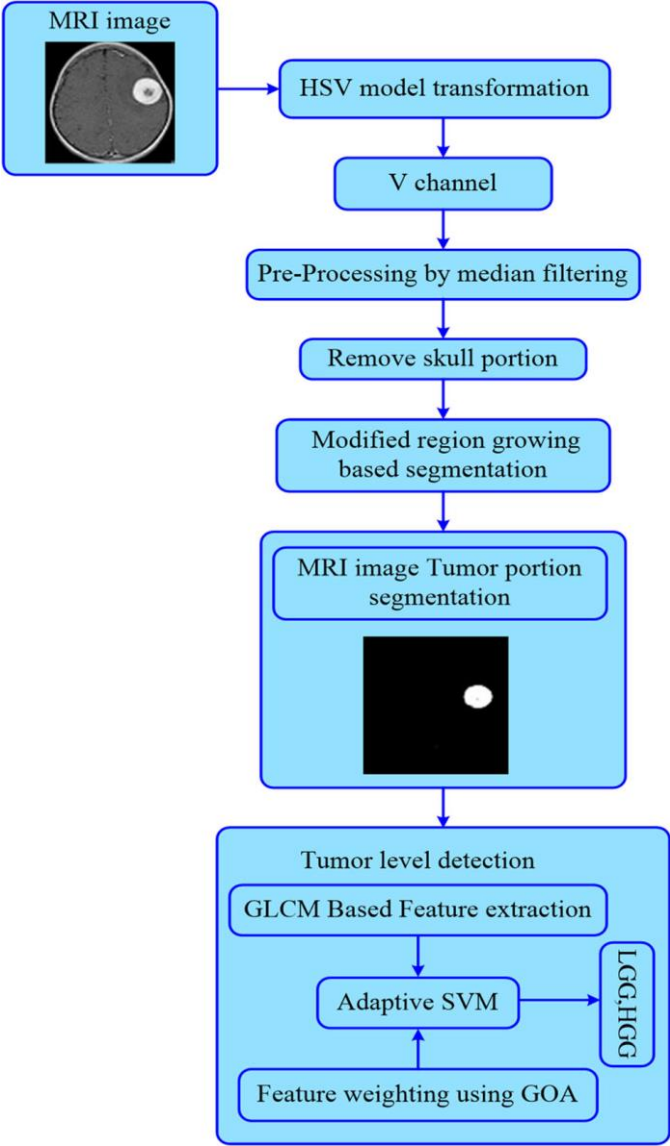
Figure 1.9. A method for modified region growing and adaptive SVM [99]

In the last research, a new framework for brain tumor segmentation is proposed. The proposed framework is depicted in Figure 1.10 as a seven-step block diagram. An anisotropic filter is used to pre-process the MRI volume of FLAIR pictures in the first stage. The data matrix (V) is formed in the second phase, and the data matrix is decomposed into the basis matrix (W) and coefficient matrix (H) in the third phase. The coefficient matrix(H) is clustered by fuzzy C-means clustering in the fourth phase, which segments the entire tumor in the FLAIR slice. Results of this proposed study indicate a dice sore as 0.80 [100].
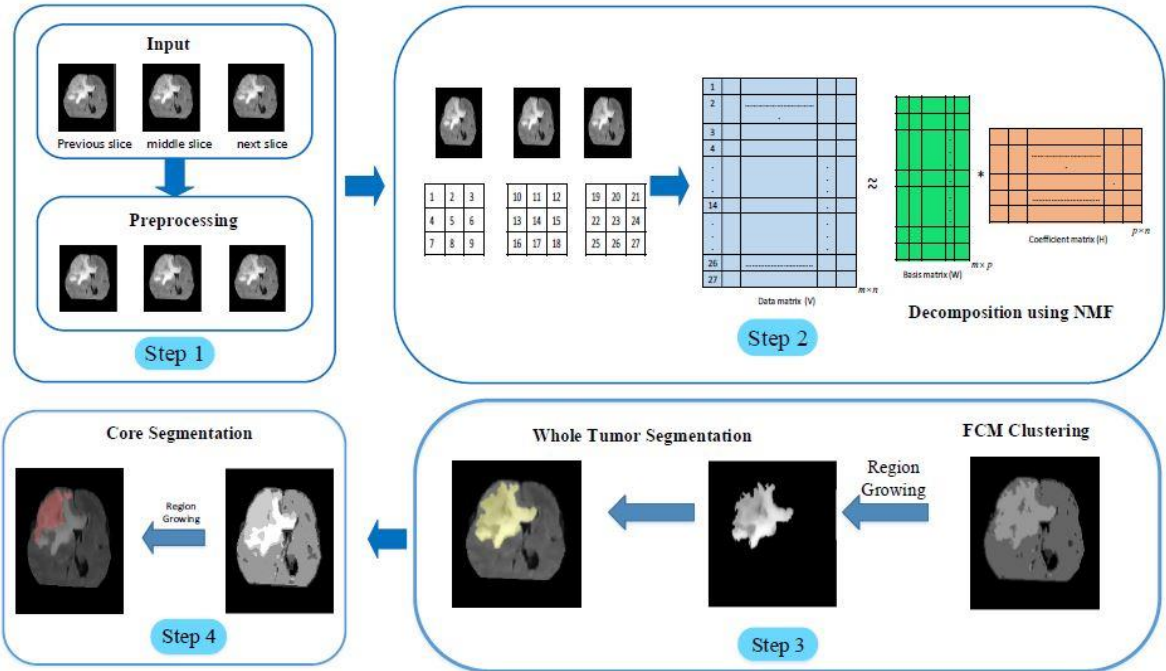
Figure 1.10. Approach for brain tumor segmentation by non-negative matrix factorization [100]

2.FUNDAMENTAL INFORMATION

The brain controls many things, including intelligence, creativity, emotion, and memory. The cerebrum, cerebellum, and brainstem are the parts of the brain that are protected within the skull. Our five senses - sight, smell, touch, taste, and hearing - all provide information to the brain at the same time. It assembles the messages in a fashion that makes sense to us, and it can store the data in our memory. The brain is in charge of our thoughts, memory, and speech, as well as the movement of our arms and legs and the function of many of our body's organs. The brain and spinal cord make up the central nervous system (CNS). Spinal nerves branching from the spinal cord and cranial nerves branching from the brain make up the peripheral nervous system (PNS) [101].

The cerebrum, cerebellum, and brainstem can be defined as the main parts of the brain. *The cerebrum*, which is made up of the right and left hemispheres, is the largest region of the brain. It is responsible for higher functions such as interpreting touch, vision, and hearing, as well as speaking, reasoning, emotions, learning, and fine motor control. *The cerebellum* is found under the cerebrum. Its objective is to keep muscle motions coordinated, maintain posture, and maintain balance. The cerebrum and cerebellum are connected to the spinal cord by the *brainstem*, which serves as a relay center. Breathing, heart rate, body temperature, wake and sleep cycles, digestion, sneezing, coughing, vomiting, and swallowing are all autonomic functions [102].

The right and left hemispheres of the cerebrum are separated into two parts. The corpus callosum, a bundle of fibers that connects them, transfers messages from one side to the other. The opposite side of the body is controlled by each hemisphere. Your left arm or leg may be weak or paralyzed if you have a stroke on the right side of your brain. Speech, understanding, mathematics, and writing are all controlled by the left hemisphere. Creativity, spatial ability, artistic, and musical abilities are all controlled by the right hemisphere. In around 92 percent of adults, the left hemisphere is dominant in hand use and speaking [103].

A brain MRI is one of the most regularly used medical imaging procedures. Using multiple MRI sequences, physicians can focus on different areas of the brain and investigate brain anatomy and pathology. MRI is used to examine the structure of the brain and to detect pathological situations such as cerebrovascular events, demyelinating illnesses, and neurological illnesses. Furthermore, an MRI can be utilized to examine brain activity during

certain activities (functional MRI - fMRI). The MRI of the brain should be done methodically, commencing at the midline and moving laterally. Thus, the ventricles should be examined first, followed by the surrounding subcortical tissues, brain lobes, cerebral cortex, meninges, and skull [104].

2.1. Brain Tumor

A brain tumor is one of the deadliest disorders which compresses brain tissues to create a place for enhancing mass. A tumor can eventuate in any body part preventing the regular working of the physiologic system and it is quite mortal when spread into the brain. Several kinds of brain tumors can occur in the human brain varying in positions, sizes, and shapes which should be treated accordingly. The abnormal tumors are classified as primary and secondary brain tumors based on their features. When cancerous tissues initiate and stay at the same position and place, they can be defined as primary brain tumors. The secondary brain tumor which is also known as a metastatic tumor is inclined to spread to other body sections from where it is revealed. When it comes to the classification of the primary tumor, it can be either benign (noncancerous) or malignant (cancerous). Furthermore, the treatment planning of brain tumors has significant importance and it can be carried out according to grade and tissue cell information which is usually obtained during a biopsy. Type of tissue cell can describe the cells that had caused to the tumor and the grade of tumor can estimate aggressiveness. During the various stage of tumor growth, different grades can be occurred [38].

2.1.1. Benign brain tumors

Chordomas are slow-growing tumors that are most common in people ages between 50 and 60. They can be mostly seen in the base of the skull and the lower section of the spine. Even though they are benign tumors, they might be capable of invading adjacent bone and effect neural tissue closed by. Rarely seen these tumors are only 0.2 percent of all primary brain tumors [39], [40].

Craniopharyngiomas are also benign, however, due to their critical location deep in the brain, they are difficult to intervene [39].

Other types of rare brain tumors such as gangliocytomas, gangliomas, and anaplastic gangliogliomas contain neuroplastic nerve cells which mostly occur in young adults are slightly well-differentiated [40].

Glomus jugulare are most commonly benign and their location is mostly under the skull base and very close to the jugular vein. These kinds of tumors are just responsible for only 0.6 percent of neoplasms of the head and neck [40].

Meningiomas are the most prevalent benign tumors consisting of the ratio between 10 to 15 percent of all brain neoplasms. These tumors are derived from the structures that resemble membranes around the brain and spinal cord [40,41].

Pineocytomas are usually benign lesions that occur mainly in adults. They have various characteristics such as noninvasive, homogenous, and slow-growing [41].

Apart from gliomas, meningiomas, and schwannomas, the most common intracranial tumor type is called pituitary adenomas. Most of these types of tumors are benign and inclined to be slow-growing. Including malignant kinds of these tumors occasionally spread through other parts of the human body. They can be diagnosed both in children and people in the age of 30s to 40s [40].

Schwannomas take place along nerves and consist of cells that cause electrical isolation for the nerve cells. Even though they are benign they can give rise to serious problems and even death in case of enhancing and applying pressure on nerves and the brain [40].

2.1.2.Malignant brain tumors

Gliomas, which account for 78 percent of malignant brain tumors, are the most common type of adult brain tumor. They originate from the brain's supporting cells, called glia. These cells are subdivided into astrocytes, oligodendroglial and ependymal cells (or oligos). The following are glial tumors:

- The most common glioma is an astrocytoma, responsible for around half of all tumors of the primary brain and spinal cord. Astrocytomas, part of the brain's supporting tissue, grow from star-shaped glial cells called astrocytes. They can occur in many parts of the brain, but in the cerebrum most commonly. Astrocytomas can grow in people of all ages, but in adults, especially middle-aged men, they are more prevalent. In infants or younger adults, astrocytomas in the base of the brain are more common and account for most brain tumors in children. Most of these tumors are considered low-grade in infants, while most are high-grade in adults [39].

- Ependymomas originate from the neoplastic transformation of the ventricular system lining the ependymal cells, accounting for two to three percent of all brain tumors [40].

- The most invasive type of glial tumor is glioblastoma multiforme (GBM). Such tumors tend to develop rapidly, spread to other tissues, and have a poor diagnosis. Several different cell types, such as astrocytes and oligodendrocytes, can be composed of them. GBM is more prevalent in individuals aged 50 to 70 and is more prevalent in men than in women [39].

- In general, medulloblastomas occur in the cerebellum, most commonly in adolescents. They are high-grade tumors, but they are typically receptive to chemotherapy and radiation [40].

- Oligodendrogliomas are derived from myelin-making cells, which are the insulation for the brain's wiring [39].

In this section, we explained the brain tumor types including benign and malignant tumors. There are many kinds of brain tumors considering both of these main tumors. One example can be seen in Figure 2.1.
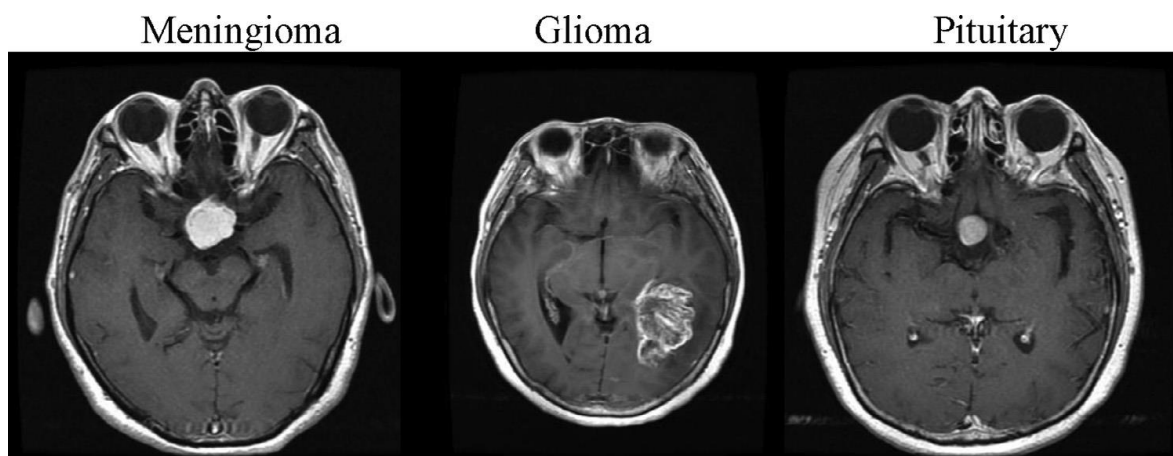
Figure 2.1. Brain MR images of different tumor types

In terms of diagnosing brain tumors, there are some effective methods including MRI and CT. The differences between these two imaging techniques provide efficient diagnosis and treatment planning. While MRI has certain advantages regarding its high contrast resolution of soft tissues, CT has also some positive aspects such as being faster, cheaper, and more available. Protocols for MRI brain tumors can differ slightly, but most contain the following traditional sequences as mentioned briefly in the first chapter: T1, T1C, T2, and FLAIR [42]. T2 and FLAIR are fluid-weighted sequences that help to recognize cytotoxic and vasogenic edema, necrosis, and tumoral cystic changes. The integrity of the blood-brain barrier is assessed by T1

pre- and post-contrast imaging. Cumulatively, a lesion's traditional MRI characteristics not only aid in diagnosis but also in determining tumor histological grade. New treatment regimes will be planned as the complexities of tumor genesis are identified. These new therapies, sadly, can lead to unpredictable and sometimes confusing image appearances on traditional MRI sequences. The phenomena coined by pseudo progression and pseudo answer have arisen, specifically with GBM therapies [43].

Procedures such as magnetic resonance (MR) imaging, positron emission tomography (PET), and computed tomography (CT) scanning are used for diagnosis. In detecting various types of diseases, these imaging processes are beneficial. The use of harmless magnetic fields and radio waves makes it very popular to successfully diagnose and treat brain tumors with MR images.

2.2. Medical Imaging

Medical imaging refers to the methods and procedures used, including the study of natural anatomy and function, to produce photographs of the human body (or parts of it) for different clinical purposes, such as medical procedures and diagnosis or medical research [44].

Although mathematical sciences were commonly used for image processing, before the development of computed tomography (CT) for the imaging of X-rays and isotope emission tomography, they were of little significance in bio-medical practice, then MRI ruled as the most informative medical imaging technique over the other modalities in many ways [45]. The general representation of a medical imaging system is shown in Figure 2.2.
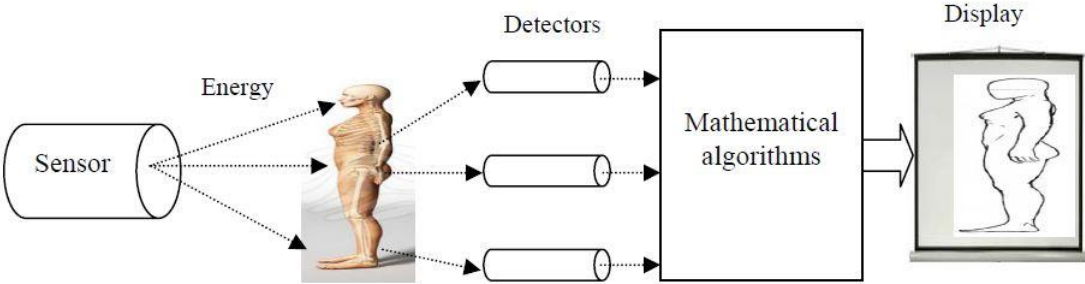
Figure 2.2. General representation of a medical imaging system [45]

In Figure 7, a medical imaging system is described which consists of a sensor as an energy source that is able to penetrate and pass through the human body. The energy is absorbed or attenuated at various levels based on the atomic number or density of different tissues. At the

end of this process, signals are created. To detect these signals, special detectors that are compatible with the energy source are designed and these signals are used to create an image by utilizing mathematical manipulation techniques. The final stage involves classification for an obtained image according to the energy form applied to the human body. Several different methods can be used to get a look into the patient, depending on the energy sources. Such strategies are based on a signal that passes right through a patient. These signals interact with the patient's tissues. A picture of the inside of the patient can be created by recognizing the signal coming from the body [46].

2.2.1 Digital image processing

An image can be defined as a two-dimensional function f (x, y). Here, the x and y spatial coordinates and the amplitude in any pair of (x, y) coordinates of f are called the brightness or the gray scale of the image at that point. When the brightness values of x, y, and f are measurable, the resulting image is called a digital image. The digital image processing field refers to the processing of digital images by means of a digital computer. A digital image is a combination of a measurable number of elements. Each of these elements has a specific location and value. These elements are called picture elements, image elements, image elements, and pixels. Digital images require a lot of archive and computing power in the field of digital image processing. This depends on the development of digital computers and the development of supporting technologies for data storage, imaging, and transmission. [8].

In today's technology, almost all medical imaging techniques are capable of providing digital image processing for diagnosing and surgical planning. There are several basic steps regarding digital image processing that are shown in Figure 2.3.
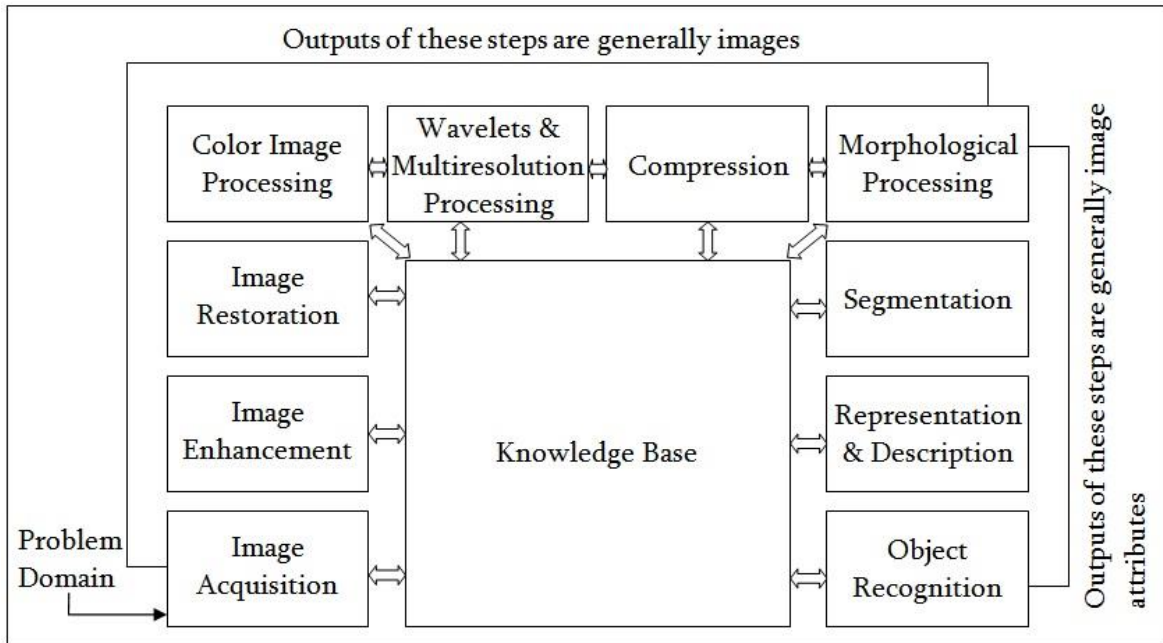
Figure 2.3. Fundamental steps in digital image processing [8]

As can be seen in Figure 8, digital image processing starts with the *image acquisition* stage which generally contains preprocessing operations such as scaling. As a second section, *image enhancement* can be carried out to manipulate an image to obtain more suitable results comparing to the original image for a specific application. *Image restoration* is another basic step that is responsible for developing the appearance of an image. Due to the significant use of digital images over the Internet, *color image processing* became quite common. In addition, *wavelets* can be used to represent images in various degrees of resolution such as image data compression. Furthermore, by applying the *compression* process, it is possible to reduce the storage demanded saving an image or transmit it based on necessary bandwidth. *Morphological processing* is quite a beneficial method that is capable of extracting image components to identify and represent the shape. *Segmentation* is the process of separating a digital image into its parts of objects. It can generally be said that the more detailed the segmentation is, the more likely it is that identification will succeed. Raw pixel data which is acquired as an output of the segmentation stage is used at the stage of *representation and description.* The raw pixel data mostly comprise the boundary of the region or all the points in that region. *Description,* which is also known as feature selection, deals with the extraction of attributes that result in or are necessary for distinguishing one class of objects from another with some quantitative details of interest. *Recognition* is used for assigning a label (e.g., "tumor") to an object regarding its definer [47,48].

Segmentation is a very effective pre-processing method in software-based medical image analysis and diagnosis. MR brain images have a wide range of applications in the investigation of complex anatomical structures and human behavior. Due to the inhomogeneity caused by the radio-frequency coil, MR brain images are severely affected by noise and artifacts. Therefore, the blurry nature of the tissue boundaries in the image makes the segmentation process more difficult [48]. In addition to the general steps of digital image processing, common components of an image processing system should also be under consideration. These components are shown in Figure 2.4 and their function is also explained in the following paragraph.
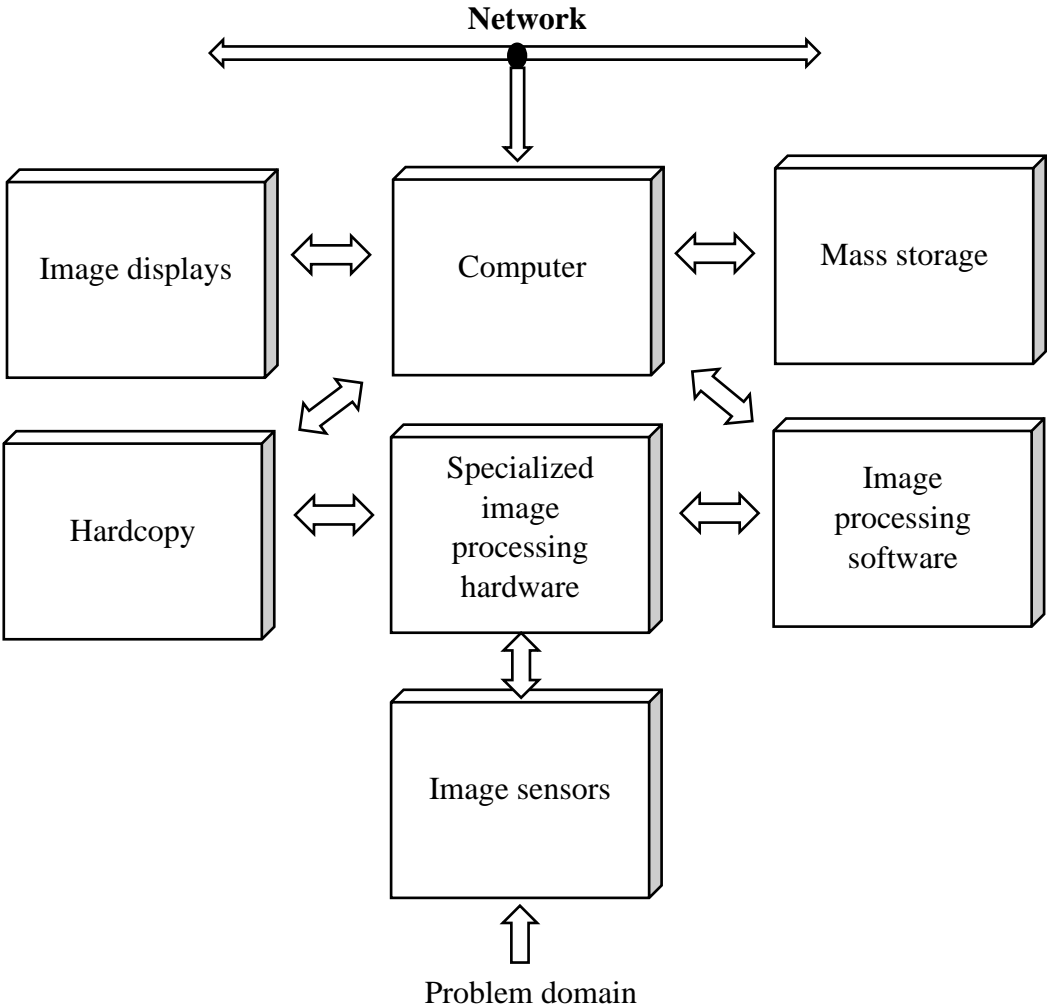
Figure 2.4. Component of an image processing system [8]

In terms of *sensing*, the successful acquisition of digital images involves two components. One of them is a physical device that is sensitive to the energy form scattered by the object that wanted to be imaged. The other one, also known as a *digitizer*, is a device for transforming the

output of the sensing device into digital data. *Specialized image processing hardware* mostly contains the digitizer and hardware that are responsible for performing other primitive transactions for instance arithmetic logic unit (ALU). The ALU is able to execute arithmetic and logical operations that are parallel to entire images. After images are converted into digital form, the ALU can be used to average images for the operation of noise reduction. This unit basically distinguishes from typical main computers in operations that require fast data. The *computer,* which is one of the main parts of the image processing system is used for general purposes and can vary between a PC and a supercomputer. *Software* component in image processing carries out specific tasks and contains specialized modules. One of the mandatory components in image processing applications is *mass storage* capability. In the case of dealing with many numbers of images, it can be challenging and critical to providing the required storage in an image processing system. Digital storage can be classified into three categories including short-term storage while performing processing, online storage to execute comparatively fast recall, and archival storage. *Image displays* are mainly used for TV monitors favorably on the flat screen. *Hardware* devices are utilized for recording images including film cameras, laser printers, and digital units like optical and CD-ROM disks. *Networking* is nearly a default function in today's computer systems. Due to the big amount of data used for the applications of image processing, one of the most significant aspects of image transmission is bandwidth [48].

Considering the components and fundamental steps in digital image processing, combining new developing technologies with this basic knowledge can even be more effective in terms of applying different image processing techniques to medical images. Therefore, more accurately diagnosing and more useful surgical planning can be executed for patients. One of these developing technologies which became quite common in the last few years is deep learning. Using deep learning networks (e.g., 'convolutional neural networks (CNN)') can create a huge impact on increasing the accuracy of diagnosis such as brain tumors. In order to detect brain tumors, segmentation can be used which is one of the most prevalent applications in the field of medical imaging. The segmentation method can even be more efficient when it is used in deep learning applications.

2.3.Deep Learning

In software-based medical image analysis for more accurate diagnosis, segmentation of MRI brain image data has excellent benefits. Due to the limits of image acquisition technologies, MRI images can be greatly influenced by noise and artifacts, making segmentation more

challenging[49]. Although MRI is a useful tool for properly defining brain structure, various factors, such as poor spatial resolution, low contrast, inhomogeneity, and object shape instability, might make medical image segmentation a challenge. In computer-aided medical image analysis and diagnosis, segmentation is a reliable and effective preprocessing method. Because of their complex anatomical structures and importance in human behavior study, MRI brain images have a wide range of applications. Due to the fuzzy appearance of the tissue borders on the image, the homogeneity created by the radio frequency coil makes the segmentation more challenging [50,51]. Manual segmentation of the 3D MR image is applied by medical professionals and is based on more knowledge and experience. Automatic segmentation methods can be applied to MR images to prevent these issues. As a result, more dependable and measurable outcomes can be obtained. Low contrast between soft tissues, increased noise, and various sorts of artifacts, on the other hand, might lead to poor diagnostic accuracy[52]. Because learning-based systems do not require registration, they may be the most successful method. These methods make use of features extracted from the training image[53].

Some problems need to be solved in order to successfully implement 3D medical imaging, deep learning techniques, and segmentation. Some of these include the ground truth version of the images, resource memory limitation, and unstable dataset problem [54]. A CNN structure has the ability to learn complex features from a brain MRI image. For the inputs of the CNN, fragments are extracted from the MR images and the input of the network is fed with these fragments. Then, trainable convolution filters and local subsampling are used to extract these complex features [54].

Computers can find complicated patterns in vast data sets using deep learning techniques. The main objective of deep learning-based mathematical models is to disseminate learned expertise and make accurate predictions for fresh and unknown data. An artificial neural network is made up of layers of connected computer units called neurons. These layers are the input layer, where data enters the network, the hidden layers, which alter the data, and the output layer, which generates the neural network's predictions. Figure 2.5 shows 1-dimensional node visualizations of these structures utilized in medical imaging. Folded neural networks are frequently used to implement deep learning in medical imaging. This is because CNN is a powerful method for learning suitable images and other structured data representations. Figure 2.5d shows the node graph used in medical pictures for CNNs once more. Blue dots represent input layers, orange points represent hidden layers, and green points represent output layers in Figure 2.5. CNN, a specific type of artificial neural network, aims to preserve spatial relationships in data with very

little connectivity between layers. The CNN's input is arranged in a grid structure and then sent to the layers that maintain these relationships. Each layer process runs on a small region of the previous layer. There are many layers in a CNN. These can be expressed as convolution and activation layers, pooling layers [55].

In addition to the convolutional neural networks, Auto-encoder models are simple network structures that utilize only one hidden layer to reconstruct data at the input layer at the output layer (Figure 2.5a). The restricted Boltzmann model (RBMs) seen in Figure 2.5b is another deep learning technique. Again, another deep learning technique used for image processing is the recurrent neural networks (RNNs) shown in Figure 2.5c. This method has traditionally been developed for discrete sequence analysis. Figure 2.5e shows the model representing multi-stream layered neural networks. According to this model, the defined CNN structure can be organized as multiple data sources. Also, in this model, channels can be combined at any point in the network. This method has two main application areas related to image processing: multi-scale image analysis and 2.5D classification [56].

Among these deep learning techniques, it is the most widely used CNN method due to its unusual structure. The content includes the input layer, the feature extraction layer that works together with the convolution layers, the linear unit (ReLU) layer that is oriented to activate the function, the pool, and the classification layers [57].
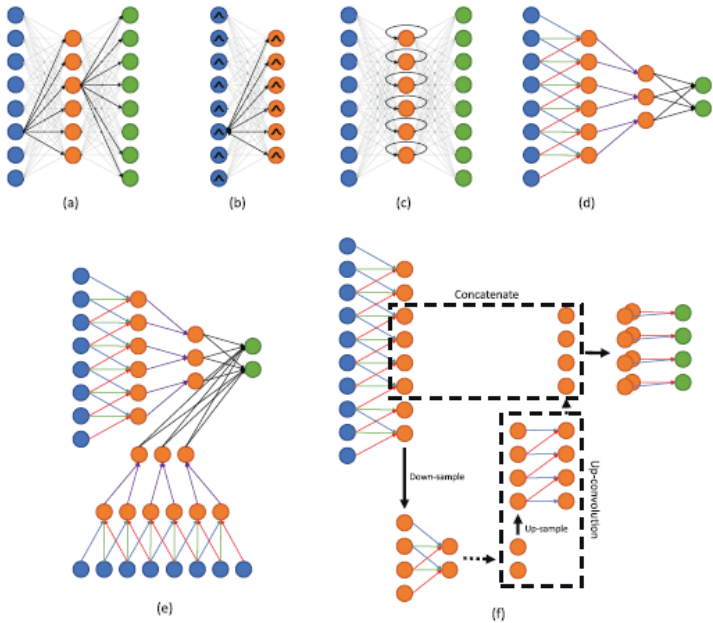
Figure 2.5. Node representation of artificial neural networks used in medical imaging, a) Auto-encoder, b) Constrained Boltzman model, c) Repetitive neural networks, d) Convolutional neural networks, e) Multi-stream convolutional neural networks, f) U-net [56]

Tasks of these layers: It is a 3-dimensional layer with a convolution layer and applies floating cubic convolution filters to the 3-dimensional inputs. This layer applies the convolution process to the data in the input layer by moving the filters vertically, horizontally, and along the depth of the input. So it performs the down-sampling process. The alternating convolution layer, on the other hand, upsampling the feature map obtained after the convolution layer. ReLU layers apply thresholding to each element of the input and set all values less than 0 to zero. The maximum pool layer performs down-sampling by dividing the input into rectangular pools and subtracts the maximum calculation for each zone [58].

Recently, CNN has become very common for analyzing medical images. To perform segmentation with the CNN, a fragment/patch of the target voxel or pixel is marked and fed as input to the artificial neural network. The center voxel can be used for the output of the network. Thanks to the convolution layers, CNN maintains a significant amount of nonlinear matches between input and output [58].

CNN, deep residual Network (DRN), deep feed-forward network, deep folding neural network (DCNN), and U-Net are only a few examples of deep learning network architecture. CNN is the most widely used deep learning methodology in image processing because of its unique structure, which contains an input layer, feature extraction layers that interact with convolution layers, and a rectified linear unit (ReLU) layer to enable it, as well as an activating function, pool layers, and classification layers [59]. CNN has recently gained popularity as a tool for assessing medical images. The target voxel or pixel is designated with a patch and then fed into and out of the networks to accomplish segmentation, allowing the center voxel to be used. CNNs capture strong nonlinear matching between inputs and outputs due to the convolution layers[60]. CNN is capable of extracting complicated properties from brain pictures. MRI brain images are patched and fed into the network as input for CNN. These complicated features are then extracted using trainable convolution filters and local subsampling[60].

As mentioned before, deep learning expresses a neural network that has multiple layers of a nonlinear processing unit. These consecutive layers utilize the output of the previous layer as input. By using these layers, the network can extract complicated hierarchy features from a large amount of data. In the last years, deep learning became quite common and shows important developments in the field of object detection, recognition, image classification, and medical image analysis. Moreover, they have generated significant outcomes comparable or superior to the expert in their fields. CNN, which has the most effective deep learning algorithms especially in image segmentation, was firstly introduced in 1989 and the first

successful application was hand-written digit recognition in 1998 [13]. Other CNN-based architectures were proposed in subsequent years, including VGGNet [61], GoogleNet [62], Residual Net [63].

CNN is a neural network of multiple layers that includes convolution, pooling, activation, and fully connected layers. CNNs are built around convolution layers, which are used to extract features. The convolution technique generates distinct feature maps depending on the filters employed. The pooling layer performs a downsampling technique by using the maximum or average of the specified neighborhood as the value to minimize the spatial size of each feature map. The non-linear rectified layer (ReLU) and its variations, such as Leaky ReLU [64], are extensively used activation functions that convert data by clipping all negative input values to zero while sending positive input values as output. A fully connected layer contains neurons that are fully connected to all preceding layer activations. They are used to flatten the results before linear classifiers are used to produce a prediction and are placed before the output of a CNN classification. While training the CNN architecture, the model predicts class scores for training images, calculates the loss using the selected loss function, and finally updates the weights through back-propagation using the gradient descent method. Cross-entropy loss is one of the most commonly used loss functions, and the most popular method of operating gradient descent is stochastic gradient descent (SGD) [64].

The essential prevalent characteristic of deep learning systems is their capability to learn features that provide learning representations of data automatically. This is the primary distinction between approaches to deep learning and more "classical" machine learning [63]. The interest in deep learning is mainly triggered in medical imaging by convolutional neural networks (CNNs), a powerful way to learn useful image representations and other structured data.

A CNN is a special kind of artificial neural network, with very few interactions between the layers, aimed at preserving spatial relationships in the data. The input of a CNN is adjusted as a grid structure and fed into the layer that is capable of preserving these relationships by performing on a small region of the previous layer in each layer (Figure 2.6). For image-related tasks, CNNs can create a significantly influential representation of the input data. As described earlier, a CNN has convolution and activation layers that are interspersed with pooling layers. This type of deep learning network is mostly trained with backpropagation and gradient descent.
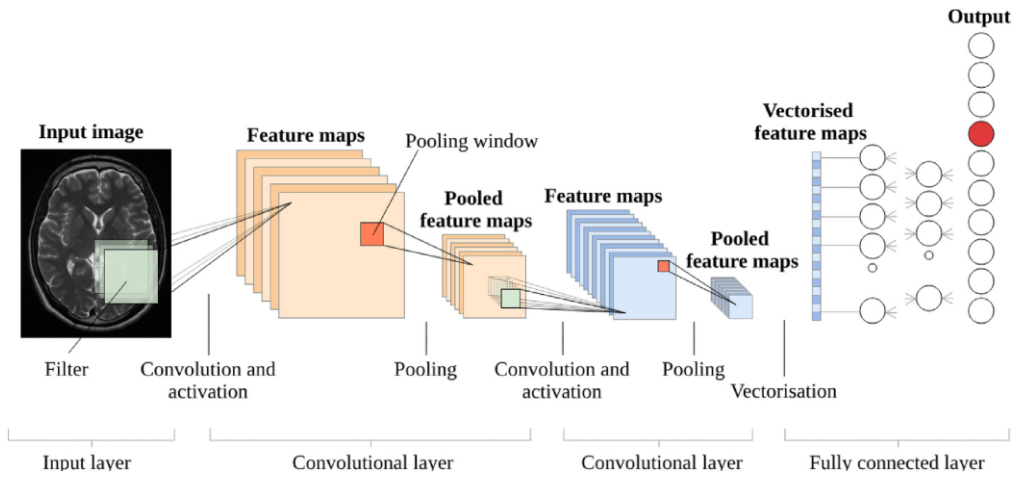
Figure 2.6. Representation of a typical CNN architecture

2.3.1.Convolutional layers

Convolution layers are responsible for the activations from the previous layers by using convolution operation with a group of small filters. They are collected in a tensor $X^{(b, a)}$, where b represents the filter number and a corresponds to the layer number. By using each filter with the exact same weights along with the whole input domain, one of them can perform a significant reduction in the number of weights that are required to be learned. The explanation for this weight-sharing is that characteristics that occur in one part of the picture are likely to appear in other sections as well. Executing all the convolutional filters at all places of the input to a convolutional layer generates a tensor of feature maps [59].

A convolutional layer consists of neurons that link the input images or the outputs of the previous layer to subregions [65]. While scanning through an image, the layer learns the features localized by these regions. A 3-by-3 filter scanning through the input is shown in Figure 2.7 which represents the basic convolution operation. The lower map represents the input and the output is represented by the upper map.
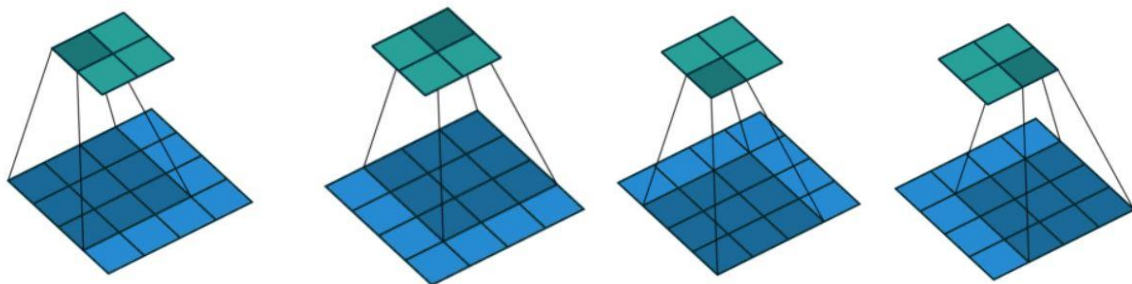
Figure 2.7. Standard 2-dimensional convolution application [65]

Even though 2D convolution filters can be useful in many cases, in terms of processing 3D images by using deep learning networks, 3D convolution operation must be applied. When it comes to 3D convolution, the generalization of 2D convolution represents them. In this case, the input layer depth is greater than the filter depth. Therefore, the 3D filter can create a motion in all directions including height, width, and channel of the image. The element-wise multiplication and addition provide one number at each location. Because of the filter's movement in a 3D space, the output number is also adjusted in 3D space. Representation of the 3D convolution operation is shown in Figure 2.8.
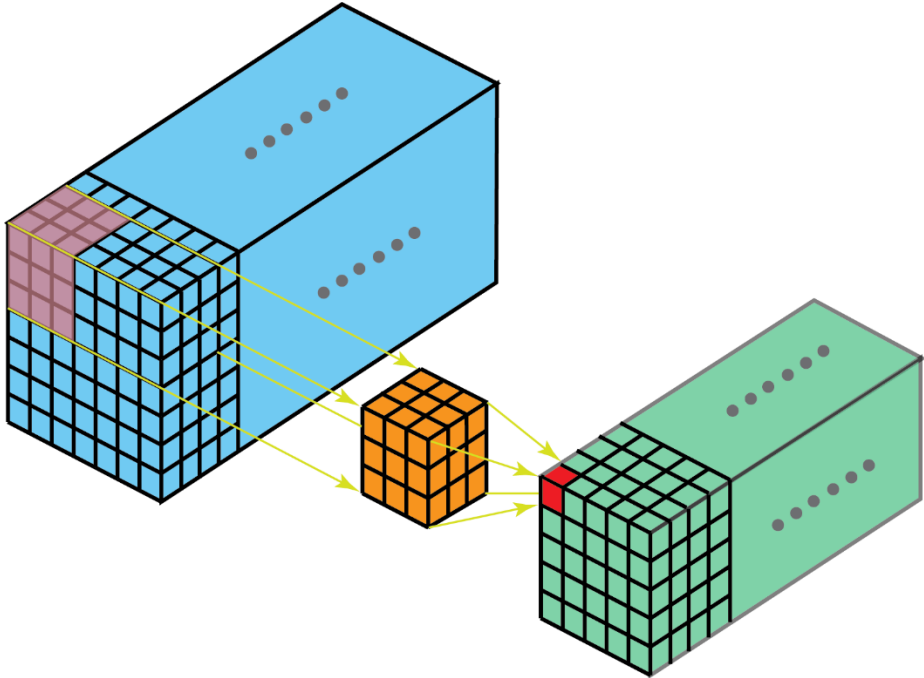
Figure 2.8. Simplified demonstrations of 3D convolution [66]

3D convolutions may define the spatial relationships of objects in 3D space, similar to 2D convolutions that encode the spatial relationships of objects in a 2D domain. For some applications, such a 3D relationship is significant, such as in 3D segmentations/reconstructions of biomedical imaging, e.g., CT and MRI, where 3D space meanders around artifacts such as blood vessels. [66]

2.3.2.Activation layers

The feature maps that are extracted from a convolutional layer are fed into nonlinear activation layers. That's way, the whole neural network can approximate nearly any nonlinear function [65]. The activation functions are usually known as the simple rectified linear units or ReLUs. If it is positive, ReLU will generate the input directly, otherwise zero will be output. For several forms of neural networks, it has become the default activation feature because it is easier to train a model that uses it and often achieves better performance.

2.3.3. Pooling layers

After the input data was fed through one or more convolutional layers, feature maps from these layers were acquired and they are basically collected in a pooling layer. Pooling operations require small grid sections as input and generate a single number for each section. The number is mostly calculated by using the max function which is also known as max-pooling or the average function which can be defined as average pooling. Since a small change in the input image results in small changes in the activation maps, some translational invariance is given to the CNN by the pooling layers. An example of max-pooling and average pooling is given in Figure 2.9.
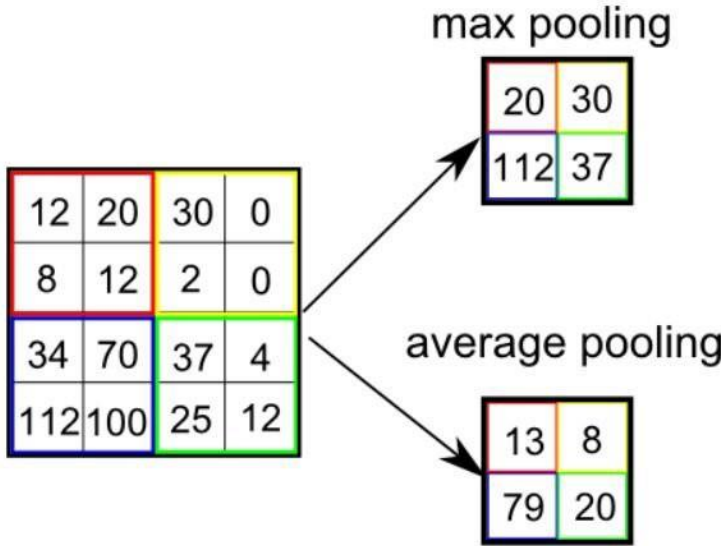
Figure 2.9. Representation of operations in pooling layers [67]

Using convolutions with increased stride lengths is another way to achieve the downsampling effect of pooling. Another representation of a max-pooling operation with a stride value '2' is shown in Figure 2.10.
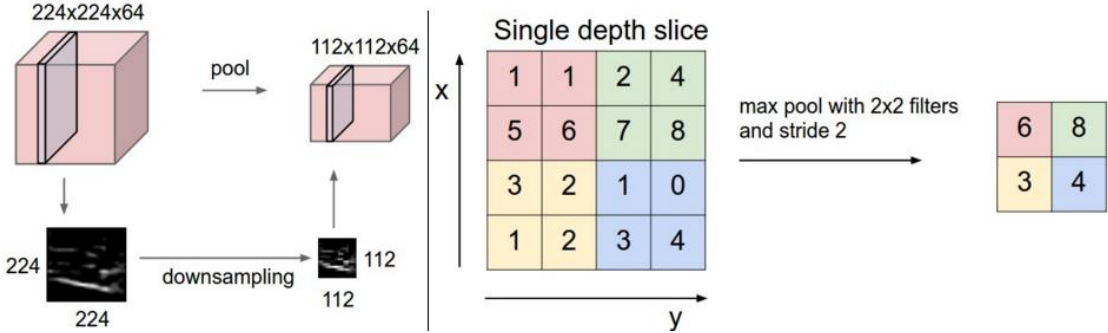
Figure 2.10. Max-pooling in a neural network [68]

2.3.4 Batch normalization layers

These layers are mainly inserted into the network after activation layers and they generate normalized activation maps by subtracting the average and dividing by the standard deviation for training batches. The network is forced to adjust regularly, like batch normalization layers, as the training batch enters these layers, which acts as a regularizer for the network, its activations to zero mean and unit standard deviation speed up training, and makes it less dependent on careful initialization of parameters [69].

2.3.5. Transposed convolution layers

These layers can perform operations by applying transposed convolution in the opposite direction of a normal convolution which is also known as up-sampling for many network applications. Some examples include the generation of high-resolution images and the mapping of low-dimensional characteristics to high-dimensional space, such as auto-encoder or semantic segmentation.

Traditionally, by applying interpolation schemes or manually constructing rules, one may achieve up-sampling. On the other hand, modern architectures such as neural networks appear to enable the network itself, without human interference, to automatically learn the proper transformation. Therefore, transposed convolution can be used to achieve this goal [70].

The implementation of a transposed convolution with a direct convolution is always possible. In Figure 16, transposed convolution is applied by using a 3x3 kernel over 2 x 2 input padded

with a 2 x 2 border of zeros using unit strides. As a result of the up-sampling operation, 4x4 output data is obtained.
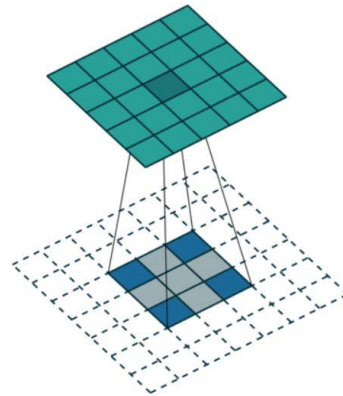
Figure 2.11. Up-sampling with transposed convolution [70]

2.3.6. Softmax layer

Softmax, just before the output layer, is implemented via a neural network layer. As the output layer, the Softmax layer must have the same number of nodes. Softmax regression is a type of logistic regression that normalizes an input value into a value vector that follows a distribution of probability with a total sum of up to 1 [71].

2.3.7. Pixel classification layer

This layer is capable of providing a categorical label for each image pixel or voxel. For especially semantic segmentation networks, it generates a pixel classification output layer. The layer outputs a categorical label for each CNN-processed picture pixel or voxel. During preparation, the layer automatically ignores unknown pixel labels [72].

2.4.Semantic Segmentation

Speaking of semantic segmentation, it is a technique that describes the process of associating each pixel of an image with a class label. For a semantic segmentation network to be trained, a collection of images and their corresponding labeled pixel images are required. Pixel labeled image is the image where the value of each pixel represents the categorical label for that pixel. The common layout in semantic segmentation networks requires downsampling the image between the convolution and relu layers, and then the output needs to be upsampled to match the input size. During this process, the network performs processing using non-linear filters.

In order to evaluate the results of semantic segmentation, several different metrics can be used including global accuracy, mean accuracy, mean IoU, weighted IoU, mean BF score, and dice-index. The development of a confusion matrix is another evaluation operation for pixel classification based on classes [73]. The instances in a predicted class are represented by every row of the confusion uncertainty matrix and each column represents the instances in a true class.

Table 2.2. Class confusion matrix for pixel classification

		True class	
		P	N
Predicted class	P	True Positive (TP)	False Positive (FP)
	N	False Positive (FN)	True Negative (TN)

The ratio of correctly categorized pixels to the total number of pixels without depending on a class defines global accuracy. For each class, the ratio of correctly classified pixels to total pixels is known as the mean precision shown in Eq (1) [74].

$$Accuracy = \frac{TP + TN}{TP + TN + FP + FN} \qquad (1)$$

The IoU (Intersection over Union) metric, also known as the Jaccard index and illustrated in Eqs. (2) and (3), can be used to more consistently measure semantic segmentation outcomes (3) [75]. This is one of the most commonly used metrics in the semantic segmentation process. It's defined as the ratio of segmented image overlap areas to ground truth images (Figure 2.12) [75]. As a result, this metric can be effective for evaluating the similarity of ground truth and predicted labels. The value of this measure ranged from 0 (no overlap) to 1 (full overlap).

$$Jaccard(A, B) = \frac{||A \cap B||}{||A \cup B||} \qquad (2) \qquad Jaccard = IoU = \frac{TP}{TP + FP + FN} \qquad (3)$$
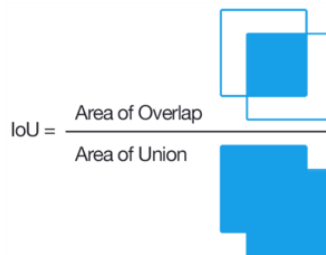
Figure 2.12. Calculation of IoU metric [75]

For the evaluation of the predicted mask collection, a comparison between predicted masks and each of the available target masks can be done. When a prediction-target mask pair has an IoU score that exceeds some predefined threshold, a true positive is observed. A false positive means that no corresponding ground truth object mask has an expected object mask. A false negative means that there was no corresponding forecast object mask for a ground truth object mask.
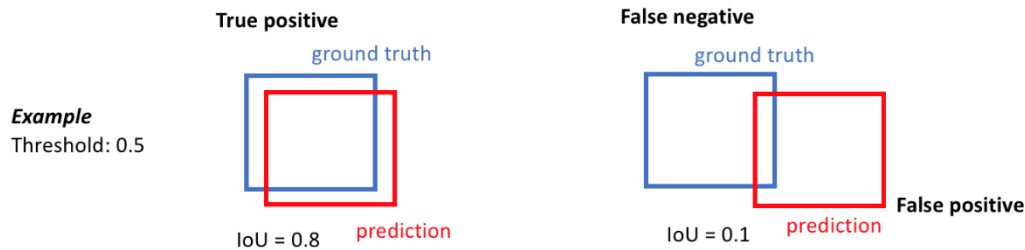
Figure 2.13. Representation of the IoU calculation [76]

The Weighted IoU is the mean IoU value of all classes and the weighted mean value of the number of pixels for each class is calculated. The BF score shows the similarity between each class's projected contours and the actual contours. In addition, the dice coefficient plays an important role in assessing semantic segmentation outcomes, which is like the IoU shown in Eqs. (4) and (5) [77].

$$Dice(A,B) = \frac{2||A \cap B||}{||A|| + ||B||} \qquad (4) \qquad Dice = \frac{2TP}{2TP + FP + FN} \qquad (5)$$

Here is an example of two circles representing the ground truth and the predicted masks for an arbitrary object class given by the Dice and IoU metrics [78].
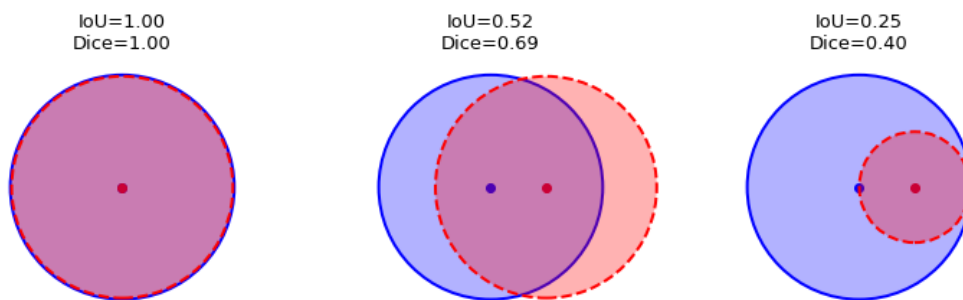
Figure 2.14. Illustration of dice and IoU metrics based on ground truth and predicted masks [78]

Important statistics about semantic segmentation and label prediction can be represented by all these metrics.

3.MATERIAL AND METHODS

The procedures performed in the current study, the grayscale imaging of brain MRI sections and the creation of an artificial neural network using deep learning techniques of all these sections in an MR image, and then the semantic segmentation technique to distinguish healthy brain tissue or tumor tissue from the background in the image. It is aimed to be Using 3D MR images and using the Deep Learning Toolbox feature of MATLAB, training the computer through artificial neural networks mentioned in literature research and performing tumor diagnosis in these 3D images, and increasing the diagnostic accuracy percentage.

Our proposed method begins with image acquisition in MATLAB, followed by pre-processing applications such as histogram equalization, as stated previously. Then, as an input, random patches from MR images are fed into a neural network. This network was trained using 16 layers, including convolution layers, batch normalization layers, relu layers, max-pooling layers, and transposed convolution layers and relu layers for down-sampling and transposed convolution layers and relu layers for up-sampling. The softmax layer and pixel classification layer complete the deep learning network. Test images were used to apply semantic segmentation after the training process.

Segmented MR slices and predicted labels are among the semantic segmentation's outcomes. The results of semantic segmentation and 3D imaging, including the whole brain, ground truth, and projected labels, and tumor position, are presented in the final stage. The Block diagram of the proposed method is shown in Figure 3.1.

Figure 3.1. Block diagram of the proposed method.

3.1. Image Dataset

In the study, NIfTI (Neuroimaging Informatics Technology Initiative) meta-data was used as image data. These data, called the BraTS data set, include MR scans of brain tumors. These data, which are known as glioma and are the most common basic brain tumor type, are taken

from http://medicaldecathlon.com/. The brain MR dataset contains 257 training images with corresponding labels, and the dimensions of these MR images are 155 sections and T1 (T1-weighted), T1C (contrast-enhanced T1-weighted), T2 (T2-weighted), and FLAIR (Liquid Attenuation Inversion Recovery) The dimensions of the 4 different imaging modalities are 240 * 240. 5 distinct MR images were used as test images for applying semantic segmentation for background and tumor prediction, as well as analyzing segmentation criteria such mean accuracy, mean IoU, weighted IOU, and mean BFScore [79]. The experiments were carried out on a computer with an i7 9th generation processor unit 2.60 GHz / 8GB RAM and NVIDIA GEFORCE GTX. In terms of brain tumor diagnosis, each MR imaging modality has various significance. Edema tumor locations can be identified using T2 images, healthy tissues can be discriminated using T1 pictures, tumor margins can be identified using T1C imaging, and edema regions may be distinguished from the cerebrospinal fluid using FLAIR images. [80,81]. In our presented approach, all imaging modalities are first processed in a pre-processing imaging application before being fed into a neural network as an input image. Image processing techniques such as image sharpening and histogram equalization were used to the original images after they were displayed on MATLAB to enhance contrast.
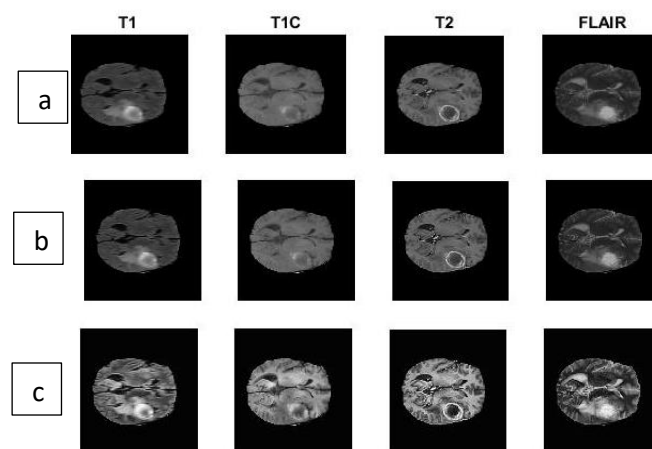
Figure 3.2. Different MR modalities and pre-processing operations a) original images, b) images after image sharpening were applied, c) images with histogram equalization.

3.2. Pre-processing

In order to increase contrast, histogram equalization was applied to the original images, as shown in Figure 3.3. We used an adaptive histogram equalization technique, which takes a different approach than standard histogram equalization in that it computes multiple histograms. Each of these histograms corresponds to a different section of the image, and they

are used to redistribute the image's lightness value. This approach strengthens the definitions of the edges in each area and increases the local contrast [82]. Following this segment, random patches for training are extracted from two image-based datastores that include network inputs and desired network responses.

In addition, by determining the section number and using preprocessing techniques such as sharpening and histogram equalization in all 155 sections, the contrast differences in the image have been clarified and then these images are intended to be used as test images after the artificial neural network is trained. It is also among the studies that these 4 different modalities are displayed in a single figure (Figure3.3).
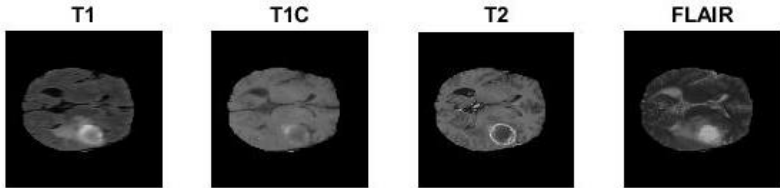
Figure 3.3. Displaying original MR images in four modalities

These 4 different modalities of this selected section were then corrected by the sharpening pre-processing technique (Figure 3.4).
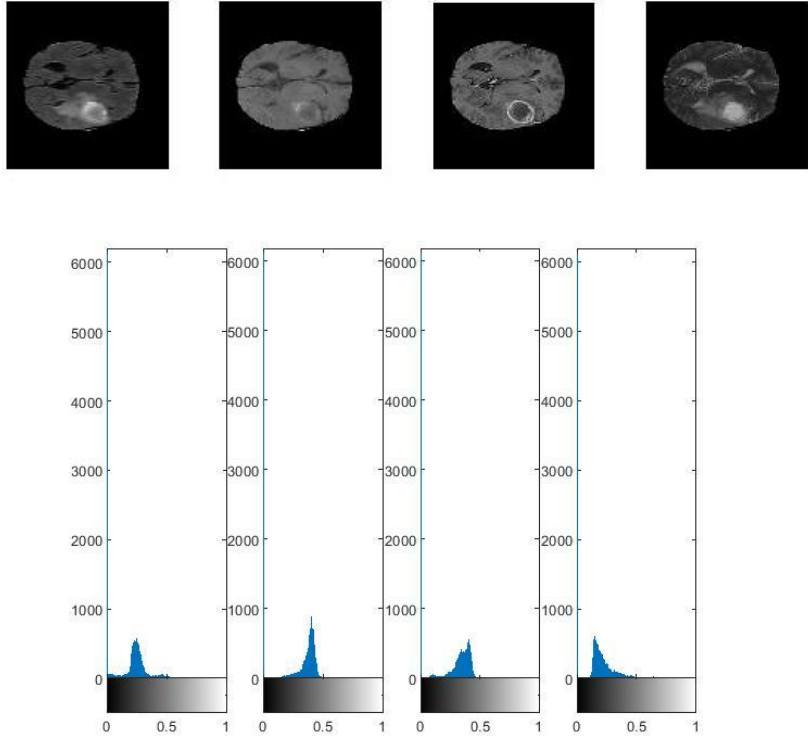
Figure 3.4. Sharpening of the MR images and related histograms

By applying the histogram equalization technique to these sharpened images, the contrast differences have been made clear and the resolution has been increased (Figure 35). All slices can also be shown in Figure 3.6.
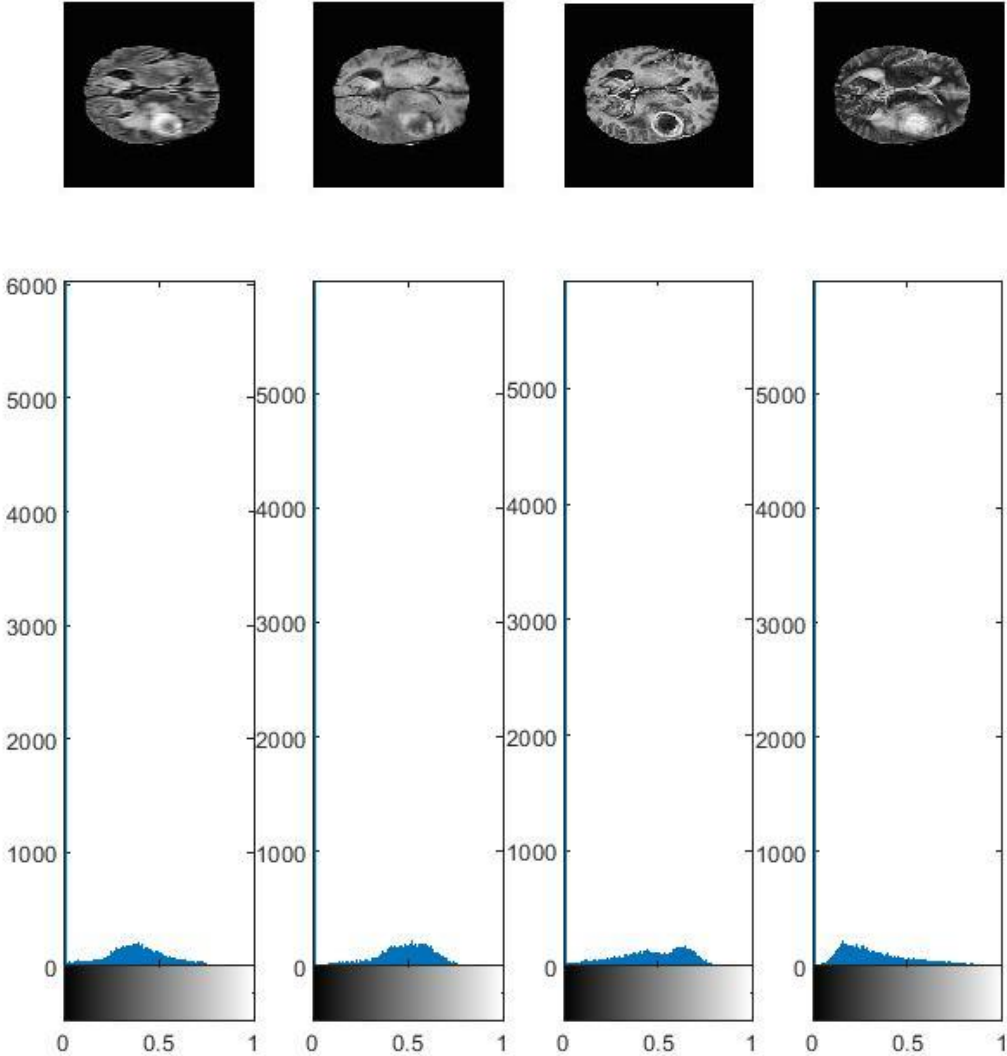
Figure 3.5. Applying histogram equalization technique to MR images

Random patches for training are collected from two image-based datastores that incorporate network inputs and desired network responses after this section. It may also be used to train semantic segmentation networks with pixel label data and ground truth images. The patch sizes are 36*36*155 and 40*40*155, respectively, and there are 80 and 90 patches per image. These patch sizes were chosen to simplify the deep learning network and improve its performance as much as feasible due to memory issues. Patch sizes with these measurements demonstrate the best outcomes as a result of several testing.

Combined Slices
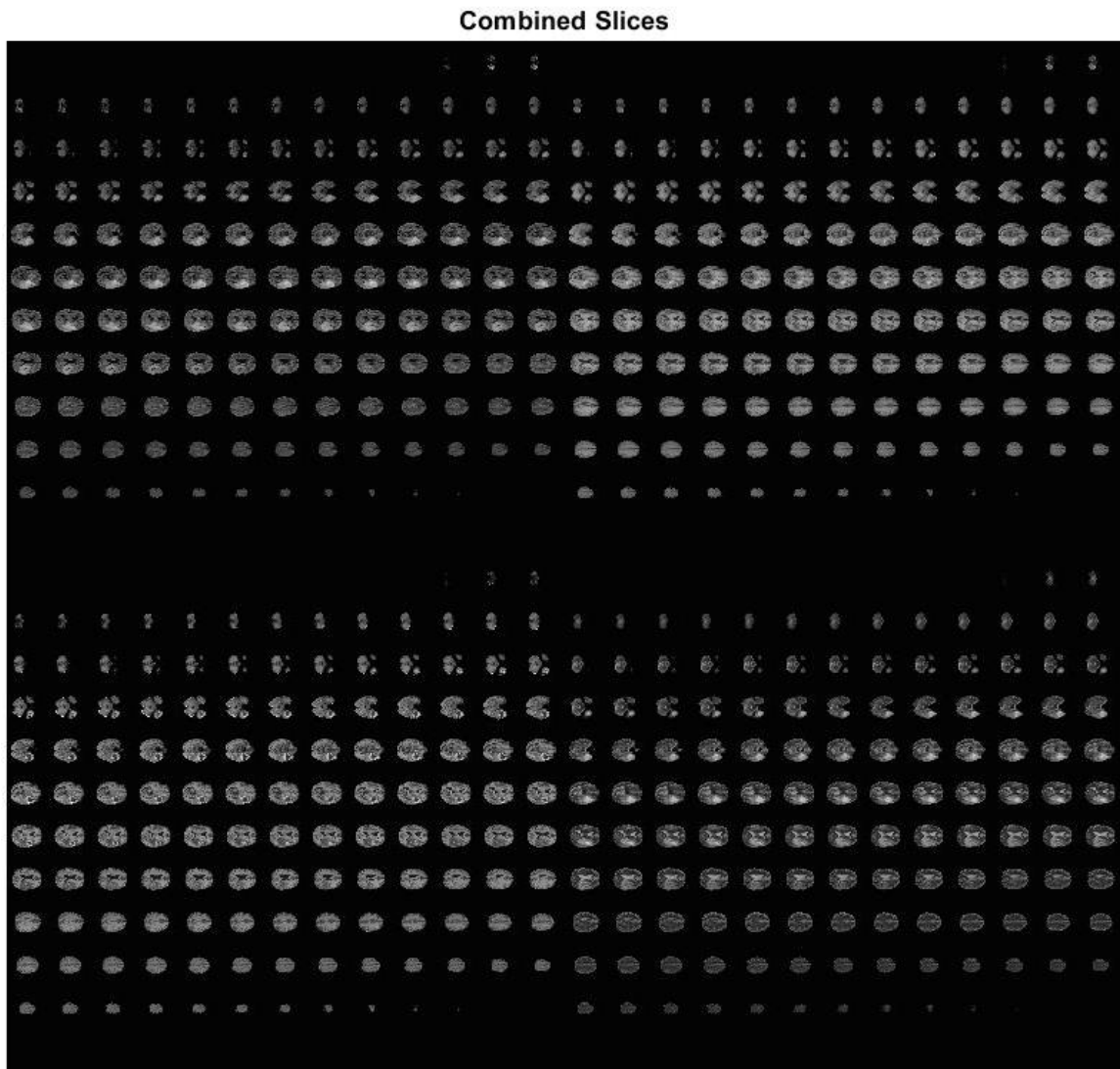
Figure 3.6. All MR images consisting of 155 slices with four modalities: T1, T1C, T2, and FLAIR.

3.3. The Deep Learning Network

Convolution and transposed convolution layers were used to perform downsampling and upsampling operations in our proposed deep learning network (Figure 3.7). Then, using the network whose simplified structure is shown in Figure 3.8, semantic segmentation was applied to test images.

The obtained patches are fed into a deep learning network as an input image. Convolution layers are applied to images with 12 filters that have dimensions of 4*4*4 due to strong performance findings acquired following an experimental phase. It was also planned to conduct a more

thorough investigation, taking into account the tumor measures. It was also intended to perform a more detailed analysis, considering the tumor measurements. The 3D max-pooling layer was used to conduct down-sampling by dividing the 3D image into cuboidal regions.
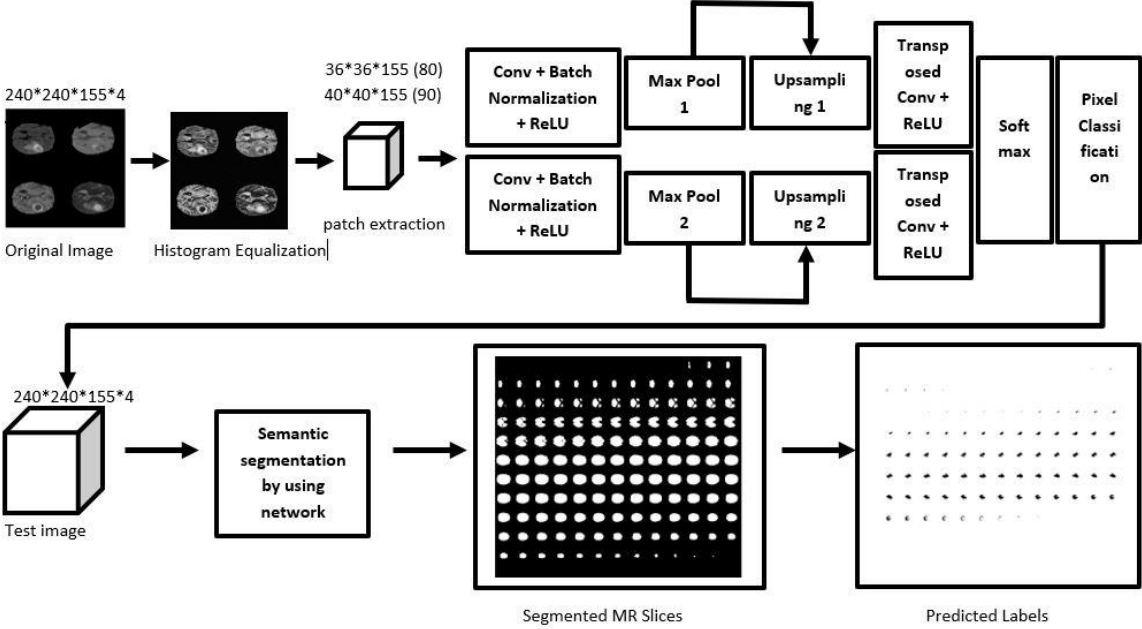
Figure 3.7. Architecture of deep learning network and semantic segmentation.
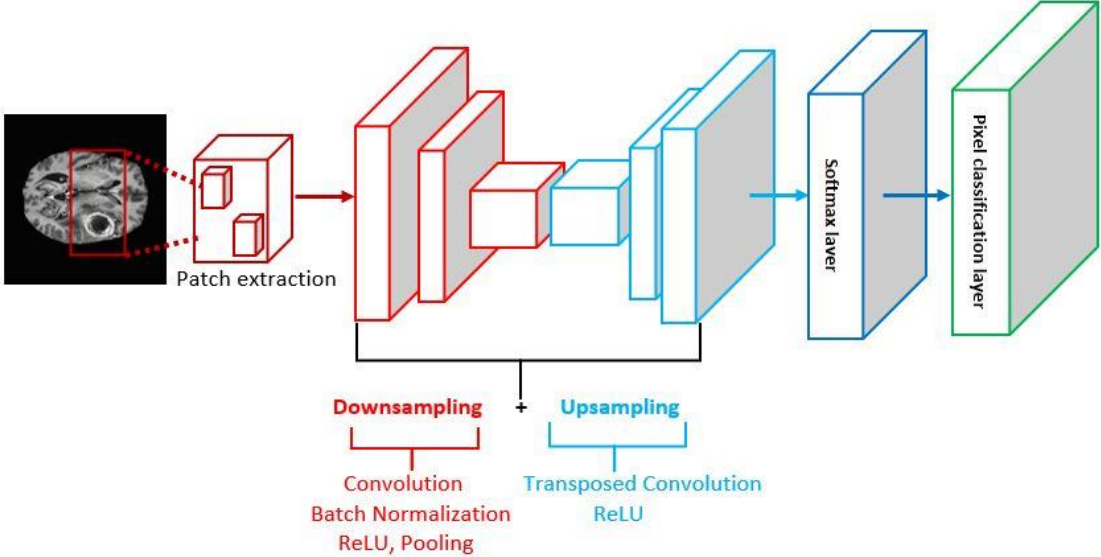
Figure 3.8. Simplified representation of deep learning network for the proposed study.

The training process of this deep learning network was carried out by using MATLAB and it is approximately required 3-hour training for the image dataset. An example of the training process is shown in Figure 3.9.
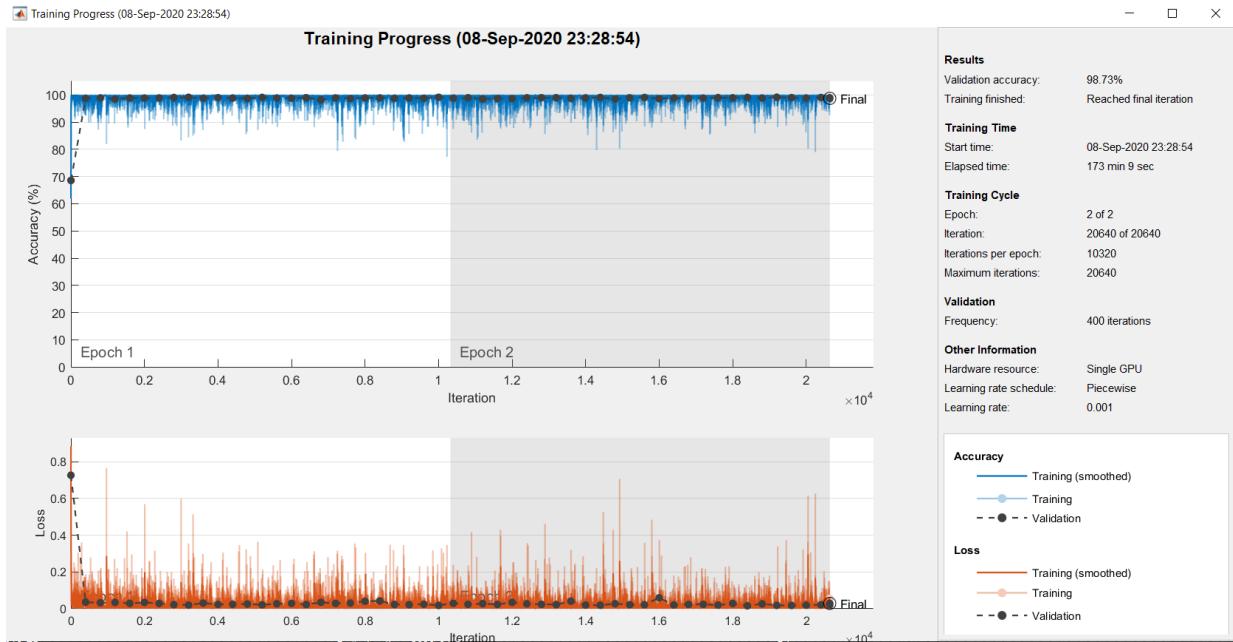
Figure 3.9. Illustration of the training process for the image dataset

When training networks for deep learning, it is normal to keep track of their development. It can be learned how the training is going by plotting different metrics during the training. It can also be seen how quickly the network's accuracy is improving, as well as if the network is beginning to overfit the training data [83]. Each iteration requires a gradient estimate and a network parameter update. If validation data is stated as a training option, validation metrics are displayed in the figure each time network is going to be validated. In Figure 3.9, many different types of metrics can be observed, and these can be listed as following: *Training accuracy* represents classification accuracy on each individual mini-batch. *Smoothed training accuracy* is achieved by smoothing the training accuracy using a smoothing algorithm. It has a lower noise level than unsmoothed accuracy, making it easier to identify patterns. *Validation accuracy* is classification accuracy on the entire validation set. *Training loss, smoothed training loss, and validation loss* are responsible for the loss on each mini-batch, its smoothed version, and the loss on the validation set, respectively [84].

In the training process of our deep learning network, a stochastic gradient descent algorithm was used. Stochastic gradient descent is a well-known and commonly used algorithm in various Machine Learning algorithms, and it is the base of Neural Networks [85]. In simple terms, gradient refers to the slope or slant of a surface. Consequently, gradient descent involves descending a slope to the lowest point on the earth. Consider a two-dimensional graph, such as the parabola shown in the diagram below.
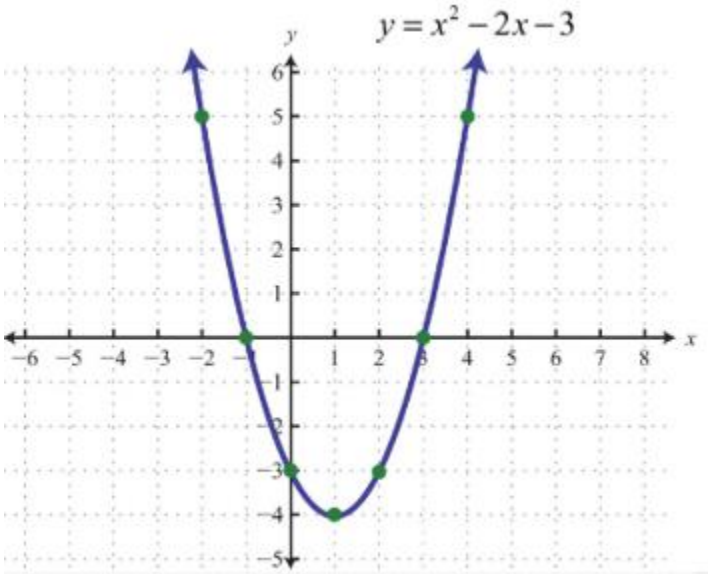
Figure 3.10. A graph regarding gradient descent [85]

The lowest point on the parabola is at x = 1 in the graph above. The gradient descent algorithm aims to find the value of "x" that minimizes "y." The objective function that the gradient descent algorithm uses to descend to the lowest point is referred to as "y." Gradient descent is an iterative algorithm that begins at a random point on a function's slope and works its way down until it reaches the function's lowest point. When the optimal points cannot be identified by equating the function's slope to 0, this algorithm comes in handy. In the parabola above, the number of squared residuals can be mentally mapped as the function "y" and the weight vector as "x" in linear regression [86].

By taking small steps in the direction of the loss function's negative gradient at each iteration, the standard gradient descent algorithm updates the network parameters (weights and biases) to minimize the loss function [87].

$$\emptyset(k + 1) = \emptyset(k) - a\nabla E(\emptyset(k)) \qquad (6)$$

According to Eq.6, the iteration number is k, the learning rate is a>0, the parameter vector is $\emptyset$, and the loss function is E($\emptyset$). The gradient of the loss function, $\nabla E(\emptyset)$, is calculated using the entire training set in the conventional gradient descent algorithm, and the standard gradient descent algorithm uses the entire data set at once.

The stochastic gradient descent algorithm, on the other hand, evaluates the gradient and updates the parameters using a subset of the training data for each iteration. Each iteration uses a different subset, known as a mini-batch. One epoch represents a complete transfer of the training algorithm over the entire training set using mini-batches. Since the parameter updates computed using a mini-batch are a noisy approximation of the parameter update that would result from using the entire data set, stochastic gradient descent is stochastic. The 'MiniBatchSize' and 'MaxEpochs' name-value pair arguments can be used to determine the mini-batch size and the maximum number of epochs, respectively.

3.3.1.Down-sampling

Image downsampling is completed by max-pooling layers, which are put into the network after convolution, batch normalization, and relu layers. Fundamentally, the goal of these layers is to handle data of a more manageable scale, minimize data storage size, and provide faster image processing time by lowering input data dimensions. Eq. 7 displays the convolution layer formula (1). Dimension filters (F) were used to create a three-dimensional image (I) [88].

$$O(i, j, k) = \sum_m \sum_n \sum_p I(m, n, p) F(i - m, j - n, k - p) \qquad (7)$$

In Eq. (7), the matrix form is defined as follows: Scale of input matrix (number of images) x (width (w)) x (height(h)) x (depth(d)), where w and h correspond to the number of convolution filters and d to the filter depth [89].

3.3.2.Up-sampling

For upsampling the data's 3D feature charts, transposed convolution layers are applied to the neural network. As a result, the image's size can be increased at the end of these layers. For the deconvolution operation, the same size filters were used as in the convolution layers. The deep learning network's final layer is the pixel classification layer, which assigns a categorical mark to each image pixel or voxel so that semantic segmentation can be performed.

Considering upsampling, which has an inverse objective of downsampling, it is aimed to increase the image's dimensions and fill in the holes (columns/rows) in some way. Applying to upsample operation to the original image by a factor of three, it is required to use logic to add two more rows/columns for each row/column in the image (Figure 3.11). One alternative is to simply replicate each column/row in the original image [90].
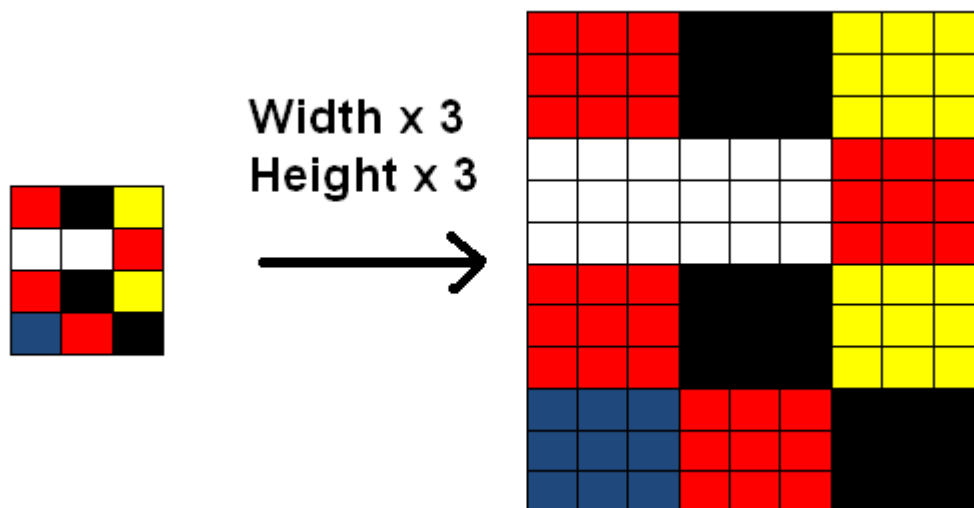
Figure 3.11. Simple representation of up-sampling [90]

Upsampling is the method of increasing spatial resolution while preserving the image's 2D representation. It's widely used for zooming in on a single area of an image and removing the pixelation effect that happens when a low-resolution image is viewed on a wide frame [91].

3.3.3.Semantic segmentation by using the network

Semantic segmentation is the process of matching each pixel of an MR brain image with a class label such as background or tumor. A deep learning network and semantic segmentation are used to classify every pixel in an image. As a result of this procedure, images are segmented into classes[92]. Our method uses a deep learning architecture to create a neural network and apply semantic segmentation to MR images. The downsampling of an image between convolutional and ReLU layers, as well as output upsampling to fit the input size, is a common structure used in semantic segmentation networks.

3.3.4.Evaluation metrics

Several metrics were used to evaluate the segmentation performance, including global accuracy, mean accuracy, mean IoU, weighted IoU, mean BF score, and dice-index. The development of a confusion matrix is another evaluation operation for pixel classification according to classes [93]. The instances in a predicted class are represented by the rows of the confusion matrix, while the instances in a true class are represented by the columns (Table 3.1).

Table 3.1. Class confusion matrix for pixel classification based on tumor and background.

		True class	
		P (Background)	N (Tumor)
Predicted class	P (Background)	True Positive (TP)	False Positive (FP)
	N(Tumor)	False Positive (FN)	True Negative (TN)

3.4. 3D Imaging with MR Slices

In the final part of our research, we compared the similarities and tumor structure in terms of presenting tumor dimensions such as width, height, and depth using 3D imaging of the entire brain, ground truth, and predicted labels. In addition, 3D brain imaging with accurate tumor location can support surgeons in improving treatment options and extending academic research in the field of medical imaging. We aimed to see if any whole brain tumors were using semantic segmentation and a deep learning network. Our evaluation results show that we are capable of

detecting brain cancers with remarkable precision and accuracy. In addition, 3D imaging of the brain tumor region was performed using three distinct imaging planes.

3.5. Surface Area Calculation by Using MR Slices

An algorithm for the calculation of surface area involves calculating the area of all of the pixels in the image by summing the areas of each pixel in an image. The region of a single-pixel is measured by looking at its two-by-two neighbors. There are six distinct patterns, each of which represents a different area:
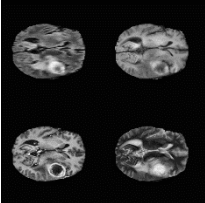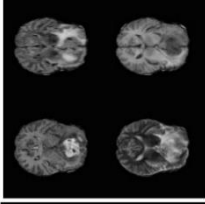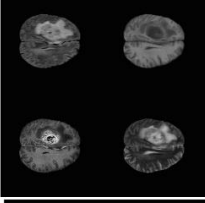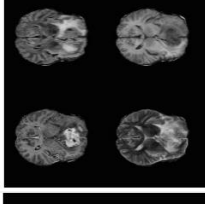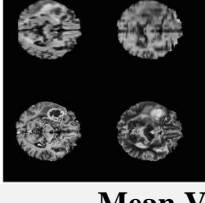
- Patterns with a pixel area of zero (area = 0)
- Patterns of one pixel per square inch (area = 1/4)
- Patterns with two adjacent pixels on the same pixel (area = 1/2)
- Pixel patterns with two diagonals (area = 3/4)
- Three-on-pixel patterns (area = 7/8)
- Patterns on pixels for all four (area = 1)

Each pixel is divided into four 2-by-2 neighborhoods. This means that a single on pixel surrounded by off pixels, for instance, has a total area of 1 [94].

4.RESEARCH FINDINGS

A total of 257 BraTS image data sets were used in this study to train a deep learning network by using semantic segmentation. We used training, validation, and test images to predict labels and compare them to ground-truth labels in order to apply semantic segmentation with the deep learning technique. After the training phase was completed, 5 separate data sets containing 155 MR slices with tumor were utilized. Table 3 shows the evaluation results of our model, which includes many semantic segmentation metrics.

Table 4.1. Evaluation results of our proposed model for 5 different MR test images

Input Image Size (240*240*155*4)	Patch Size	Patch per image	Background Prediction (%)	Tumor Prediction (%)	Mean Accuracy (%)	Mean IoU (%)	Weighted IoU (%)	Mean BF Score (%)
	36*36 *155	80	99.84	87.93	93.89	84.7	99.59	94.93
	36*36 *155	80	99.56	95.03	97.29	86.07	99.1	88.28
	40*40 *155	90	99.71	97.83	98.77	88.12	99.45	94.85
	40*40 *155	90	99.78	87.42	93.6	87.75	99.26	91.84
	40*40 *155	90	99.89	90.38	95.14	88.09	99.71	94.79
Mean Values (%)			99,756	91,718	95,738	86,946	99,42	92,938

According to the findings, the average tumor prediction was 91.72, and the average background prediction was 99.75. Other measurements for the five images were 95.74, 86.95, and 99.42, respectively, for mean precision, mean IoU and weighted IoU. One of the most important metrics, the Mean BF Score, was determined to be 92.94.

As shown in Table 3, semantic segmentation metrics were used to evaluate test images. These images were also subjected to image analysis, with the results displayed to show segmented images, a comparison of ground truth and projected labels and a similarity ratio between these labels. Figures 4.1, 4.3, 4.5, 4.7, and 4.9 depict all of these findings. Figures 4.2, 4.4, 4.6, 4.8, and 4.10 indicate the similarity between labels with dice scores centered on 8 slices for the purpose of showing the resemblance between labels with dice scores.
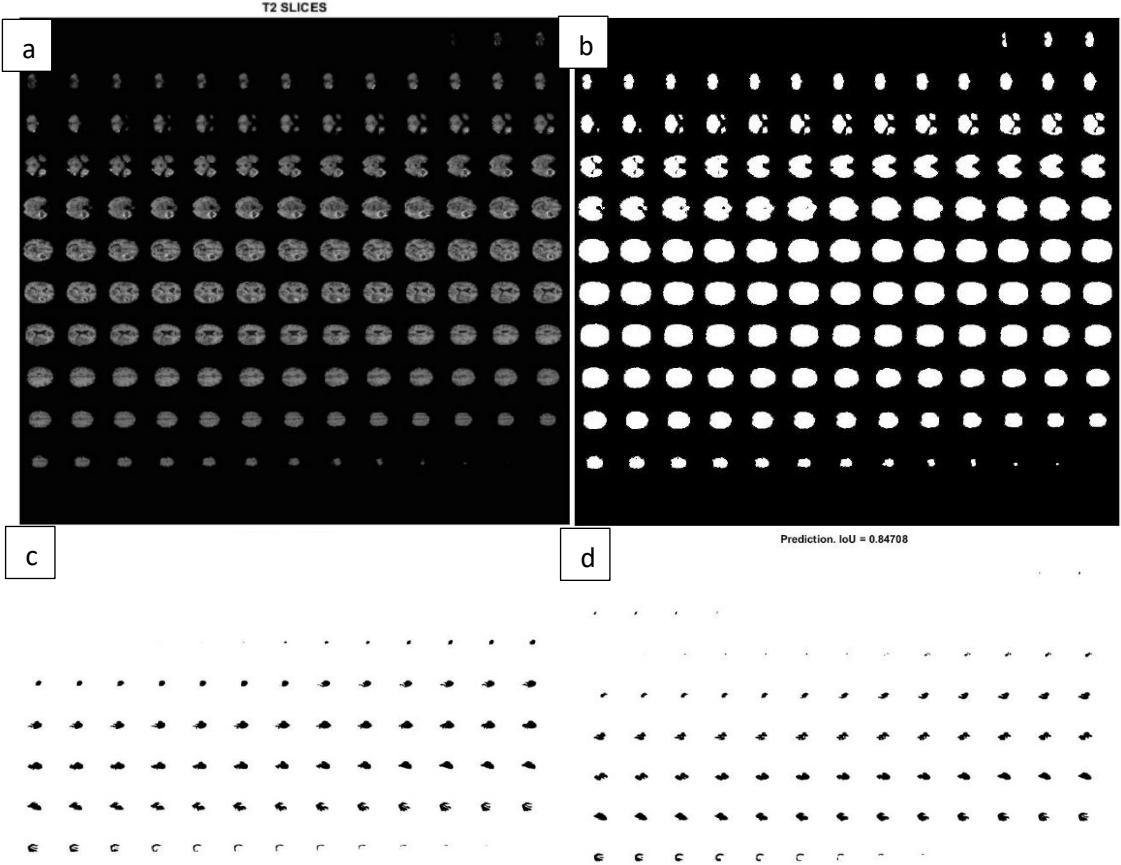
Figure 4.1. Semantic segmentation results of the first image including ground truth and predicted labels with IoU ratio as 84.71 a) original MR slices (T2), b) segmented MR slices, c) ground truth labels, and d) predicted labels.
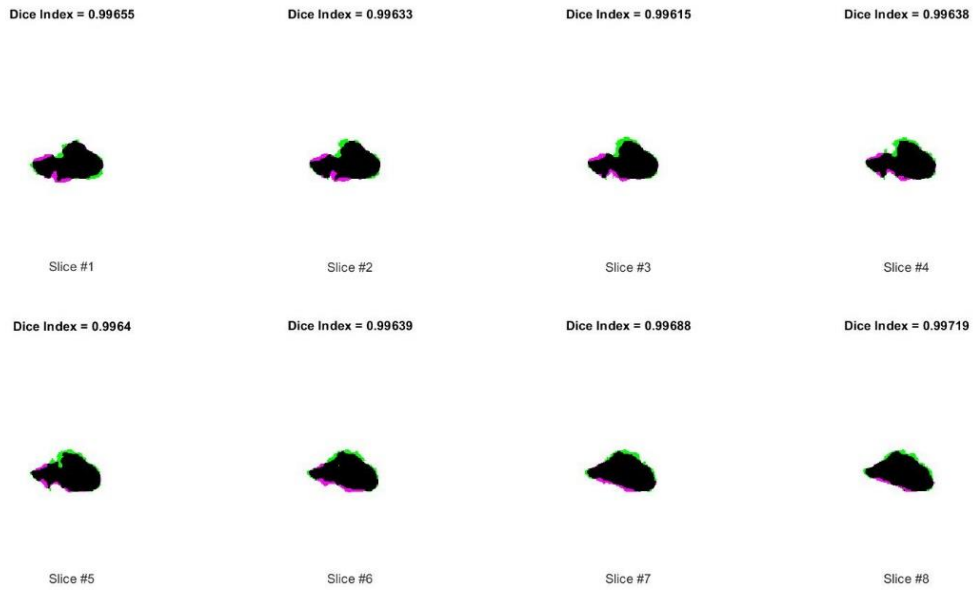
Figure 4.2. Similarity ratios with dice scores of the first test image.
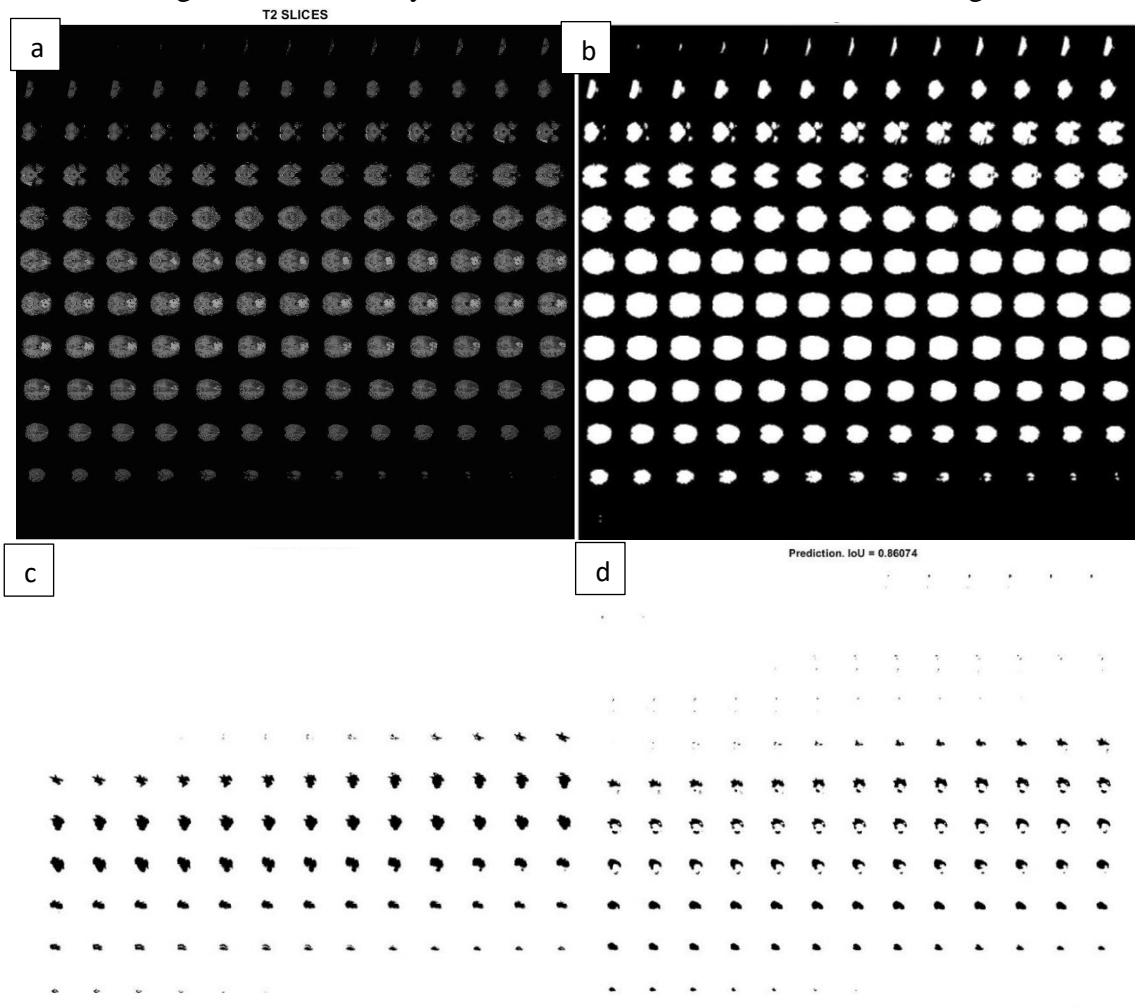
Figure 4.3. Semantic segmentation results of the second image including ground truth and predicted labels with IoU ratio as 86.07 a) original MR slices (T2), b) segmented MR slices, c) ground truth labels, and d) predicted labels.
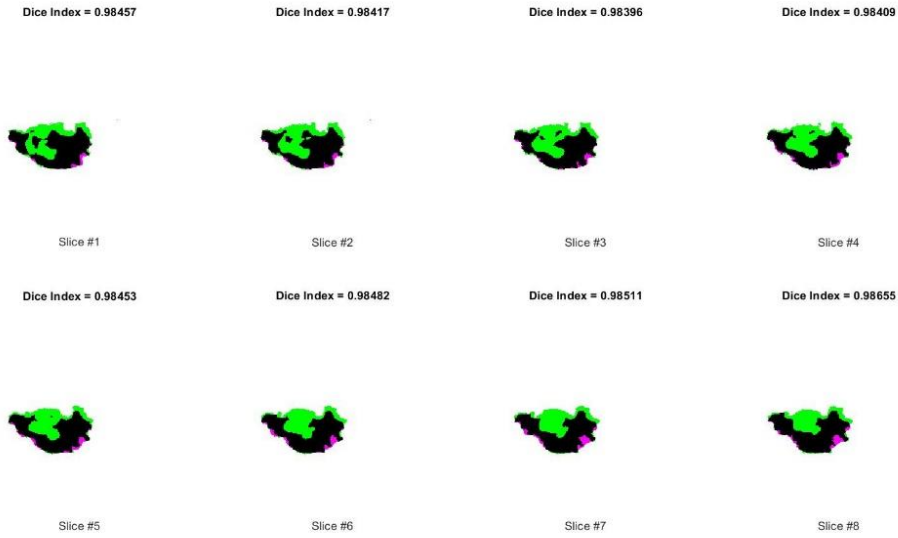
Figure 4.4. Similarity ratios with dice scores of the second image.
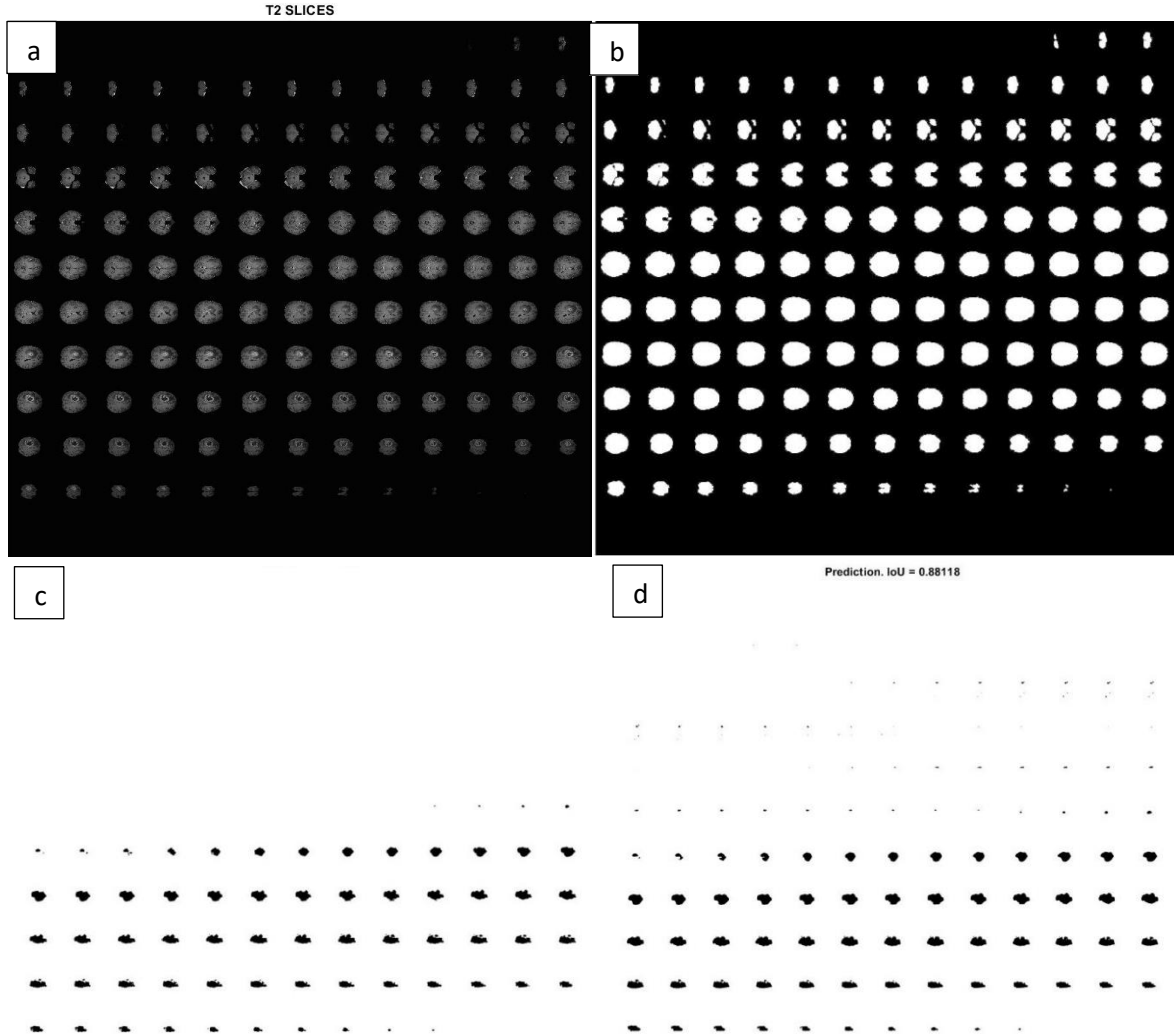
Figure 4.5. Semantic segmentation results of the third image including ground truth and predicted labels with IoU ratio as 88.12 a) original MR slices (T2), b) segmented MR slices, c) ground truth labels, and d) predicted labels.

Figure 4.6. Similarity ratios with dice scores of the third image.
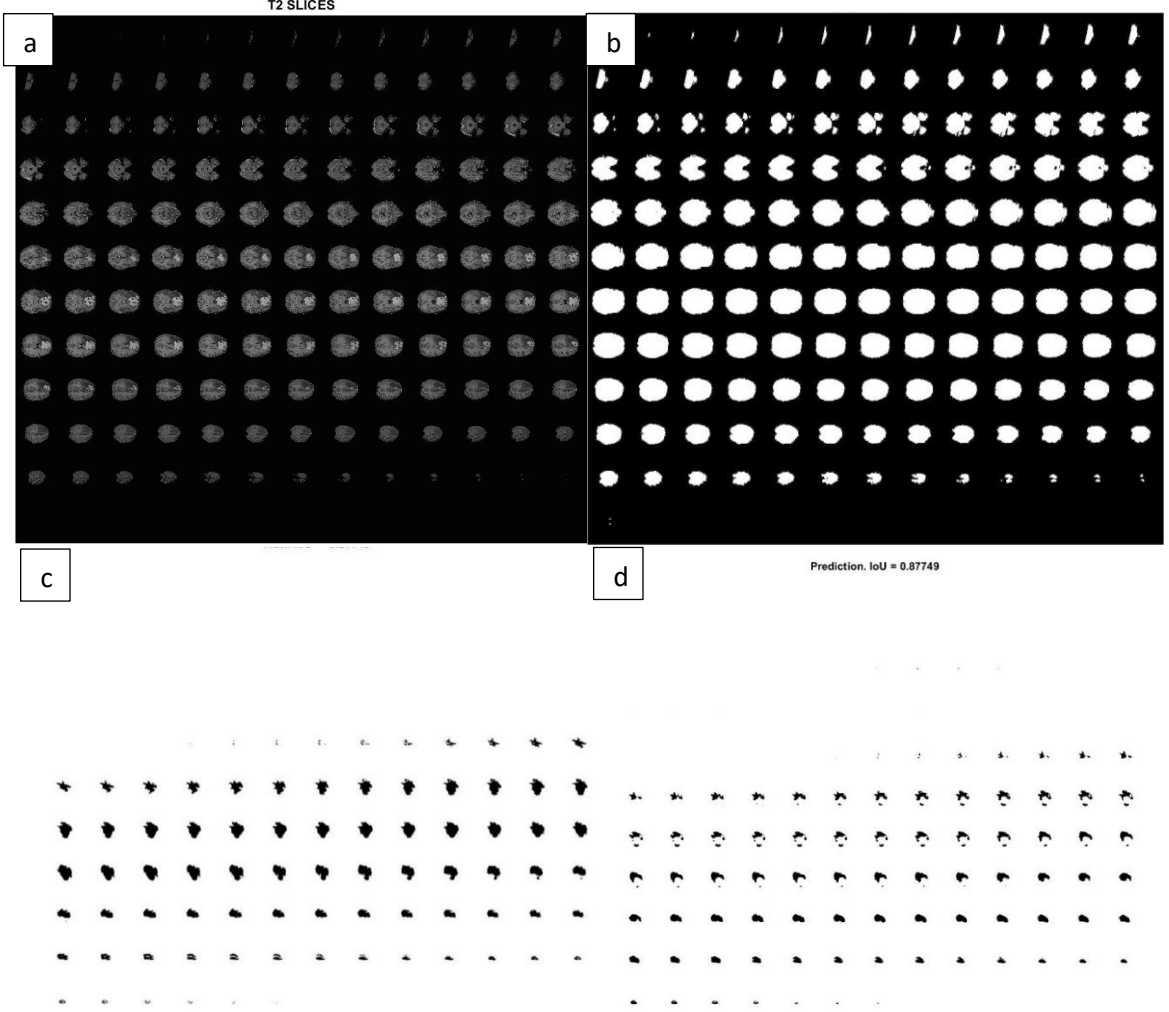
Figure 4.7. Semantic segmentation results of the fourth image including ground truth and predicted labels with IoU ratio as 87.75 a) original MR slices (T2), b) segmented MR slices, c) ground truth labels, and d) predicted labels.

Dice Index = 0.99572   Dice Index = 0.99574   Dice Index = 0.99589   Dice Index = 0.9963

Slice #1   Slice #2   Slice #3   Slice #4

Dice Index = 0.99638   Dice Index = 0.99662   Dice Index = 0.99662   Dice Index = 0.99607

Slice #5   Slice #6   Slice #7   Slice #8
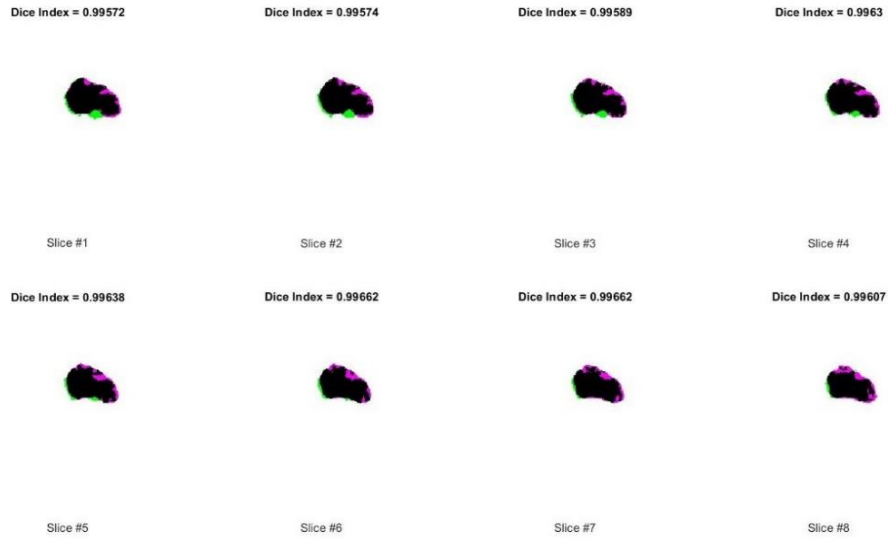
Figure 4.8. Similarity ratios with dice scores of the fourth image.
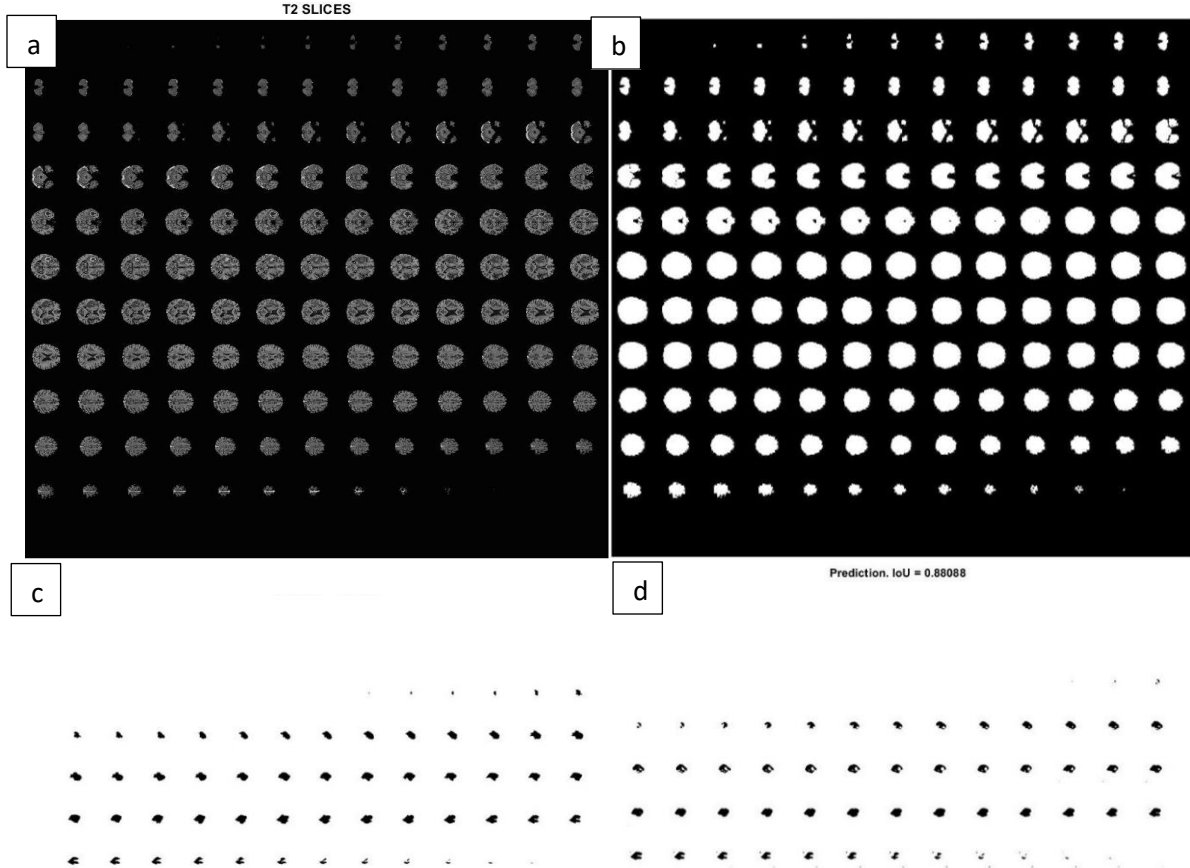
Figure 4.9. Semantic segmentation results of the fifth image including ground truth and predicted labels with IoU ratio as 88.09 a) original MR slices (T2), b) segmented MR slices, c) ground truth labels, and d) predicted labels.

51
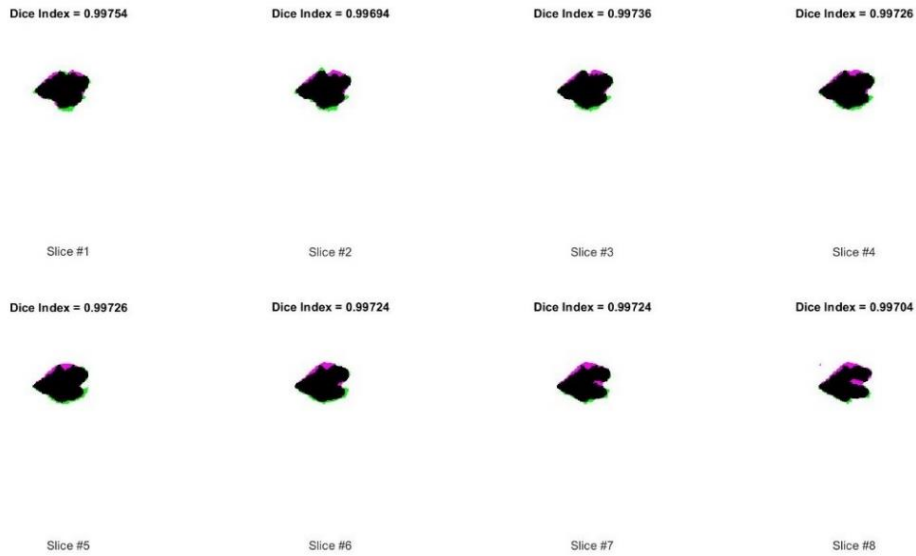
Figure 4.10. Similarity ratios with dice scores of the fifth image.

Using segmented MR slices and labels, MATLAB was utilized to perform 3D imaging of the entire brain, ground truth labels, and projected labels (Figure 4.11). To examine the similarities between ground truth and prediction, labels were put into segmented MR slices (Figure 4.12), and then a 3D brain model containing tumor was generated to assess tumor measures more precisely (Figure 4.13).
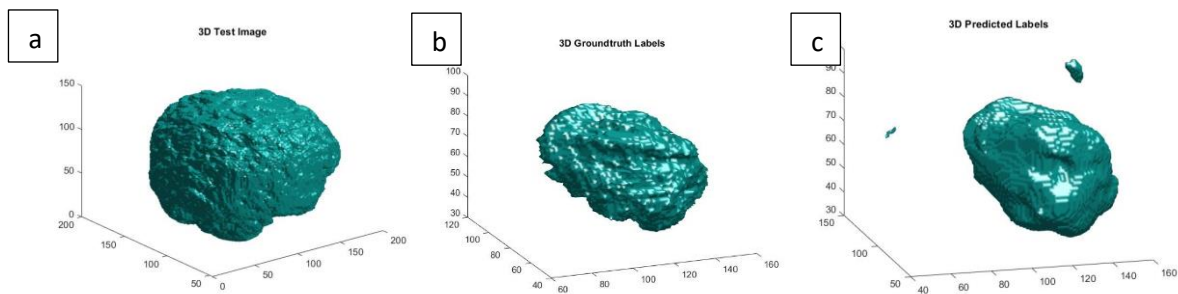
Figure 4.11. An example for displaying in 3D, a) whole brain, b) ground truth labels, and c) predicted labels

The similarity between these labels and the 3D model built using them is compared when ground truth and predicted labels are incorporated into a segmented image. In order to better comprehend the specific location of the tumor, 3D models were constructed and cropped using MATLAB's 3d picture cropping function. These images were shown in three imaging planes: coronal (Figure 4.14), sagittal (Figure 4.15), and axial (Figure 4.16). They depict the tumor's position and provide details on the tumor's measurements, such as its height, width, and depth.
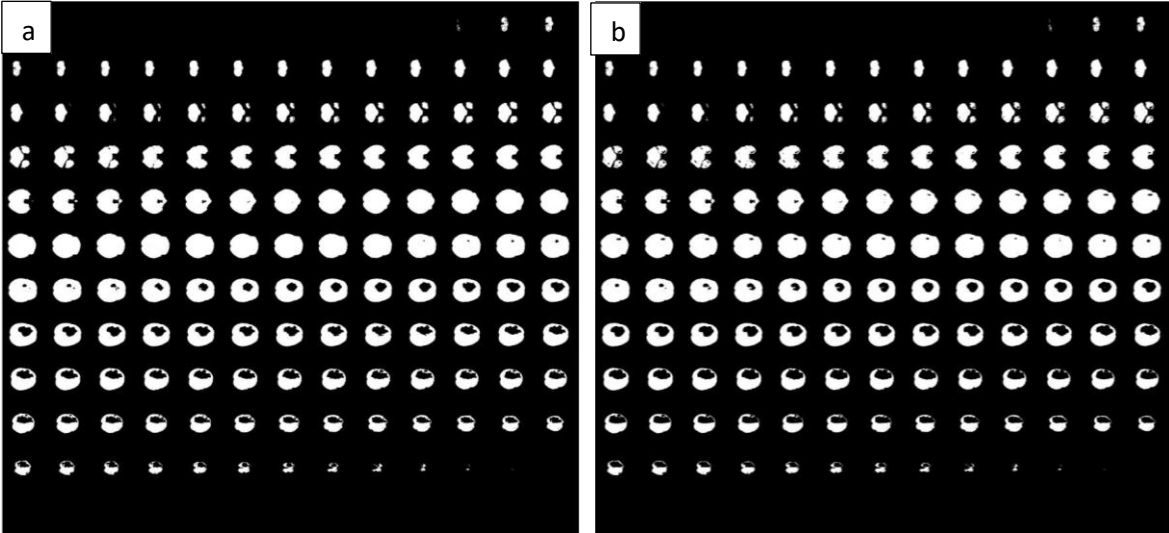
Figure 4.12. Label insertion into segmented MR slices, a) MR slices with ground truth labels, b) MR slices with predicted labels.
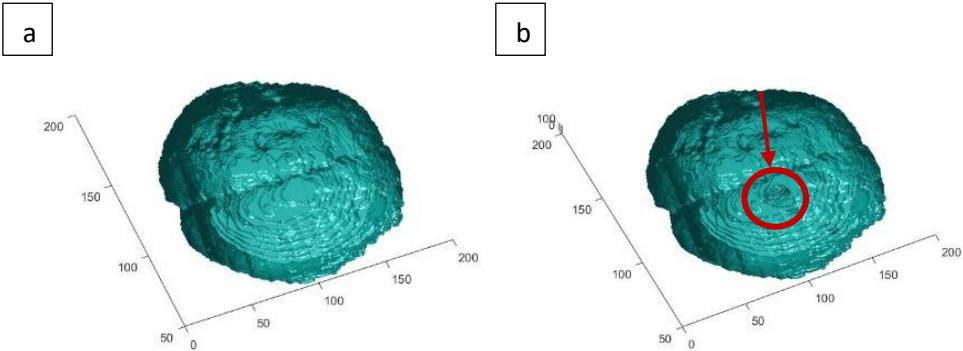
Figure 4.13. 3D MR brain image display by using label inserted slices a) ground truth labels, b) predicted labels (axes represent the pixel number).
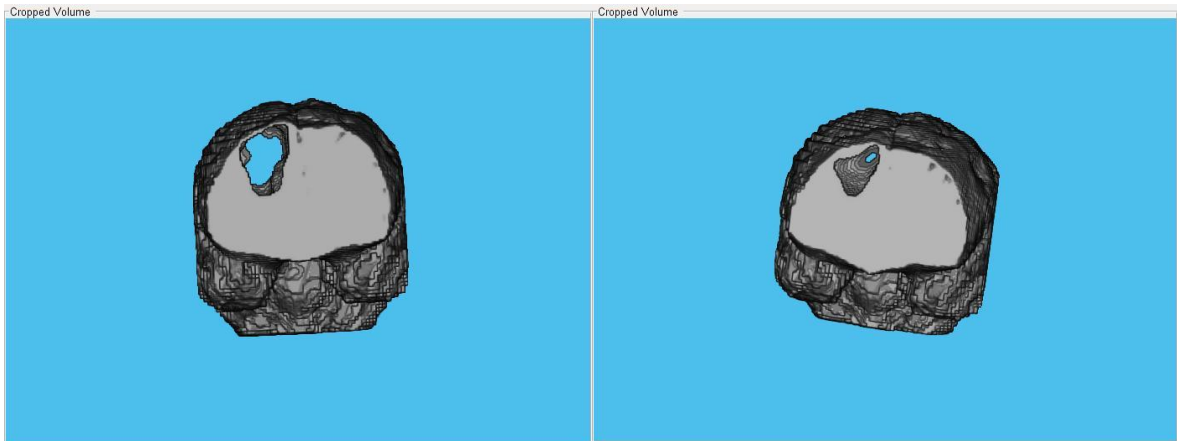
Figure 4.14. 3D representation of exact tumor region on the coronal plane.
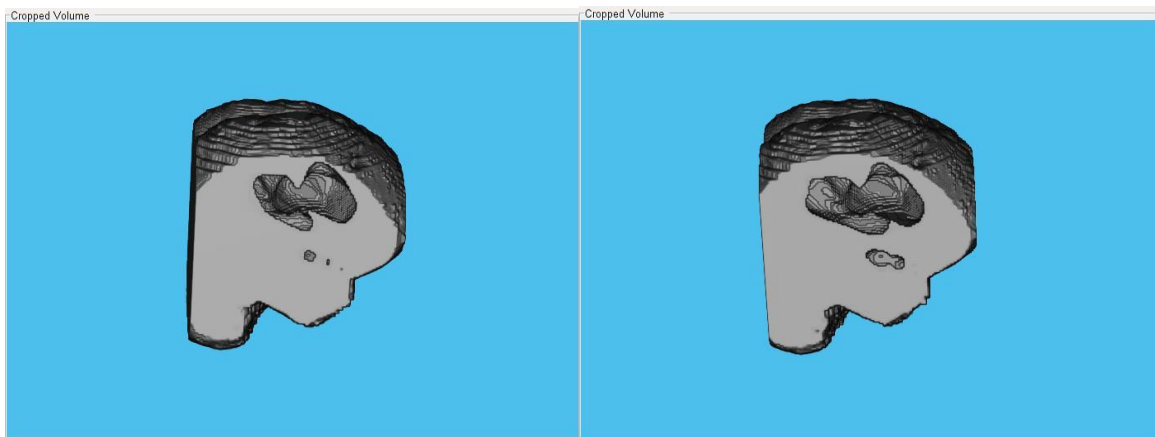
Figure 4.15. 3D representation of exact tumor region on the sagittal plane.
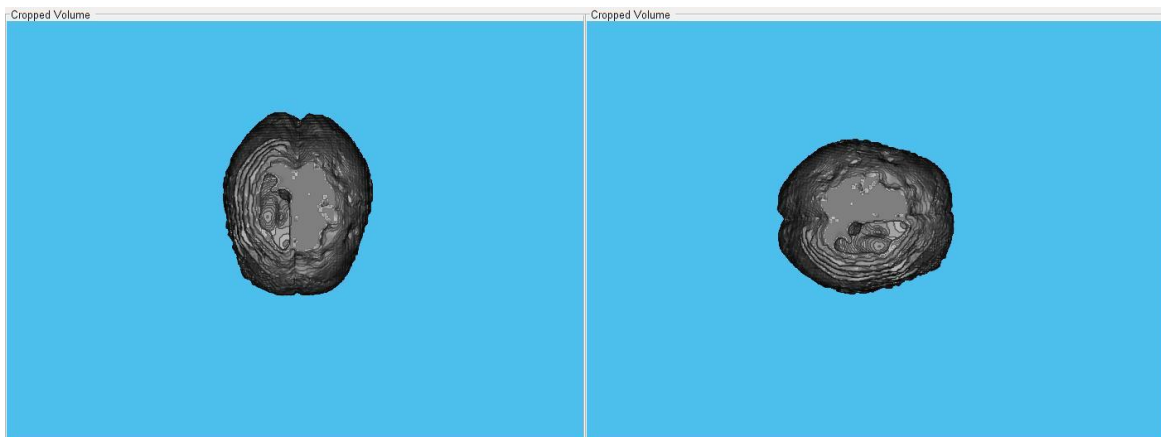
Figure 4.16.   3D representation of exact tumor region on axial plane.

This study presents a system that employs a semantic segmentation methodology with a convolutional neural network. Our proposed methodology compares ground truth and projected labels to measure background and tumor prediction using semantic segmentation on MRI data. 257 MR images with four different modalities were learned in a deep learning network. Following the successful completion of the training procedure, this neural network was fed 5 distinct MR test pictures, each with 155 slices, for semantic segmentation. The results of this semantic segmentation network indicated substantial values when it comes to analyzing segmentation metrics. As previously indicated, segmentation factors such as IoU, BF score, and dice score produce more accurate and consistent results when compared to other relevant studies. Furthermore, for background and tumor prediction, 99.76 and 91.72 were calculated, respectively. These ratios can be interpreted as critical numbers for determining the effectiveness of semantic segmentation and obtaining tumor-region information. On the other hand, when our model is run with more memory, it can be even more successful in future studies. To get around this issue, we can use an external GPU unit, which allows us to analyze and evaluate a lot more test images in a shorter period. Patch size and patch per image variables derived from original images can also be increased to improve pixel classification. As a result, a significant tumor prediction ratio can be established. Increasing the number of classes is another choice for increasing the variety of pixel classification. Since it can include more test data and classes, this approach could perform better.

Another aim of this study is to use 3D brain imaging, ground truth and predicted labels, and tumor with insertion of these labels into segmented images to get precise tumor position information. The similarity ratios between ground truth and expected labels were found to be 86.95, indicating that semantic segmentation is accurate. All 155 MR slices were used and superposed to construct a 3D brain model with a tumor. In the images mentioned earlier, it can be seen the variations between the 3D brain model with ground reality labels and the 3D projected labels.

In this study, 3-dimensional imaging of the brain and the tumor was achieved by using 155 MR slices for each image as previously stated. After this step, the calculation of the total surface area of the tumor and the comparison of the surface areas of the ground truth labeled images with the predicted labeled images were performed. In order to apply this process, the surface area of each section obtained after segmentation was calculated for the brain and labels. Surface areas, tumor prediction rates, and mean IoU metrics for 4 different MR images are given in Table 4.2.

Table 4.2. Total surface areas of related images

Images	Total surface area of brain	Total surface area of ground truth labels	Total surface area of predicted labels	False prediction ratio (%)	Tumor prediction ratio (%)	Mean IoU(%)
1	1667000 (100)	199810 (11,98%)	189550 (11,37%)	-10310 -0,61%	93,3	87,75
2	1504100 (100)	83214 (5,53%)	86830 (5,77%)	+3616 +0,24%	92,85	88,08
3	1305700 (100)	211260 (16,18%)	151840 (11,63%)	-59420 -4,55%	86,94	91,47
4	1384300 (100)	137980 (9,96%)	138230 (9,98%)	+250 +0,02%	97,83	88,12
Average	1465275 (100)	158066 (10,91%)	141612,5 (9,68%)	-16453,5 -1,23%	92,73	88,855

As seen in the table, the surface areas of 4 different MR images were calculated for the whole brain, ground truth labels, and predicted labels. At the same time, tumor prediction rates and average IoU values of 4 images are also given. The data in this table contains important information regarding the comparison of the original and predicted labels of the brain tumor and the area covered by the brain tumor. The surface area calculation made with predicted labels which are very close to the surface area of the tumor in ground truth labeled brain images also provides very important information about the size of the tumor. In addition, there are 5 different histogram figures were created regarding the data in Table 4.2. These figures can be useful for comparing the surface areas and estimating the size of the brain tumor.

The identification of false positives in semantic segmentation is generally done at the pixel level, whereas global indices like global accuracy over frames or averaged intersection over union (IoU) on the class mask level are used to measure it. As one of the causes of false-negative predictions for which the matching ground truth is underrepresented in the training data, there is a class imbalance. This is often inevitable in semantic segmentation [105].
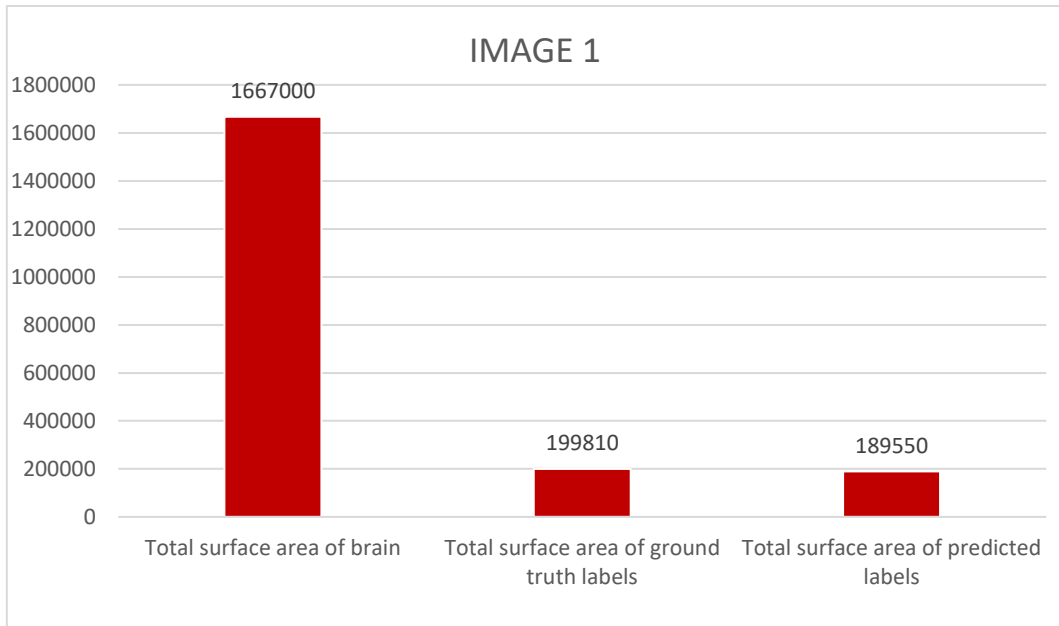
Figure 4.17. Total surface areas of the first image
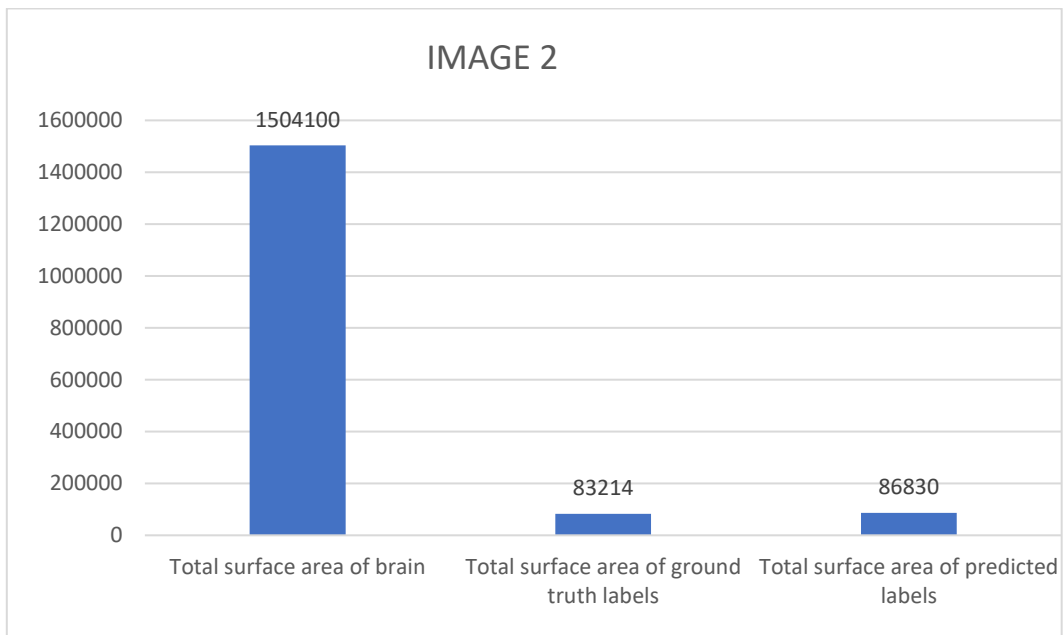
Figure 4.18. Total surface areas of the second image
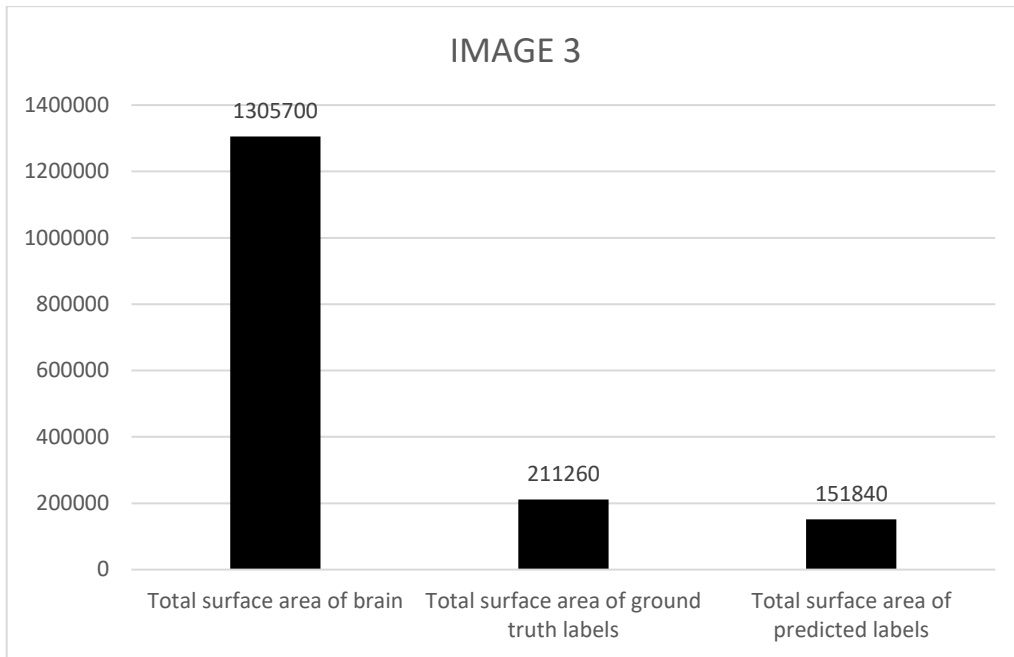
Figure 4.19. Total surface areas of the third image
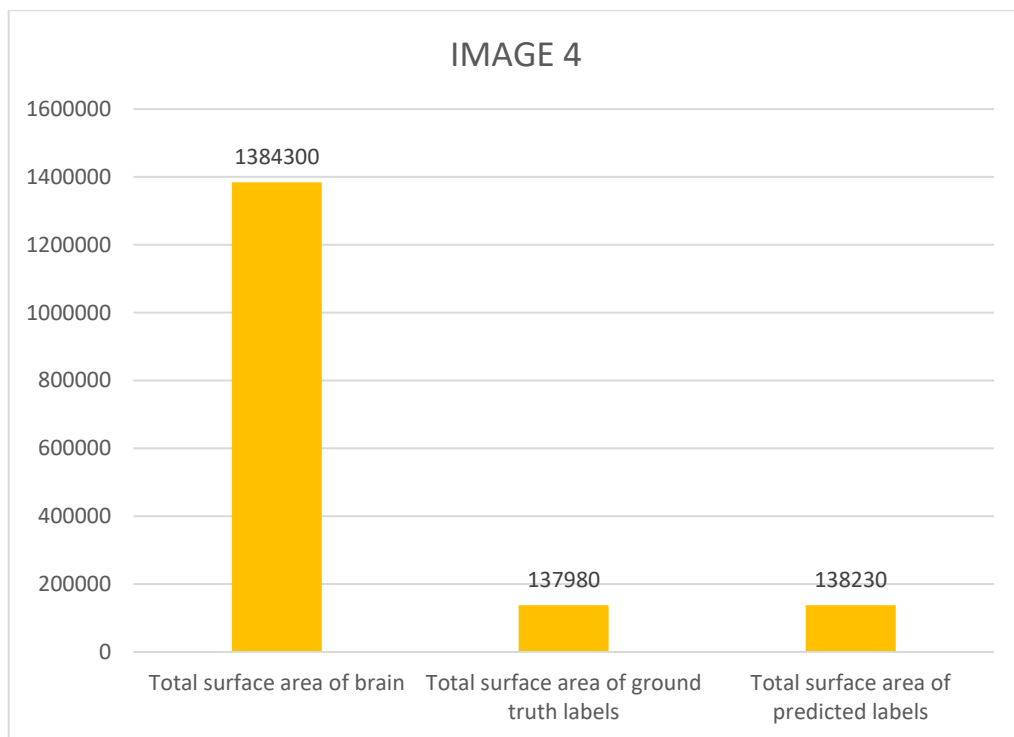
Figure 4.20. Total surface areas of the fourth image
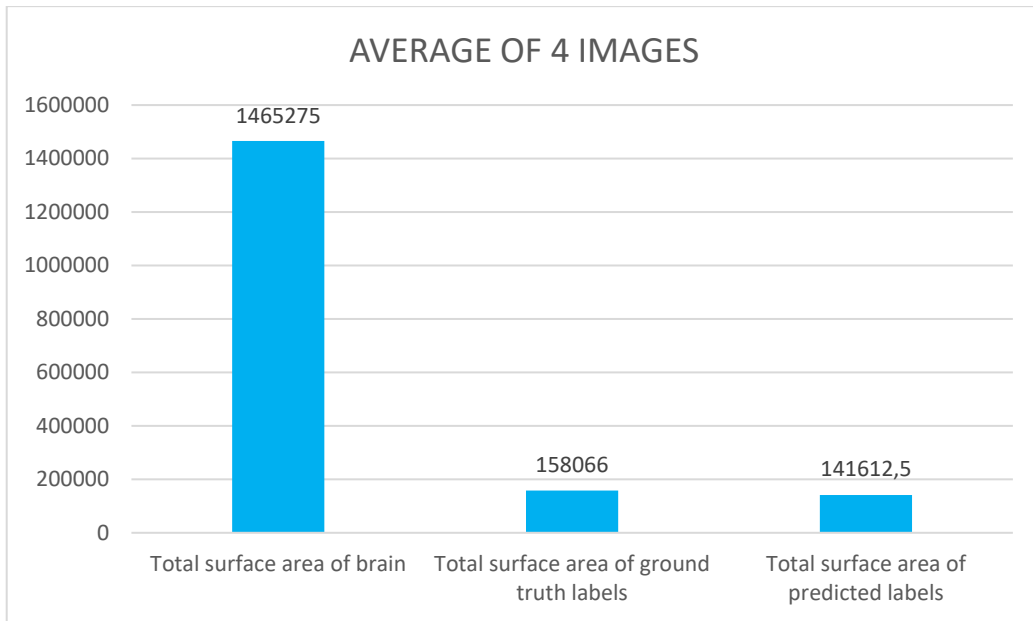
Figure 4.21. Average of total surface areas from 4 images

In these 4 MR brain images used to calculate the total surface areas, the areas of each of the 155 sections were calculated over binary images. Also, the segmented versions of each slice of these images, the comparison of the ground truth, and predicted labels were performed using the dice score function. In addition, ground truth and predicted labels for each image are embedded in segmented brain images. Finally, 3D brain imaging of the tumors was performed using segmented brain sections in which the labels were embedded. By performing 3D extraction of tumors, 3-dimensional imaging of only brain tumors was provided. In the following figures, images are containing these applications for each image. Figure 4.22 shows the all-test images and their background and tumor prediction ratios with the false positive and false negative in the form of a confusion matrix. In terms of predicting the tumor, false prediction ratios were determined as 6.697, 7.146, 13.06, and 2.17, respectively. For image 1, the original slices with 4 modalities and the application of the histogram equalization for these modalities are shown in Figure 4.23.
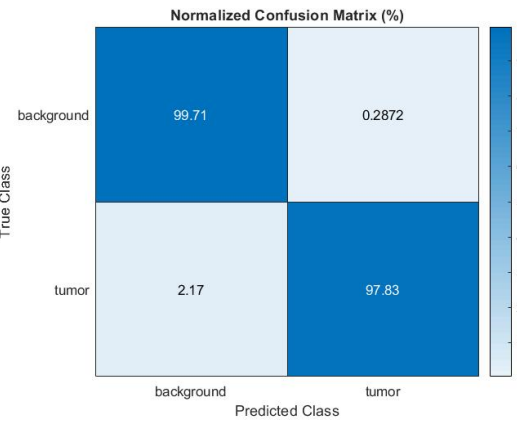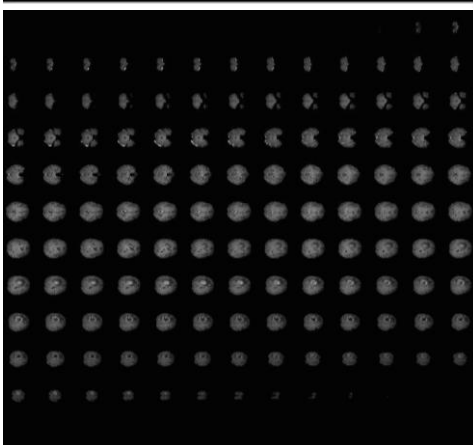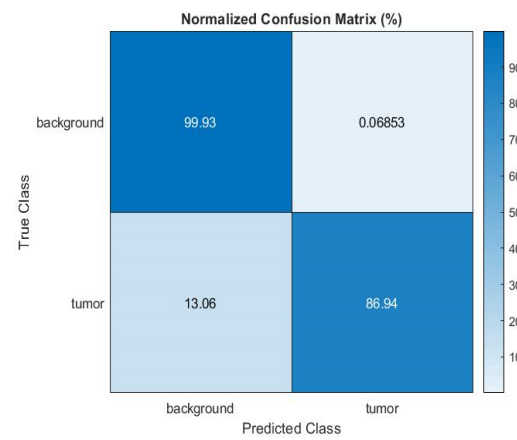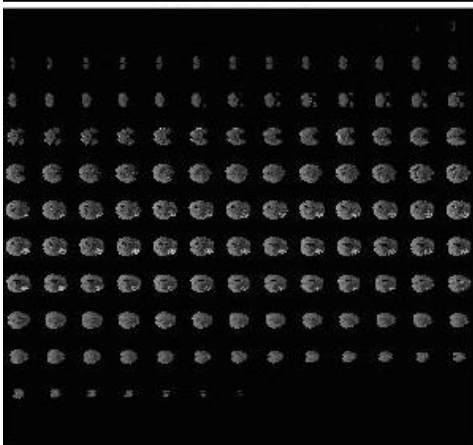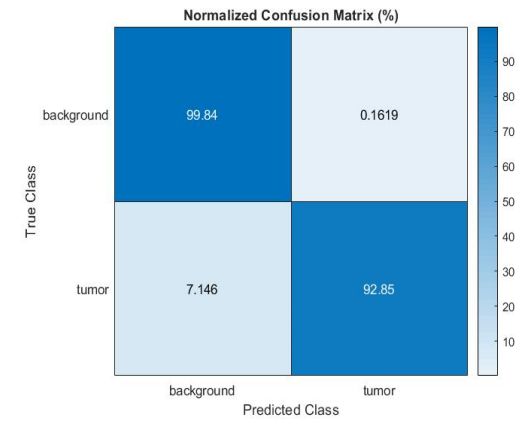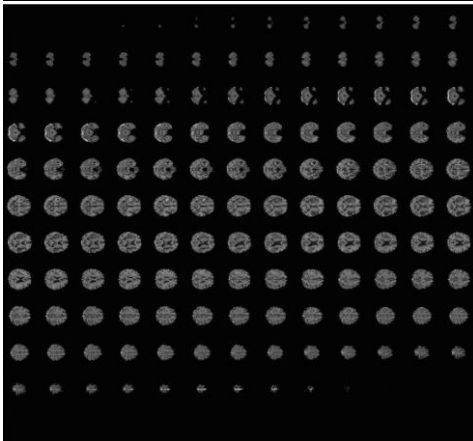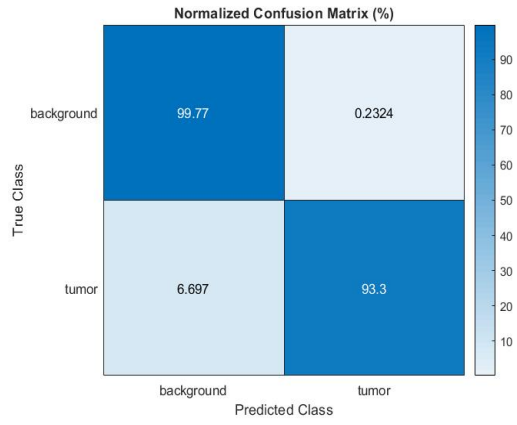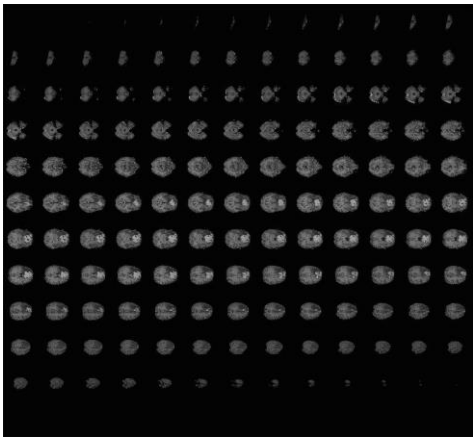
Figure 4.22. Confusion matrix results for four test images
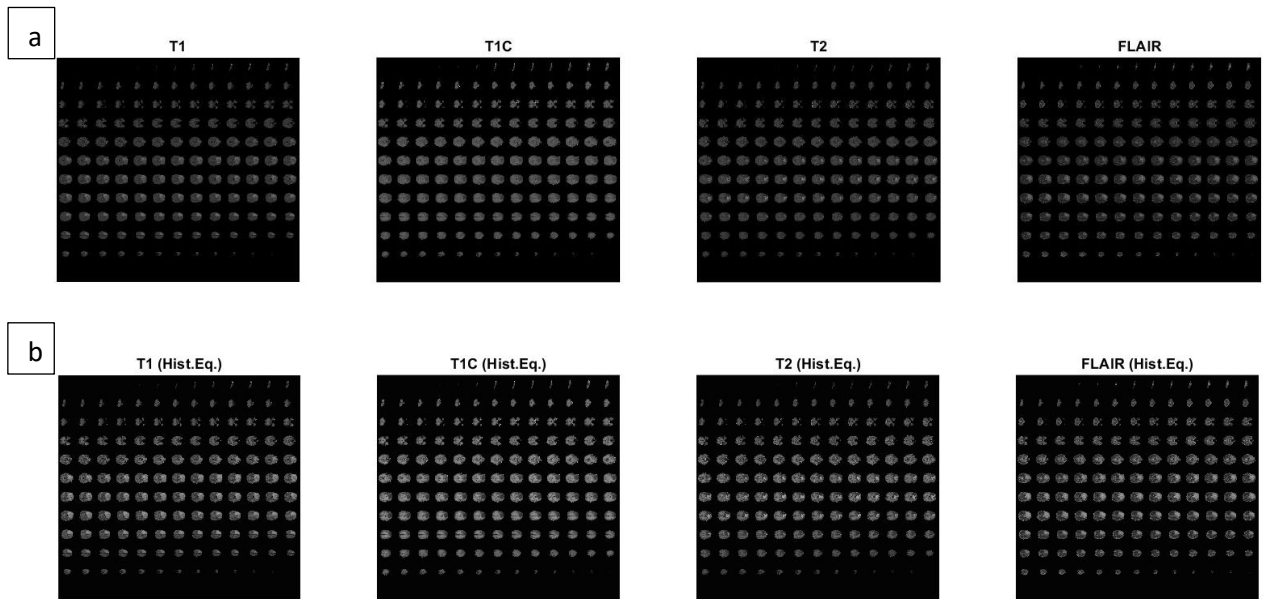
Figure 4.23. All imaging modalities for the first image, a) original slices b) histogram equalization applied
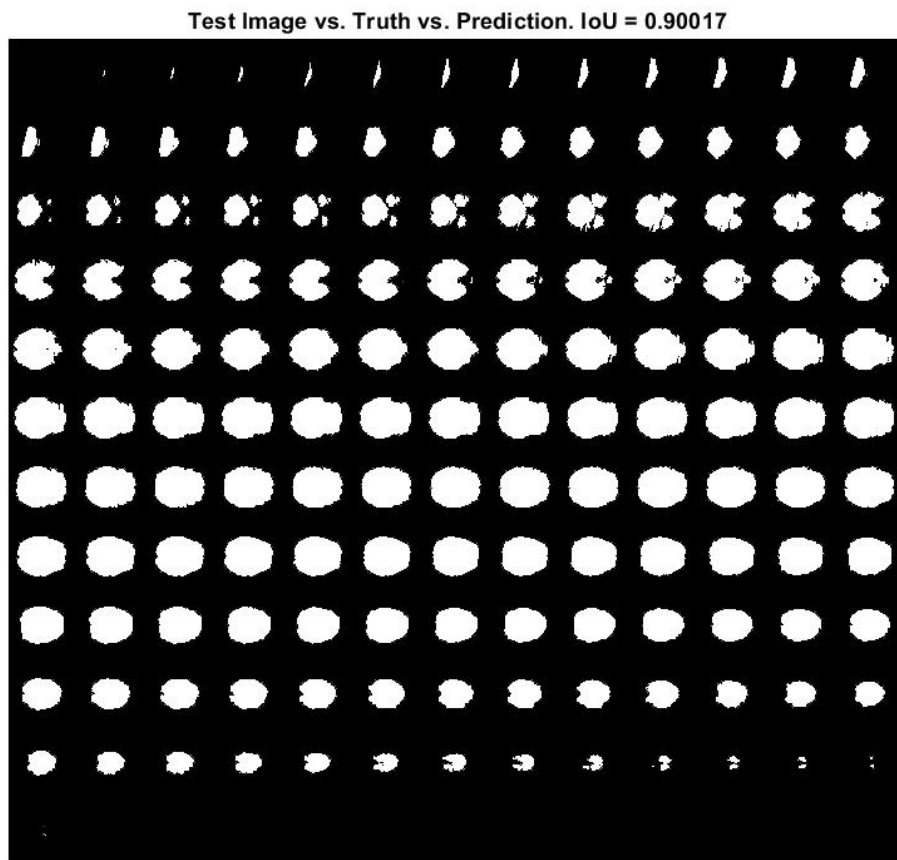
Figure 4.24. Segmented slices for the first image

Figure 4.23 represents the original MR brain images with 4 modalities and their version of histogram equalization for all 155 slices. In Figure 4.24 segmented MR brain slices are shown for the first test image.
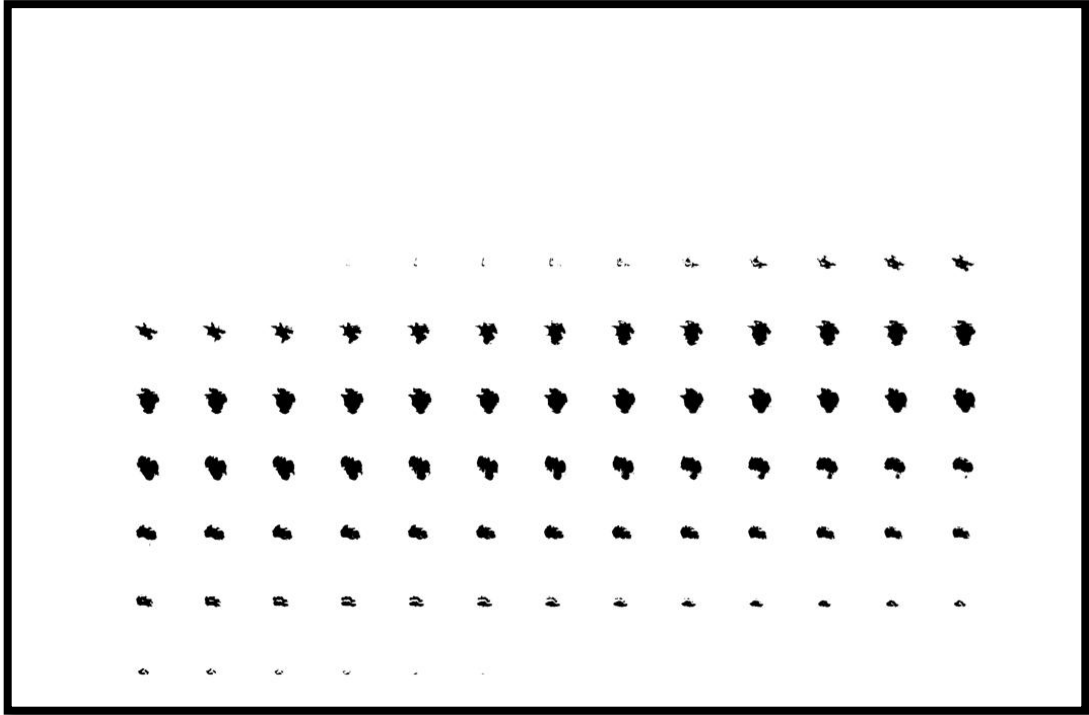
Figure 4.25. Ground truth labels for the first image
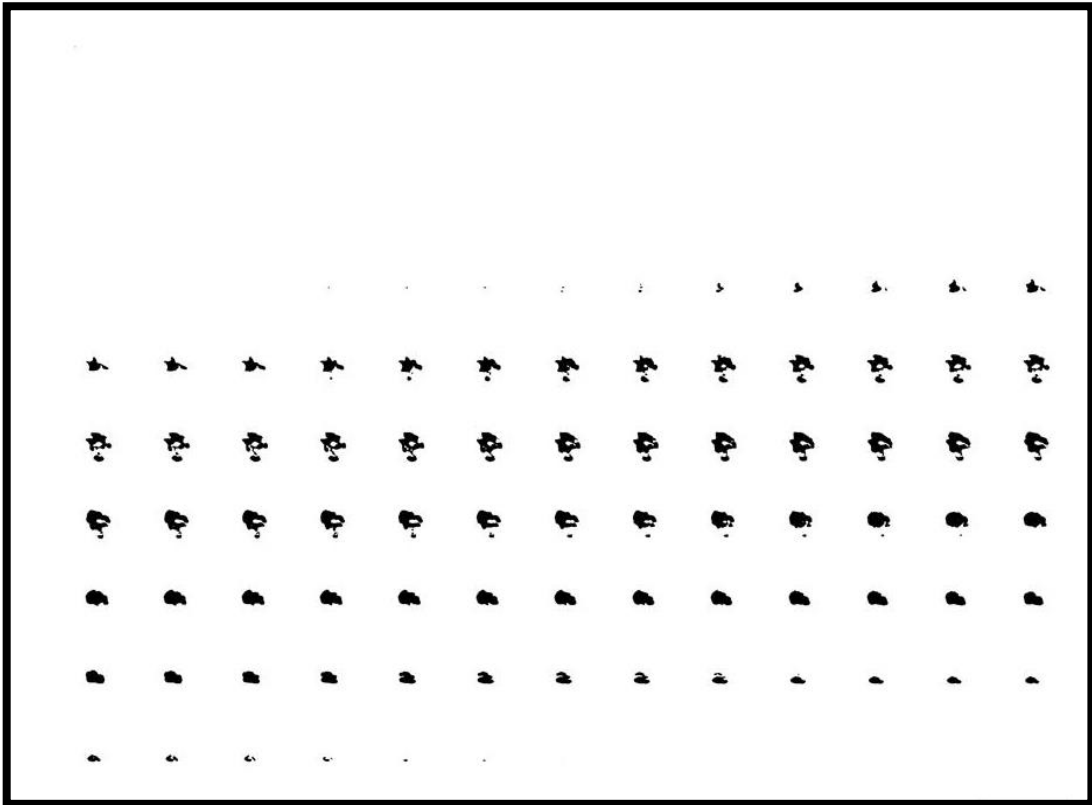
Figure 4.26. Predicted labels for the first image

Original MR slices containing ground truth labels and predicted labels which are obtained as an output of the proposed neural network can be compared in terms of resemblance for the first test image in Figure 4.25 and Figure 4.26.
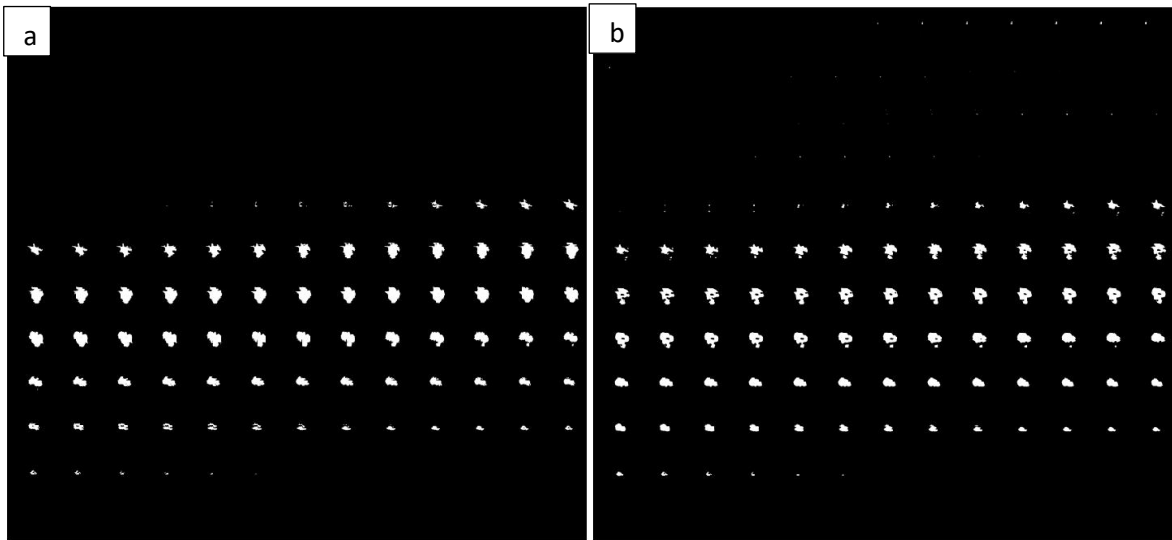
Figure 4.27. Binary versions of ground truth (a) and predicted (b) labels for the first image

Figure 4.28. Dice scores of ground truth and predicted labels for the first image

The first step for the calculation of surface areas is to acquire volume information, both ground truth labels and predicted labels are required to be binarized. The binary version of the labels is presented in Figure 4.27. Moreover, to evaluate semantic segmentation numerically dice index metric was used which was mentioned in the previous chapter. Figure 4.28 comprises 20 slices of the first test image and as can be seen the similarity ratio between ground truth and predicted labels are considerably high.

Figure 4.29. Area calculation of ground truth labels for the first image (slices from 1 to 81)
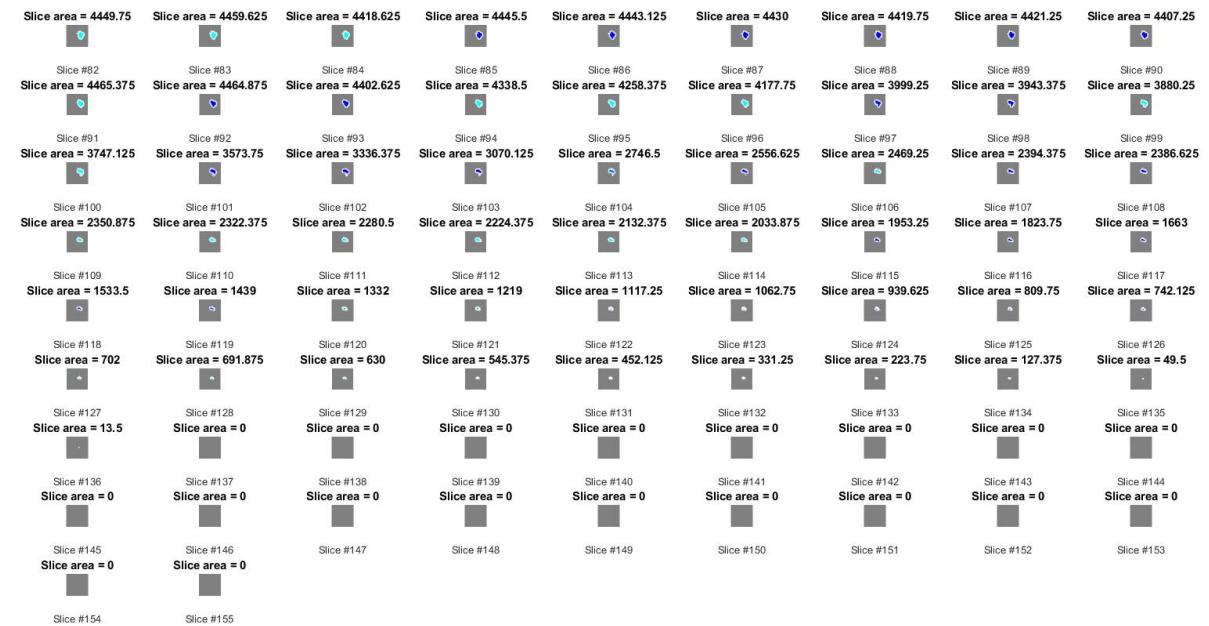
Figure 4.30. Area calculation of ground truth labels for the first image(slices from 82 to155)

Figure 4.29 and Figure 4.30 represent displays of the ground truth surface area calculation for each MR slice on the first test image from 1 to 155. As can be seen in these figures, slice areas without any tumor existence were determined as 0. Other slices with tumors have different results depending on the tumor's size.

Figure 4.31. Area calculation of predicted labels for the first image (slices from 1 to 81)

Figure 4.32. Area calculation of predicted labels for the first image (slices from 82 to 155)

Surface areas of the predicted labels for the first image are shown in Figure 4.32 and Figure 4.33. The outcome of these surface areas is quite accurate with the ground truth labels except for a few slices.

Figure 4.33. Area calculation of the brain for the first image (slices from 1 to 81)
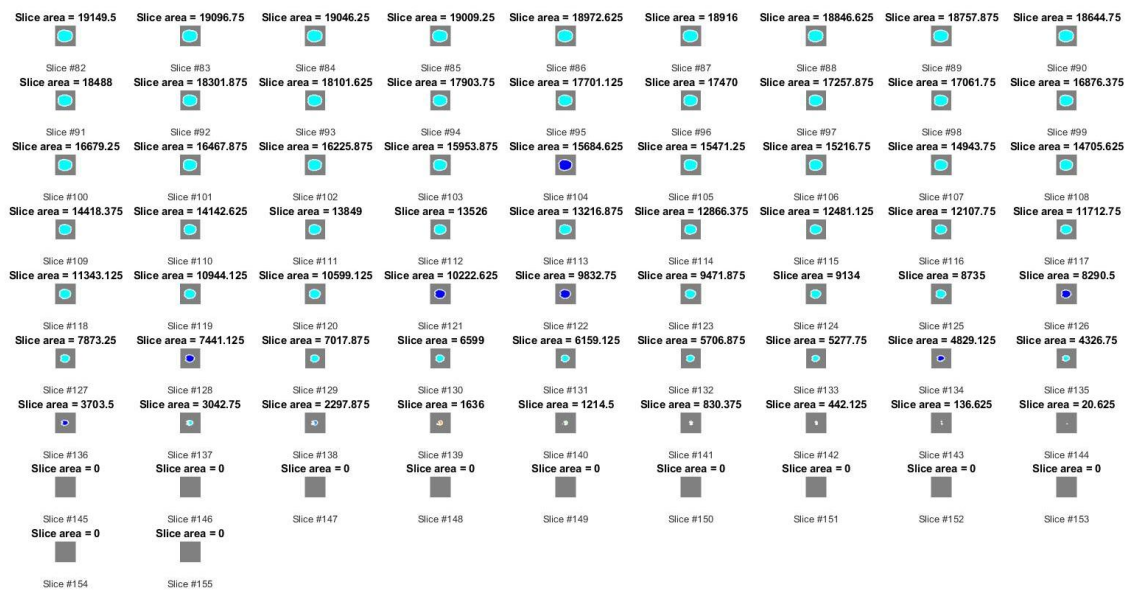
Figure 4.34. Area calculation of the brain for the first image (slices from 82 to 155)

Figure 4.33 and Figure 4.34 are the representation of surface areas for the brain on each MR slice for the first test image. Another important application in this study is to insert labels into segmented MR slices for imaging brain and tumor in 3D. Figure 4.35 shows the insertion process and Figure 4.36 represents 3D imaging for the first test image. Figure 4.37 indicates 3D imaging for the real and predicted tumor.
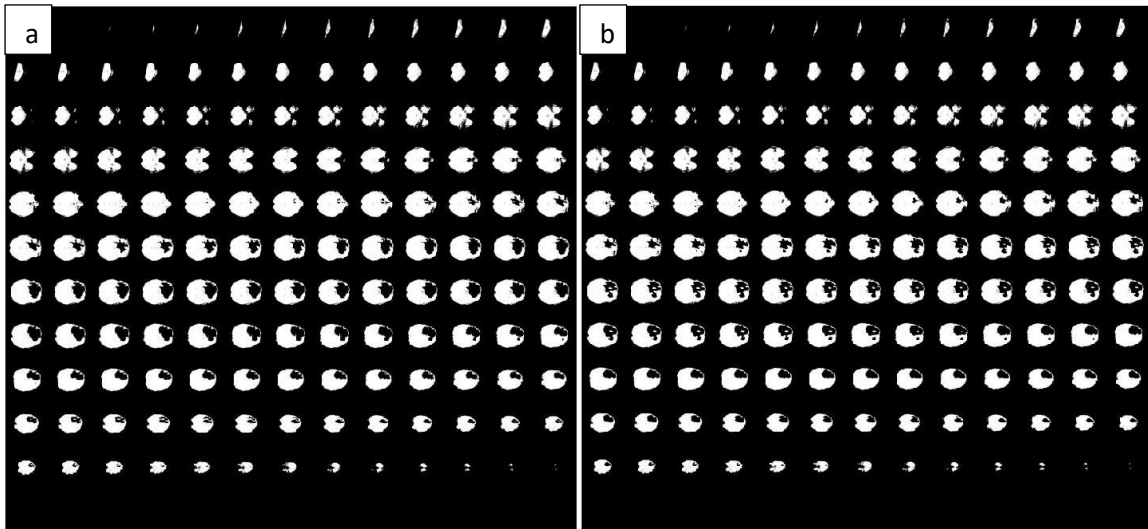
Figure 4.35. Label insertion into the segmented brain images, a) ground truth, b) predicted

Figure 4.36. 3D imaging by using segmented brain and label images for the first image, a) whole brain, b) brain with ground truth and c) brain with predicted labels

Figure 4.37. Brain tumor extraction in 3D for the first image, a) tumor with ground truth labels, b) tumor with predicted labels

Figure 4.38. All imaging modalities for the second image, a) original slices b) histogram equalization applied

Figure 4.39. Segmented slices for the second image
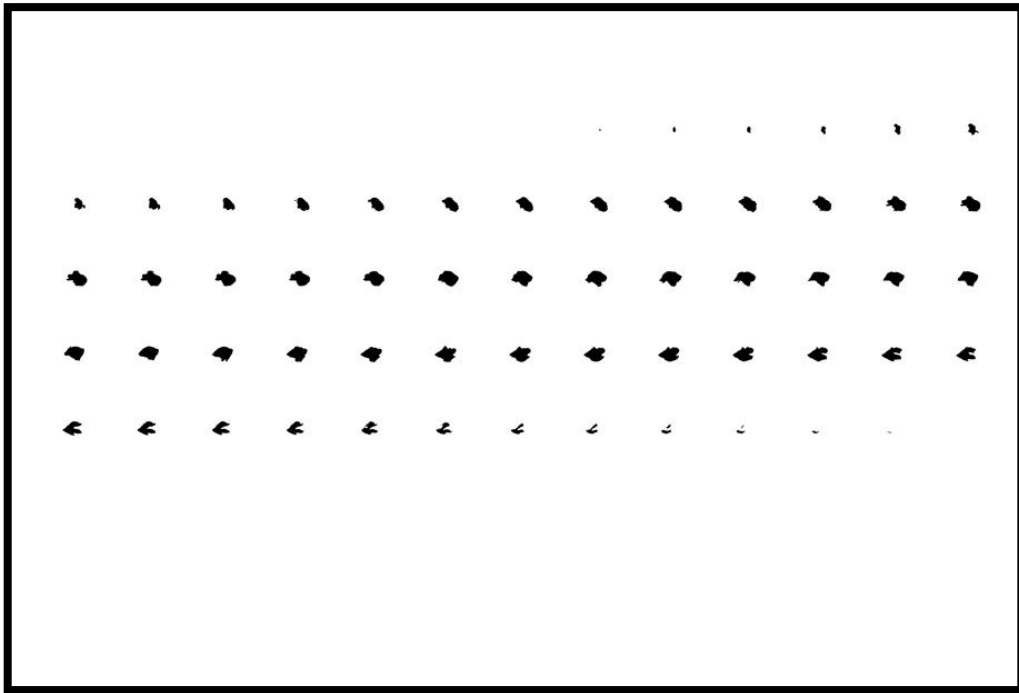
Figure 4.40. Ground truth labels for the second image
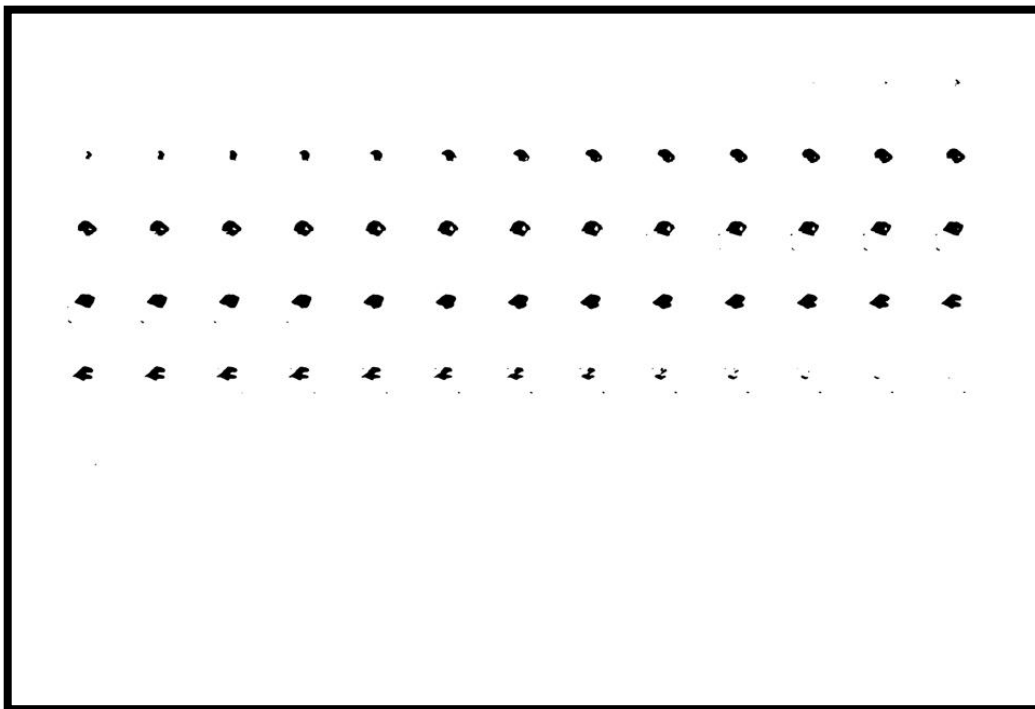
Figure 4.41. Predicted labels for the second image

Original images and their version of histogram equalization for the second test image are shown in Figure 4.38. Then, segmented MR brain slices can be seen in Figure 4.39. Ground truth and predicted labels for the second image can be compared in terms of understanding their similarity as a black and white form in Figure 4.40 and Figure 4.41.
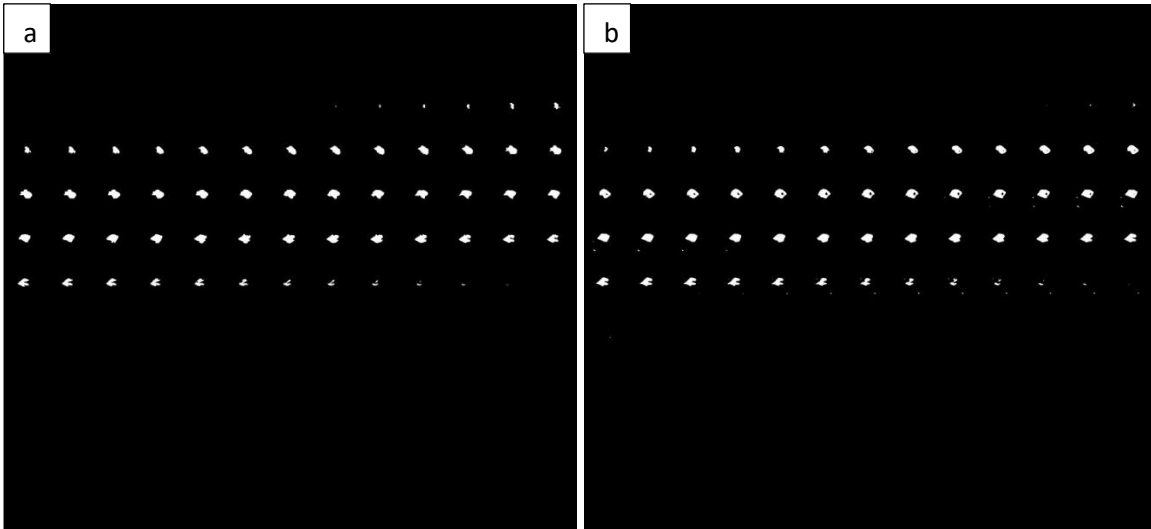
Figure 4.42.Binary versions of ground truth (a) and predicted (b) labels for the second image
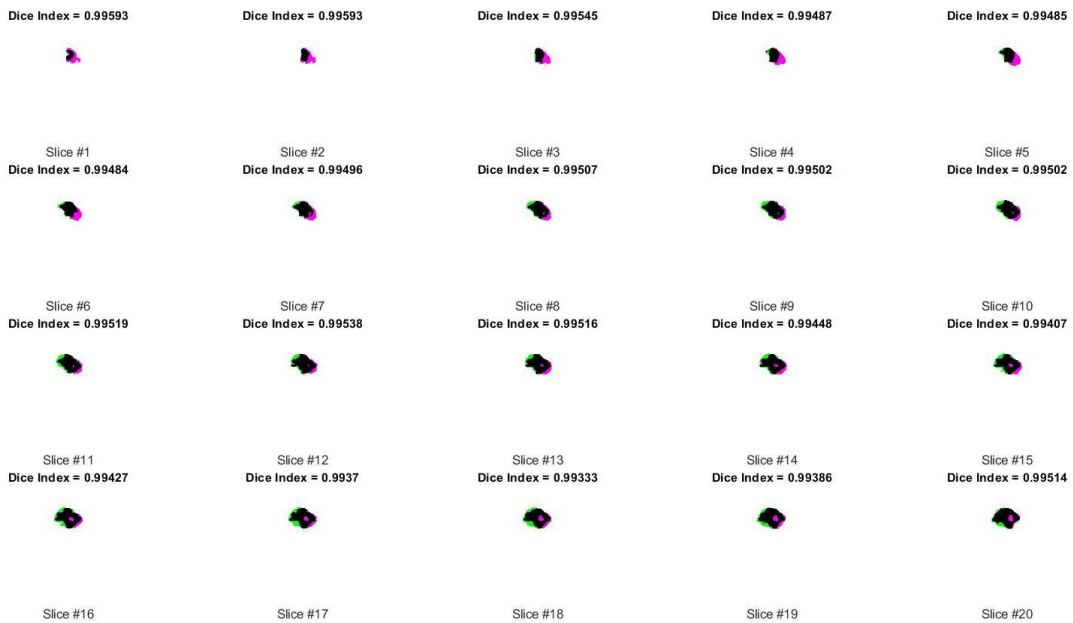
Figure 4.43. Dice scores of ground truth and predicted labels for the second image

Binarized version of ground truth and predicted labels to determine the surface areas of each slice are stated in Figure 4.42. Dice index values for 20 slices on the second test image are shown in Figure 4.43. The resemblance with the labels which can be examined in this figure is significantly accurate.

Figure 4.44 (slices 1 to 81):

Slice area = 0	Slice area = 0	Slice area = 0	Slice area = 0	Slice area = 0	Slice area = 0	Slice area = 0	Slice area = 0	Slice area = 0
Slice #1	Slice #2	Slice #3	Slice #4	Slice #5	Slice #6	Slice #7	Slice #8	Slice #9
Slice area = 0	Slice area = 0	Slice area = 0	Slice area = 0	Slice area = 0	Slice area = 0	Slice area = 0	Slice area = 0	Slice area = 0
Slice #10	Slice #11	Slice #12	Slice #13	Slice #14	Slice #15	Slice #16	Slice #17	Slice #18
Slice area = 0	Slice area = 0	Slice area = 0	Slice area = 0	Slice area = 0	Slice area = 0	Slice area = 0	Slice area = 0	Slice area = 0
Slice #19	Slice #20	Slice #21	Slice #22	Slice #23	Slice #24	Slice #25	Slice #26	Slice #27
Slice area = 0	Slice area = 0	Slice area = 0	Slice area = 0	Slice area = 0	Slice area = 0	Slice area = 23.875	Slice area = 124.25	Slice area = 191
Slice #28	Slice #29	Slice #30	Slice #31	Slice #32	Slice #33	Slice #34	Slice #35	Slice #36
Slice area = 281.75	Slice area = 488.75	Slice area = 670.25	Slice area = 809.25	Slice area = 943.625	Slice area = 1080.75	Slice area = 1225.25	Slice area = 1372.25	Slice area = 1494.5
Slice #37	Slice #38	Slice #39	Slice #40	Slice #41	Slice #42	Slice #43	Slice #44	Slice #45
Slice area = 1594.375	Slice area = 1644.75	Slice area = 1716.5	Slice area = 1762.25	Slice area = 1814.875	Slice area = 1924.375	Slice area = 1983.625	Slice area = 2004.75	Slice area = 2020.25
Slice #46	Slice #47	Slice #48	Slice #49	Slice #50	Slice #51	Slice #52	Slice #53	Slice #54
Slice area = 2037	Slice area = 2048.5	Slice area = 2079.875	Slice area = 2167.375	Slice area = 2143.875	Slice area = 2172.875	Slice area = 2164.125	Slice area = 2025.25	Slice area = 1939.25
Slice #55	Slice #56	Slice #57	Slice #58	Slice #59	Slice #60	Slice #61	Slice #62	Slice #63
Slice area = 1928	Slice area = 1986.375	Slice area = 1931.5	Slice area = 1909.625	Slice area = 1991	Slice area = 2045.125	Slice area = 2023.375	Slice area = 2069.5	Slice area = 2090
Slice #64	Slice #65	Slice #66	Slice #67	Slice #68	Slice #69	Slice #70	Slice #71	Slice #72
Slice area = 2079.25	Slice area = 2096.125	Slice area = 2035.5	Slice area = 1919.25	Slice area = 1802.25	Slice area = 1710.25	Slice area = 1589.375	Slice area = 1484.875	Slice area = 1390.25
Slice #73	Slice #74	Slice #75	Slice #76	Slice #77	Slice #78	Slice #79	Slice #80	Slice #81

Figure 4.44.Area calculation of ground truth labels for the second image(slices from 1 to 81)

Figure 4.45 (slices 82 to 155):

Slice area = 1288.75	Slice area = 1163.25	Slice area = 909.125	Slice area = 635.25	Slice area = 502.125	Slice area = 354.125	Slice area = 203.75	Slice area = 102.875	Slice area = 25.125
Slice #82	Slice #83	Slice #84	Slice #85	Slice #86	Slice #87	Slice #88	Slice #89	Slice #90
Slice area = 0	Slice area = 0	Slice area = 0	Slice area = 0	Slice area = 0	Slice area = 0	Slice area = 0	Slice area = 0	Slice area = 0
Slice #91	Slice #92	Slice #93	Slice #94	Slice #95	Slice #96	Slice #97	Slice #98	Slice #99
Slice area = 0	Slice area = 0	Slice area = 0	Slice area = 0	Slice area = 0	Slice area = 0	Slice area = 0	Slice area = 0	Slice area = 0
Slice #100	Slice #101	Slice #102	Slice #103	Slice #104	Slice #105	Slice #106	Slice #107	Slice #108
Slice area = 0	Slice area = 0	Slice area = 0	Slice area = 0	Slice area = 0	Slice area = 0	Slice area = 0	Slice area = 0	Slice area = 0
Slice #109	Slice #110	Slice #111	Slice #112	Slice #113	Slice #114	Slice #115	Slice #116	Slice #117
Slice area = 0	Slice area = 0	Slice area = 0	Slice area = 0	Slice area = 0	Slice area = 0	Slice area = 0	Slice area = 0	Slice area = 0
Slice #118	Slice #119	Slice #120	Slice #121	Slice #122	Slice #123	Slice #124	Slice #125	Slice #126
Slice area = 0	Slice area = 0	Slice area = 0	Slice area = 0	Slice area = 0	Slice area = 0	Slice area = 0	Slice area = 0	Slice area = 0
Slice #127	Slice #128	Slice #129	Slice #130	Slice #131	Slice #132	Slice #133	Slice #134	Slice #135
Slice area = 0	Slice area = 0	Slice area = 0	Slice area = 0	Slice area = 0	Slice area = 0	Slice area = 0	Slice area = 0	Slice area = 0
Slice #136	Slice #137	Slice #138	Slice #139	Slice #140	Slice #141	Slice #142	Slice #143	Slice #144
Slice area = 0	Slice area = 0	Slice area = 0	Slice area = 0	Slice area = 0	Slice area = 0	Slice area = 0	Slice area = 0	Slice area = 0
Slice #145	Slice #146	Slice #147	Slice #148	Slice #149	Slice #150	Slice #151	Slice #152	Slice #153
Slice area = 0	Slice area = 0							
Slice #154	Slice #155							

Figure 4.45. Area calculation of ground truth labels for the second image (slices from 82 to 155)

In Figure 4.44 and Figure 4.45, the surface areas of peach slices for the second test image are examined. According to these figures, the original tumor existence starts from slice # 34 to slice #90. Apart from these slices, there isn't any tumor information in the original MR image.

Figure 4.46 content:

Slice area = 0 | Slice #1
Slice area = 0 | Slice #2
Slice area = 0 | Slice #3
Slice area = 0 | Slice #4
Slice area = 0 | Slice #5
Slice area = 0 | Slice #6
Slice area = 0 | Slice #7
Slice area = 0 | Slice #8
Slice area = 0 | Slice #9
Slice area = 0 | Slice #10
Slice area = 0 | Slice #11
Slice area = 0 | Slice #12
Slice area = 0 | Slice #13
Slice area = 0 | Slice #14
Slice area = 0 | Slice #15
Slice area = 0 | Slice #16
Slice area = 0 | Slice #17
Slice area = 0 | Slice #18
Slice area = 0 | Slice #19
Slice area = 0 | Slice #20
Slice area = 0 | Slice #21
Slice area = 0 | Slice #22
Slice area = 0 | Slice #23
Slice area = 0 | Slice #24
Slice area = 0 | Slice #25
Slice area = 0 | Slice #26
Slice area = 0 | Slice #27
Slice area = 0 | Slice #28
Slice area = 0 | Slice #29
Slice area = 0 | Slice #30
Slice area = 0 | Slice #31
Slice area = 0 | Slice #32
Slice area = 0 | Slice #33
Slice area = 0 | Slice #34
Slice area = 0 | Slice #35
Slice area = 0 | Slice #36
Slice area = 5.125 | Slice #37
Slice area = 44.75 | Slice #38
Slice area = 154 | Slice #39
Slice area = 342.75 | Slice #40
Slice area = 503 | Slice #41
Slice area = 646.625 | Slice #42
Slice area = 825.625 | Slice #43
Slice area = 972.25 | Slice #44
Slice area = 1151 | Slice #45
Slice area = 1343.375 | Slice #46
Slice area = 1540.75 | Slice #47
Slice area = 1661.875 | Slice #48
Slice area = 1759.75 | Slice #49
Slice area = 1847.25 | Slice #50
Slice area = 1932.375 | Slice #51
Slice area = 1989.5 | Slice #52
Slice area = 2032.75 | Slice #53
Slice area = 2094.625 | Slice #54
Slice area = 2155.75 | Slice #55
Slice area = 2201.875 | Slice #56
Slice area = 2208.5 | Slice #57
Slice area = 2222.625 | Slice #58
Slice area = 2224.625 | Slice #59
Slice area = 2220.125 | Slice #60
Slice area = 2217.75 | Slice #61
Slice area = 2203.125 | Slice #62
Slice area = 2214.125 | Slice #63
Slice area = 2217.375 | Slice #64
Slice area = 2222.125 | Slice #65
Slice area = 2189.5 | Slice #66
Slice area = 2148.625 | Slice #67
Slice area = 2125.875 | Slice #68
Slice area = 2118 | Slice #69
Slice area = 2131.5 | Slice #70
Slice area = 2151 | Slice #71
Slice area = 2171.5 | Slice #72
Slice area = 2178.75 | Slice #73
Slice area = 2173 | Slice #74
Slice area = 2159.375 | Slice #75
Slice area = 2132.625 | Slice #76
Slice area = 2091 | Slice #77
Slice area = 1995 | Slice #78
Slice area = 1923.125 | Slice #79
Slice area = 1833.375 | Slice #80
Slice area = 1769.625 | Slice #81

Figure 4.46. Area calculation of predicted labels for the second image (slices from 1 to 81)

Figure 4.47 content:

Slice area = 1682.125 | Slice #82
Slice area = 1562.375 | Slice #83
Slice area = 1408.875 | Slice #84
Slice area = 1204.875 | Slice #85
Slice area = 971.875 | Slice #86
Slice area = 711.875 | Slice #87
Slice area = 427.625 | Slice #88
Slice area = 237.625 | Slice #89
Slice area = 126.375 | Slice #90
Slice area = 35 | Slice #91
Slice area = 14.5 | Slice #92
Slice area = 0 | Slice #93
Slice area = 0 | Slice #94
Slice area = 0 | Slice #95
Slice area = 0 | Slice #96
Slice area = 0 | Slice #97
Slice area = 0 | Slice #98
Slice area = 0 | Slice #99
Slice area = 0 | Slice #100
Slice area = 0 | Slice #101
Slice area = 0 | Slice #102
Slice area = 0 | Slice #103
Slice area = 0 | Slice #104
Slice area = 0 | Slice #105
Slice area = 0 | Slice #106
Slice area = 0 | Slice #107
Slice area = 0 | Slice #108
Slice area = 0 | Slice #109
Slice area = 0 | Slice #110
Slice area = 0 | Slice #111
Slice area = 0 | Slice #112
Slice area = 0 | Slice #113
Slice area = 0 | Slice #114
Slice area = 0 | Slice #115
Slice area = 0 | Slice #116
Slice area = 0 | Slice #117
Slice area = 0 | Slice #118
Slice area = 0 | Slice #119
Slice area = 0 | Slice #120
Slice area = 0 | Slice #121
Slice area = 0 | Slice #122
Slice area = 0 | Slice #123
Slice area = 0 | Slice #124
Slice area = 0 | Slice #125
Slice area = 0 | Slice #126
Slice area = 0 | Slice #127
Slice area = 0 | Slice #128
Slice area = 0 | Slice #129
Slice area = 0 | Slice #130
Slice area = 0 | Slice #131
Slice area = 0 | Slice #132
Slice area = 0 | Slice #133
Slice area = 0 | Slice #134
Slice area = 0 | Slice #135
Slice area = 0 | Slice #136
Slice area = 0 | Slice #137
Slice area = 0 | Slice #138
Slice area = 0 | Slice #139
Slice area = 0 | Slice #140
Slice area = 0 | Slice #141
Slice area = 0 | Slice #142
Slice area = 0 | Slice #143
Slice area = 0 | Slice #144
Slice area = 0 | Slice #145
Slice area = 0 | Slice #146
Slice #147
Slice #148
Slice #149
Slice #150
Slice #151
Slice #152
Slice #153
Slice area = 0 | Slice #154
Slice area = 0 | Slice #155

Figure 4.47. Area calculation of predicted labels for the second image (slices from 82 to 155)

Figure 4.46 and Figure 4.47 indicate the surface areas for the predicted labels on the second test image. Comparing to ground truth versions of the image, tumor existence can be analyzed between slices # 37 and #92 which can be interpreted as a significant match with ground truth.

Figure 4.48. Area calculation of the brain for the second image (slices from 1 to 81)

Figure 4.49. Area calculation of the brain for the second image (slices from 82 to 155)

Surface areas of the brain for the second test image are displayed in Figure 4.48 and Figure 4.49. For 3D imaging of the second test image which consists of 155 slices is presented in Figure 4.51. According to this figure, it can be said that even if the location of the tumor change, our suggested method is quite effective to find the tumor accurately and display it in 3D.

Figure 4.50. Label insertion into the segmented brain images for the second image,
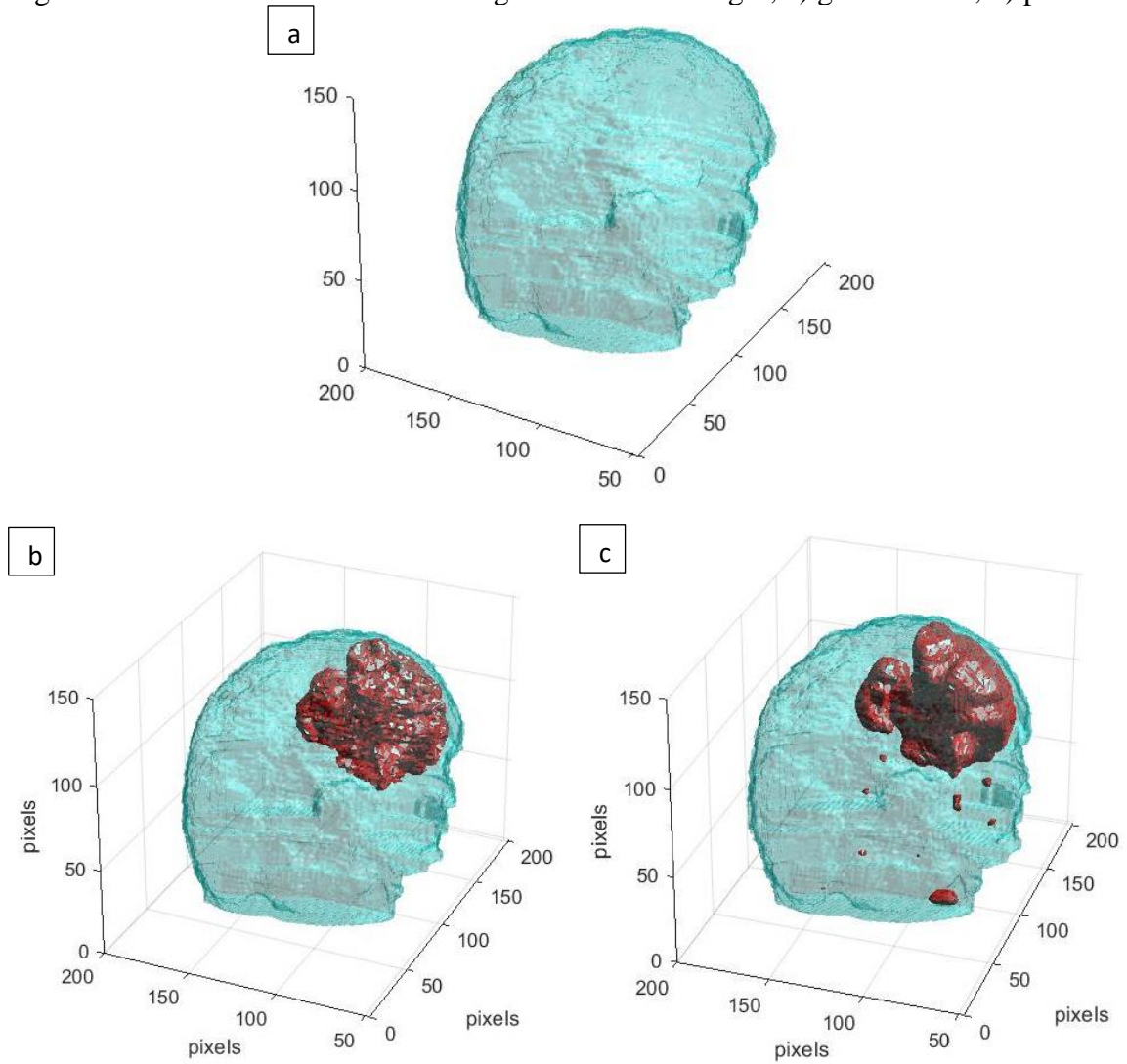a) ground truth, b) predicted

Figure 4.51. 3D imaging by using segmented brain and label images for the second image,
a) whole brain, b) brain with ground truth and c) brain with predicted labels
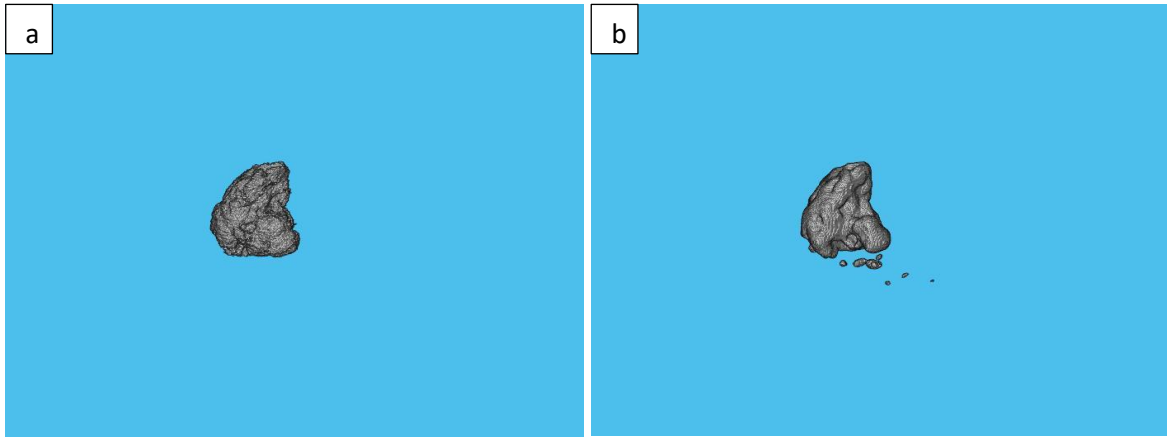
Figure 4.52. Brain tumor extraction in 3D for the second image, a) tumor with ground truth labels, b) tumor with predicted labels
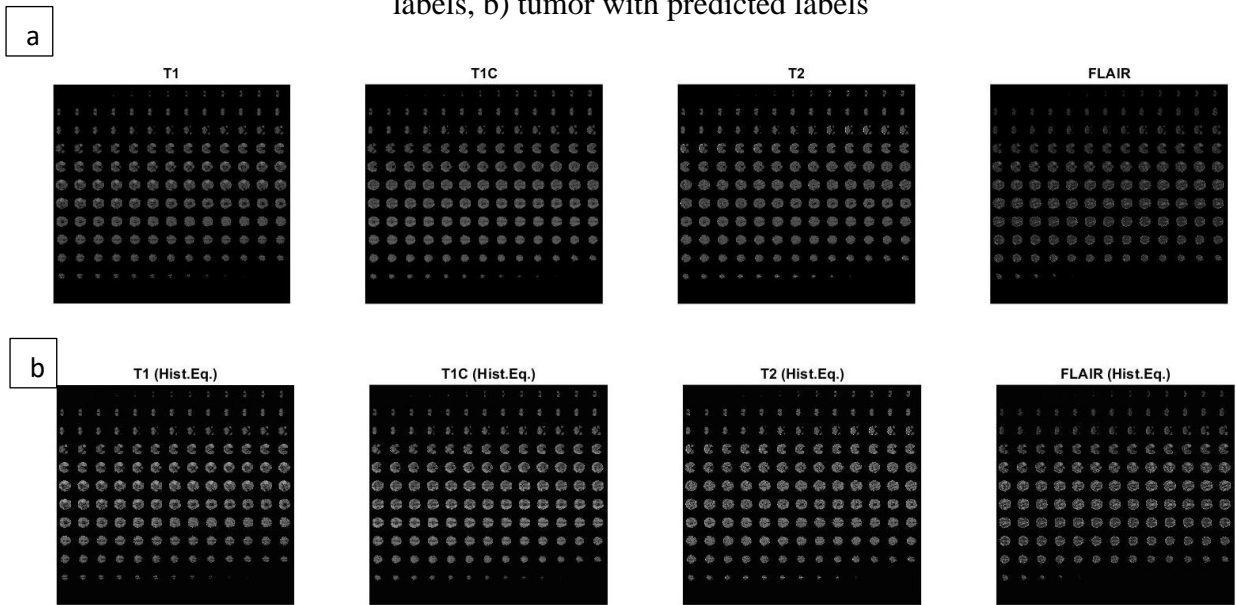

Figure 4.53. All imaging modalities for the third image, a) original slices b) histogram equalization applied
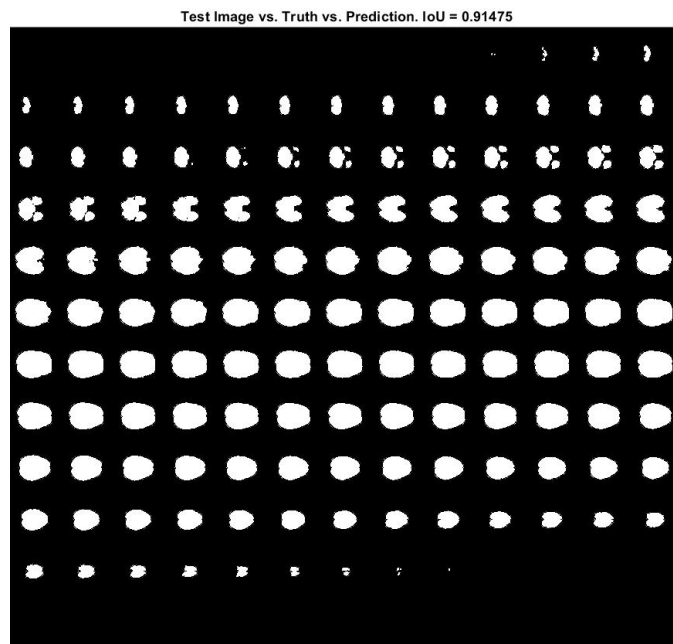
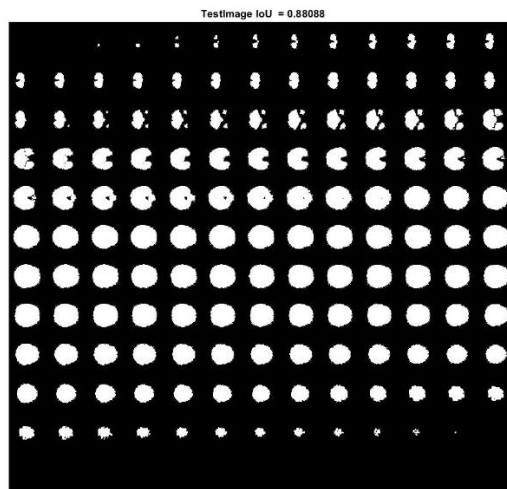Figure 4.54. Segmented slices for the third image
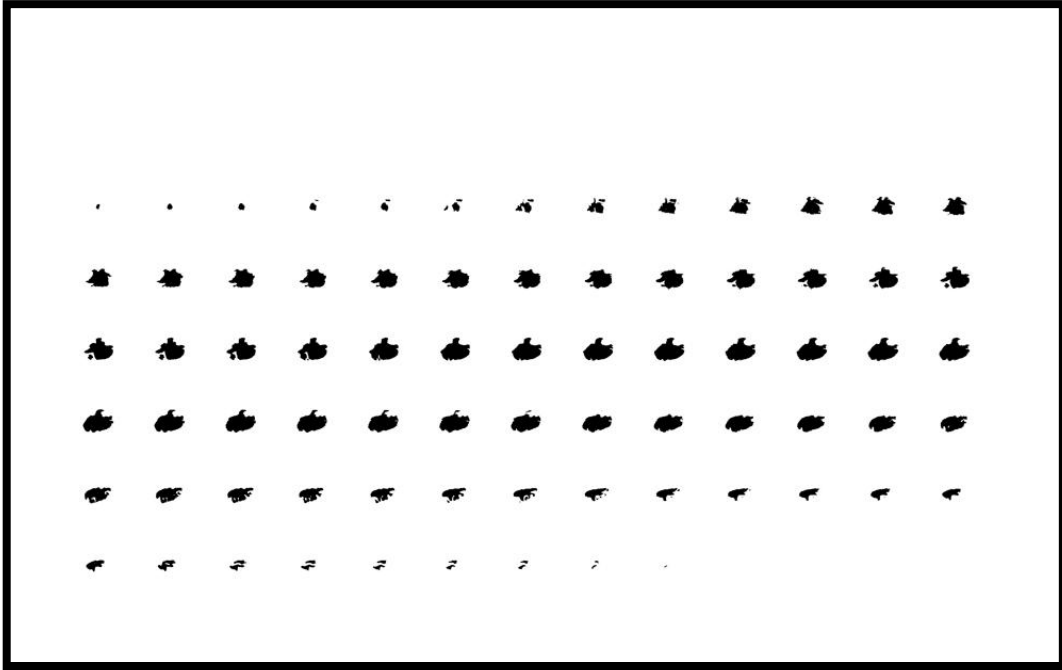
Figure 4.55. Ground truth labels for the third image

Figure 4.56. Predicted labels for the third image

Original and pre-processed slices for the third test image are presented in Figure 4.54. Segmented MR slices for the same image can be observed in Figure 4.55. In addition, ground truth and predicted labels are shown in Figure 4.55 and Figure 4.56.
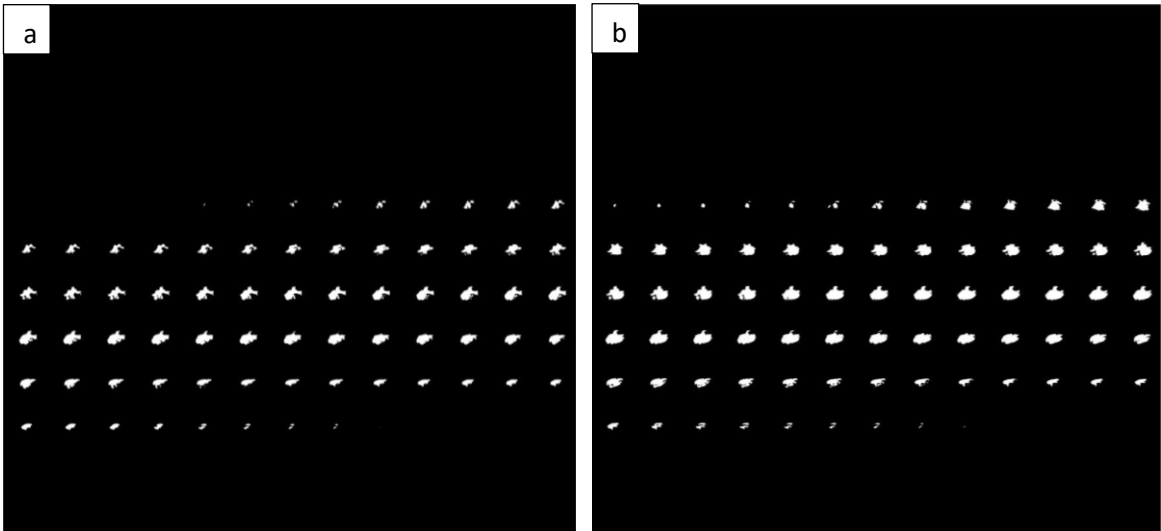
Figure 4.57. Binary versions of ground truth (a) and predicted (b) labels for the third image
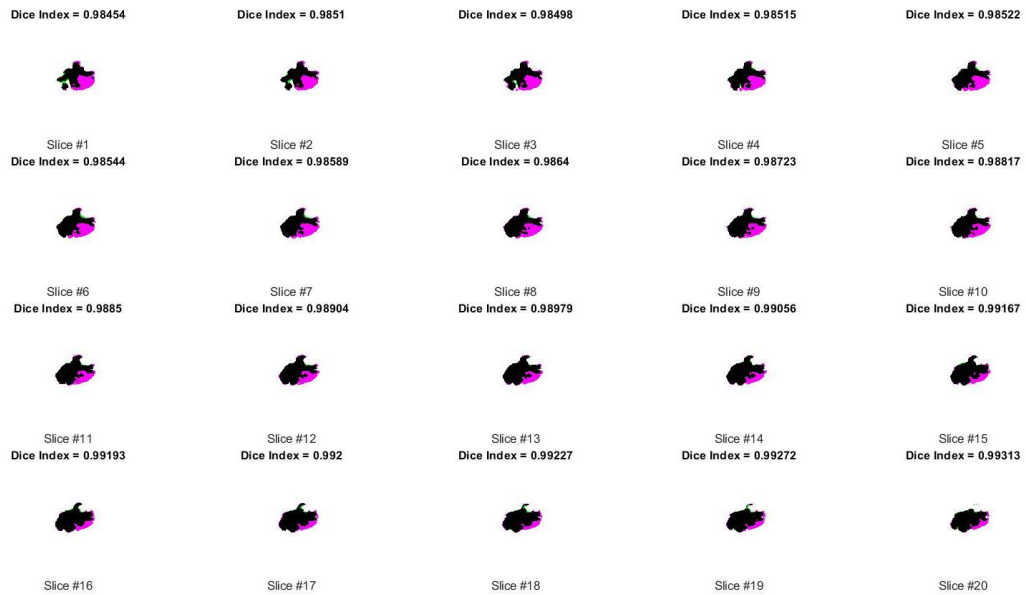
Figure 4.58. Dice scores of ground truth and predicted labels for the third image

Binarized slices are required to calculate surface areas for ground truth and predicted labels. These binary images for the third test image are displayed in Figure 4.57. Dice score of 20 slices for the third image which is crucial to emphasize the success of semantic segmentation is shown in Figure 4.58.

Figure 4.59. Area calculation of ground truth labels for the third image (slices from 1 to 81)
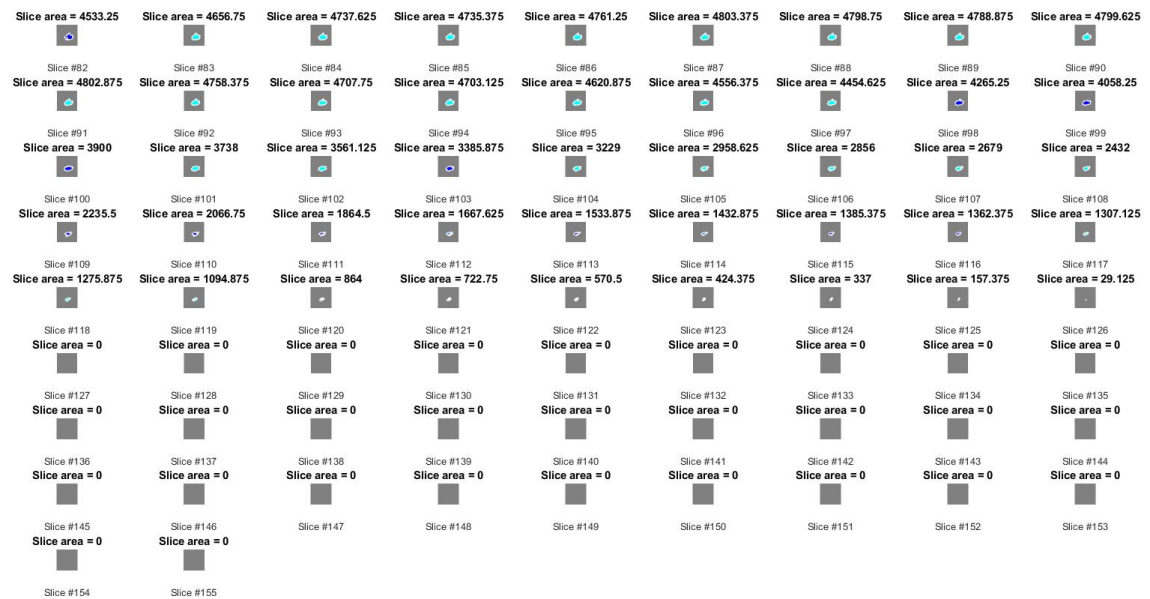
Figure 4.60.Area calculation of ground truth labels for the third image(slices from 82 to 155)

For the third test image, tumor existence of ground truth labels can be observed between slices #53 and #126. The surface area values of these slices can also be shown in Figure 4.59 and Figure 4.60).

Figure 4.61. Area calculation of predicted labels for the third image (slices from 1 to 81)

Figure 4.62. Area calculation of predicted labels for the third image (slices from 82 to 155)

Prediction for tumor existence on the third test image is quite accurate. In Figure 4.61 and Figure 4.62, the formation of the tumor can be examined from slice # 57 to slice # 126 which is almost the same as the original data.

Figure 4.63. Area calculation of the brain for the third image (slices from 1 to 81)

Slice	Area	Slice	Area	Slice	Area
#1	0	#2	0	#3	0
#4	0	#5	0	#6	0
#7	0	#8	0	#9	0
#10	18.25	#11	362.5	#12	835.125
#13	1315.875	#14	1787.75	#15	2165.125
#16	2423.625	#17	2678.5	#18	2885.25
#19	3095.375	#20	3270.75	#21	3437.375
#22	3610.875	#23	3747.875	#24	3883.125
#25	4019.75	#26	4151.5	#27	4271.375
#28	4379.125	#29	4499.875	#30	4634
#31	4921	#32	5545.25	#33	5893.625
#34	6189.75	#35	6464	#36	6719.875
#37	7070.75	#38	7382.625	#39	7708.75
#40	8164.375	#41	8616.25	#42	9083.875
#43	9608.75	#44	10069	#45	10395
#46	10697.25	#47	11005.25	#48	11316.25
#49	11538.875	#50	11763.125	#51	12007.125
#52	12256.875	#53	12521.25	#54	12957.875
#55	13409.5	#56	13762.375	#57	14017.875
#58	14282.375	#59	14463.125	#60	14689
#61	14815.125	#62	15095.125	#63	15263.875
#64	15431.5	#65	15581.625	#66	15689.5
#67	15972.375	#68	16149.875	#69	16313.25
#70	16430	#71	16511.625	#72	16560.25
#73	16595.875	#74	16584.25	#75	16593.75
#76	16609.875	#77	16592.5	#78	16607.375
#79	16574.75	#80	16553.625	#81	16514.25

Figuer 4.64. Area calculation of the brain for the third image (slices from 82 to 155)

Slice	Area	Slice	Area	Slice	Area
#82	16468	#83	16419.25	#84	16375.5
#85	16300.25	#86	16197.5	#87	16112.75
#88	16025.125	#89	15930.25	#90	15812
#91	15690.5	#92	15563.5	#93	15417.375
#94	15255.5	#95	15097.375	#96	14911.875
#97	14745.25	#98	14560.5	#99	14364.375
#100	14153.5	#101	13959.125	#102	13724.875
#103	13469.25	#104	13239.5	#105	12954.875
#106	12687.625	#107	12433.625	#108	12157.25
#109	11871.125	#110	11588.5	#111	11281.375
#112	10982.125	#113	10700	#114	10371.5
#115	10055	#116	9741.375	#117	9413.375
#118	9103.75	#119	8775.75	#120	8432.875
#121	8067.125	#122	7733.375	#123	7330.125
#124	6923.875	#125	6517	#126	6078.25
#127	5581	#128	5134.75	#129	4698.25
#130	4244.875	#131	3786.875	#132	3362.625
#133	2866	#134	2349.375	#135	1745.125
#136	1070.5	#137	634.625	#138	162.375
#139	18.375	#140	0	#141	0
#142	0	#143	0	#144	0
#145	0	#146	0	#147	0
#148	0	#149	0	#150	0
#151	0	#152	0	#153	0
#154	0	#155	0		

In order to determine brain volume for the third test image, the area of all slices was calculated and shown in Figure 4.63 and Figure 4.64. Regardless of the tumor region, our method works quite efficiently for 3D imaging of the third test image which is shown in Figure 4.65.
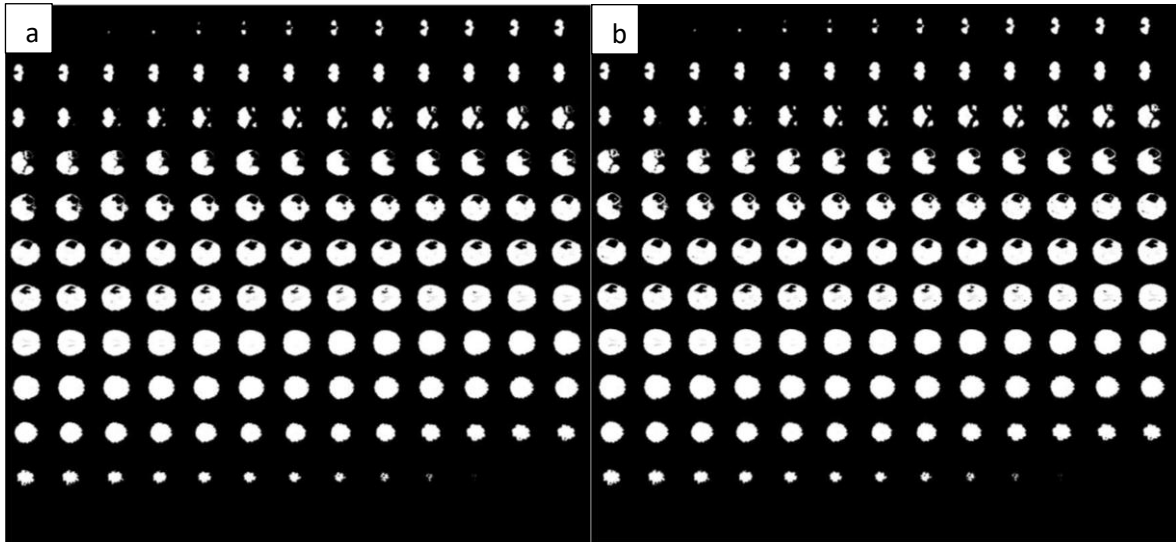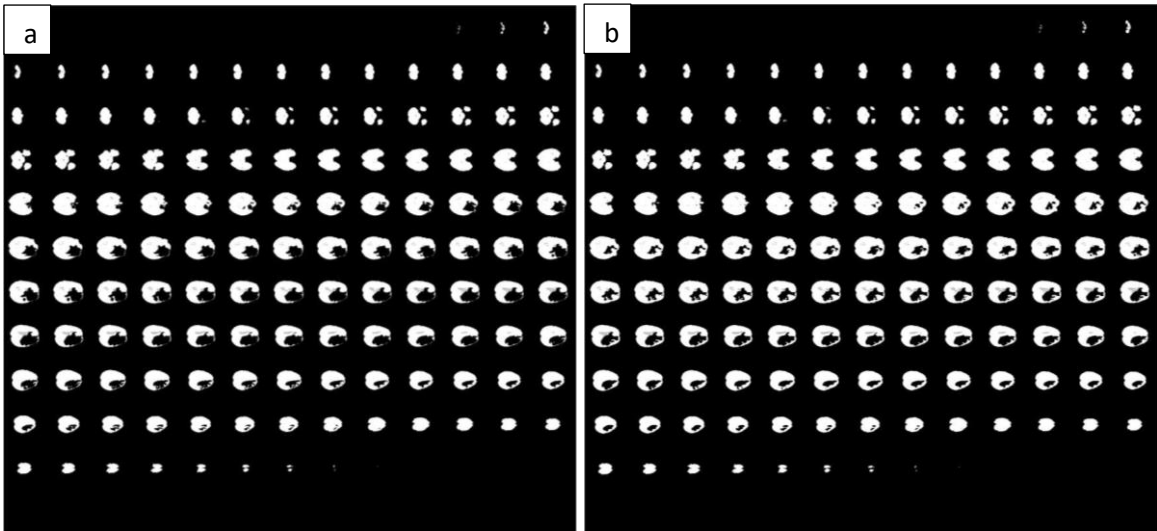
Figure 4.65. Label insertion into the segmented brain images for the third image,
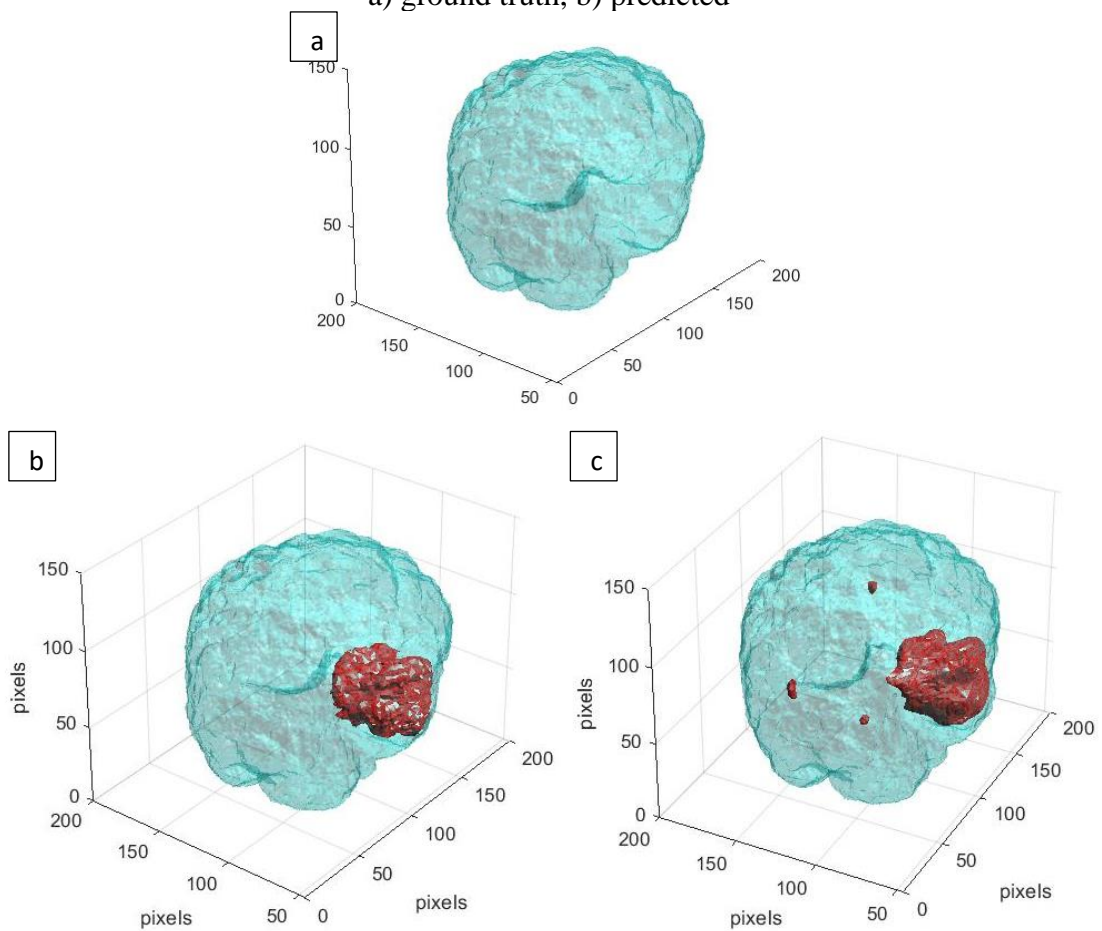a) ground truth, b) predicted
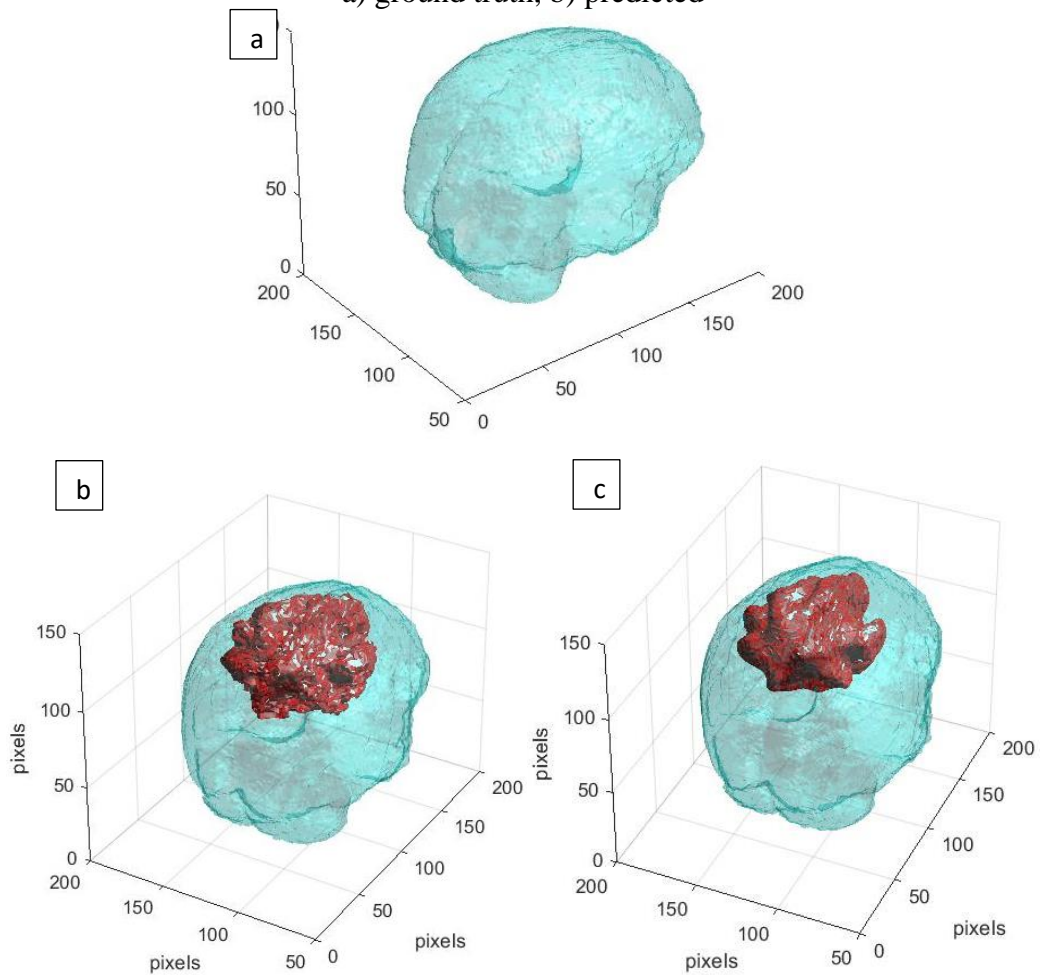
Figure 4.66. 3D imaging by using segmented brain and label images for the third image,
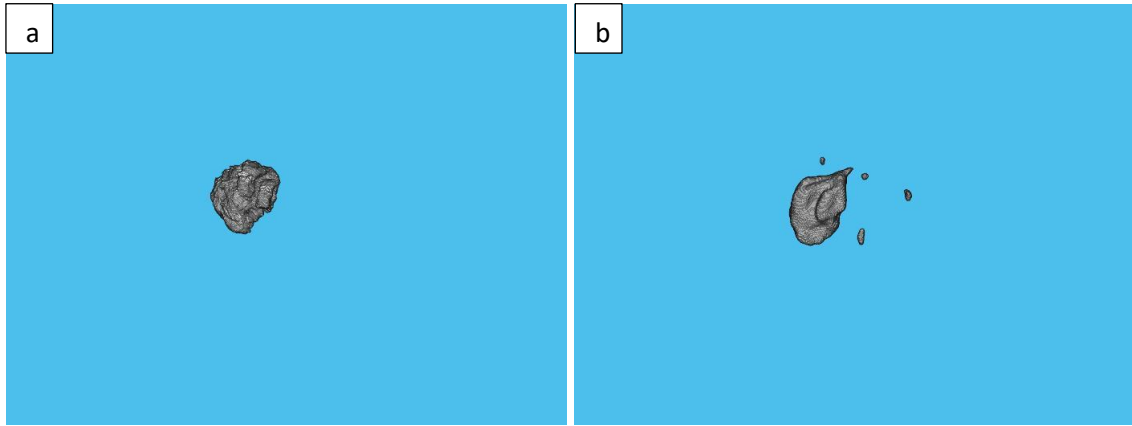a) whole brain, b) brain with ground truth and c) brain with predicted labels
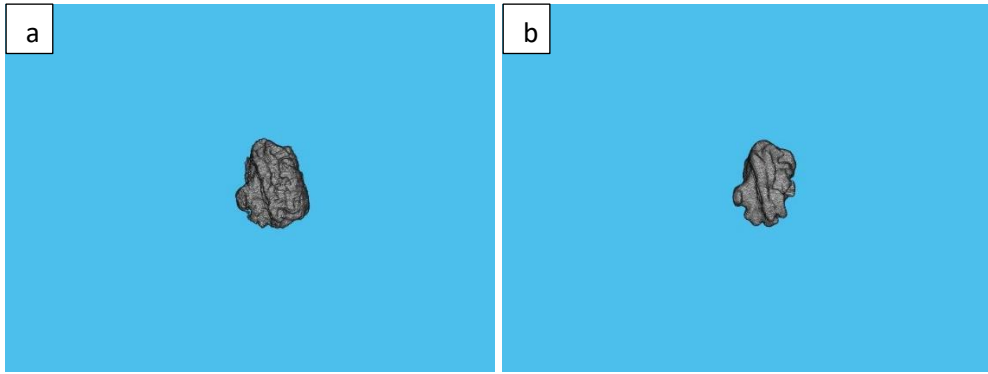
Figure 4.67. Brain tumor extraction in 3D for the third image, a) tumor with ground truth labels, b) tumor with predicted labels
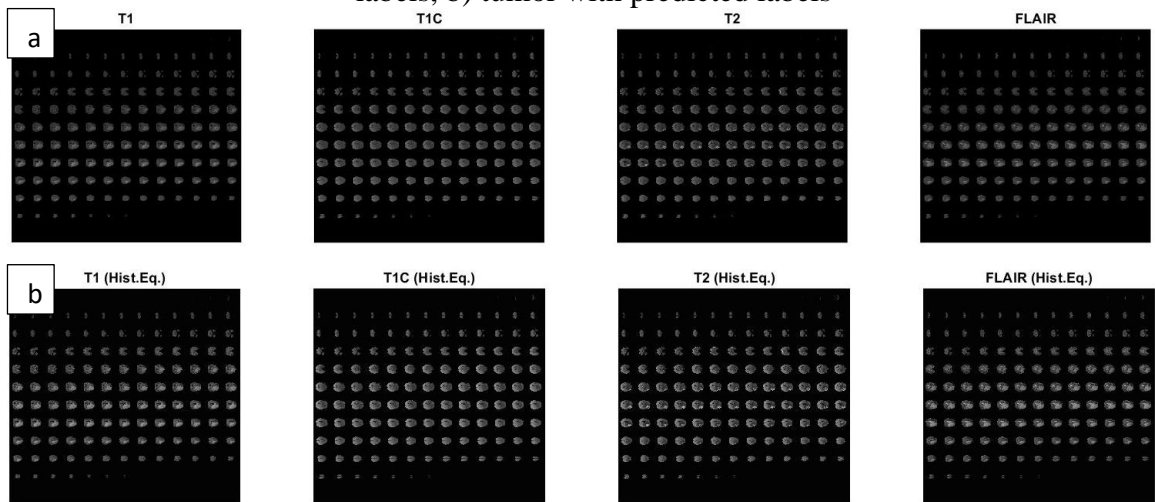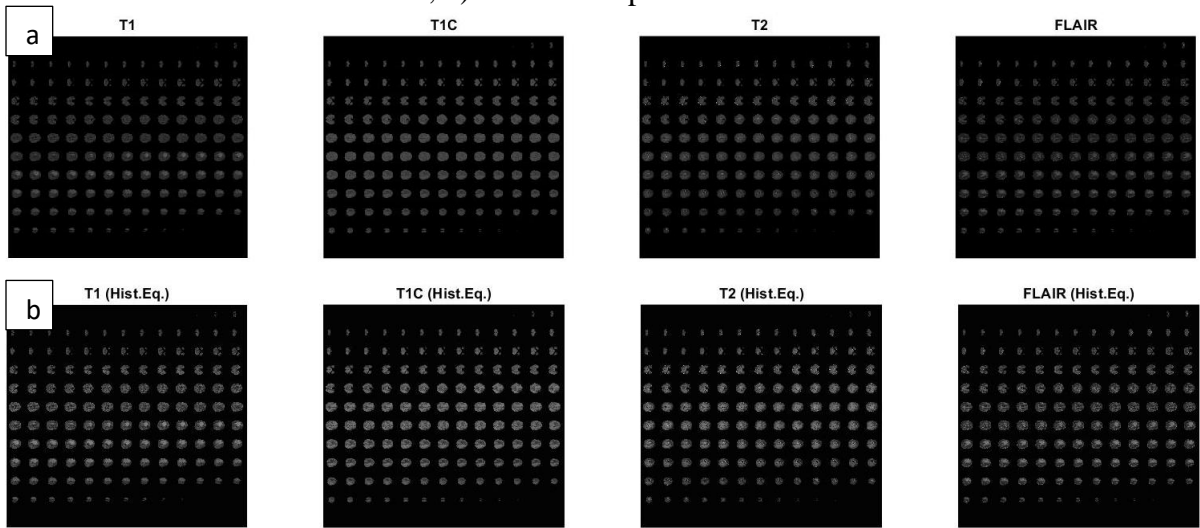

Figure 4.68. All imaging modalities for the fourth image, a) original slices b) histogram equalization applied
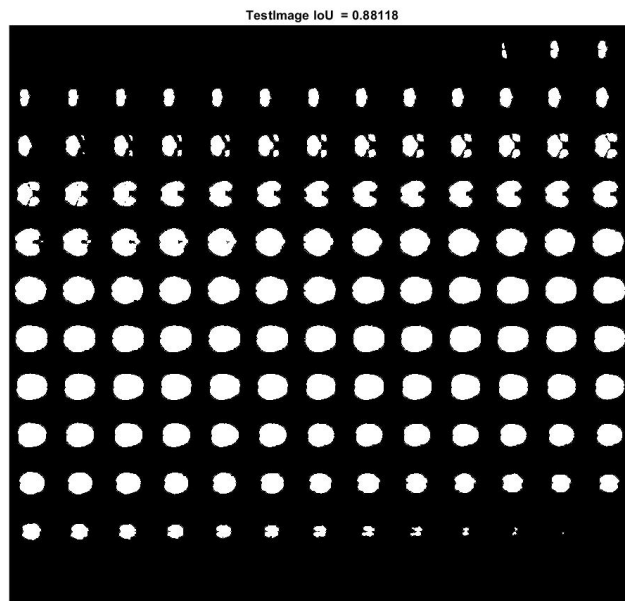
Figure 4.69. Segmented slices for the fourth image

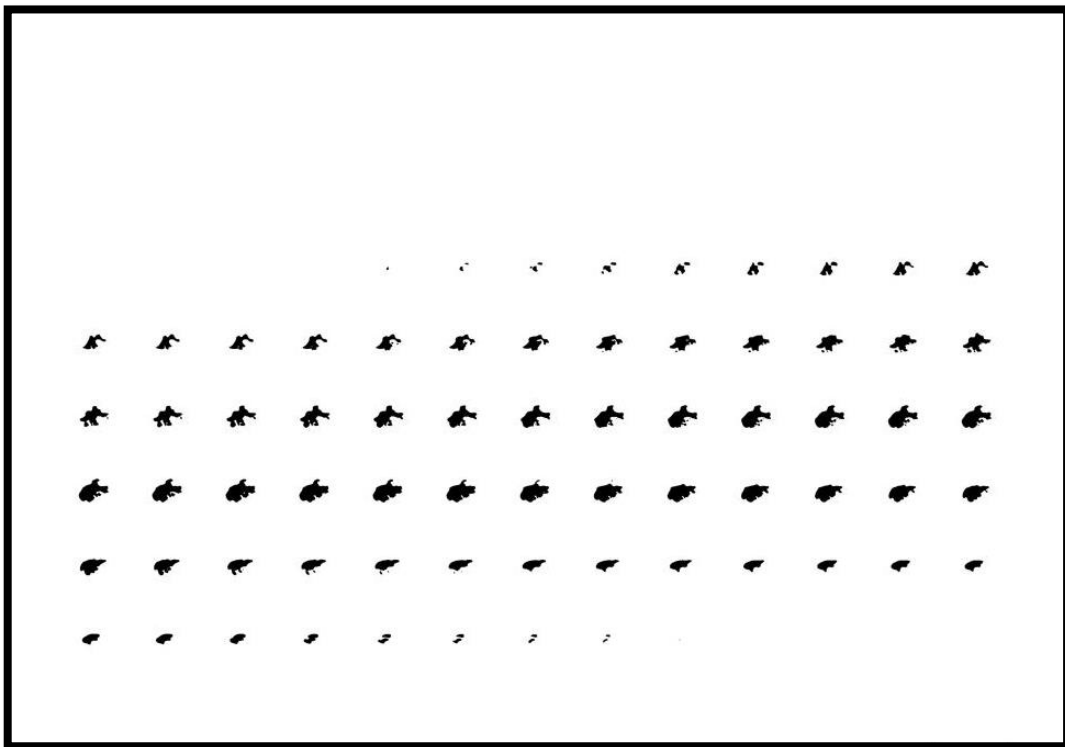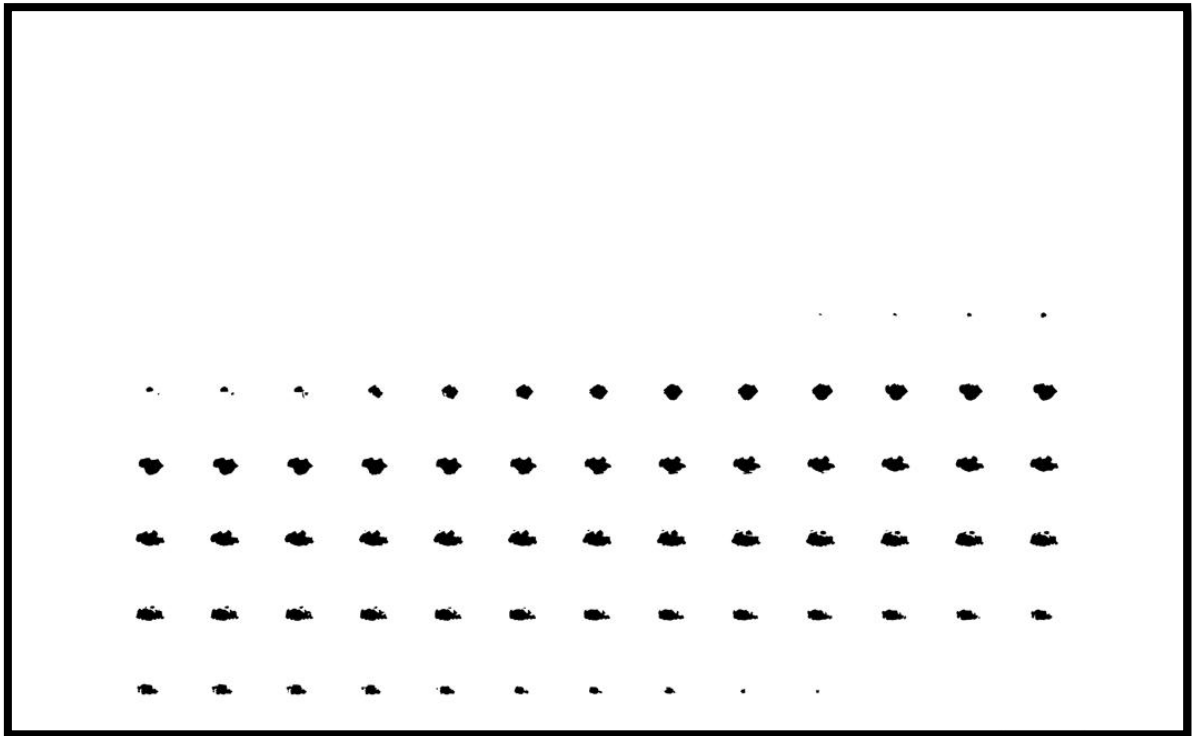Figure 4.70. Ground truth labels for the fourth image
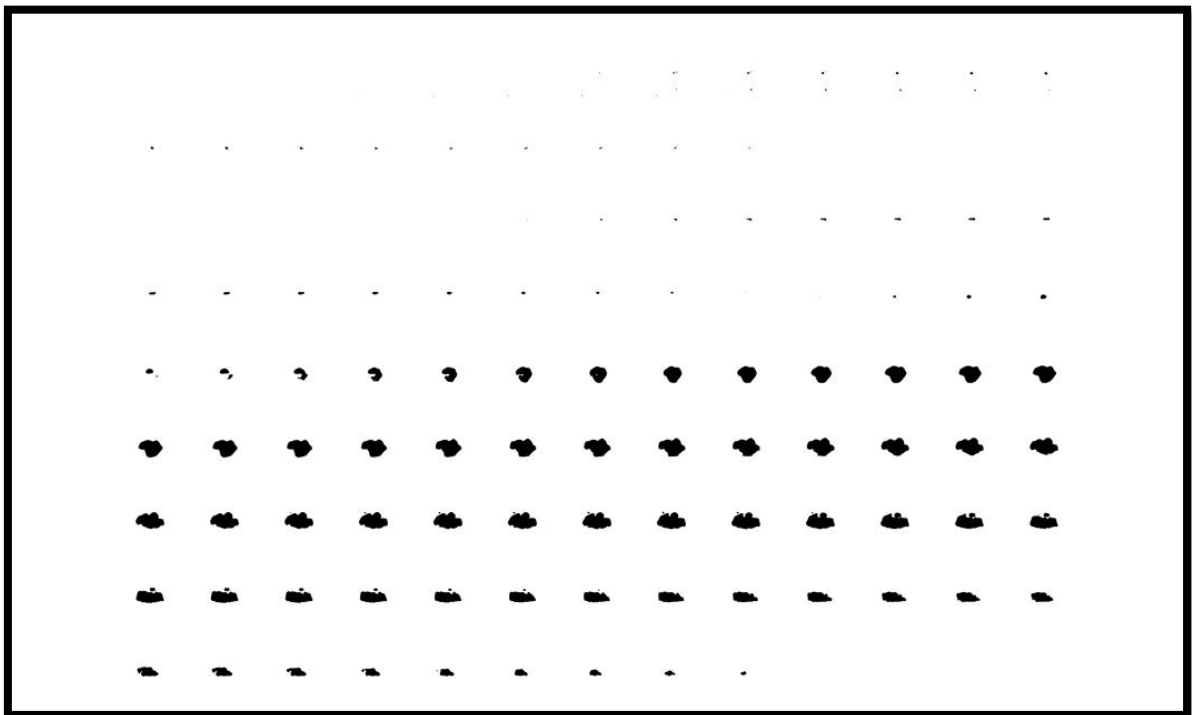
Figure 4.71. Predicted labels for the fourth image
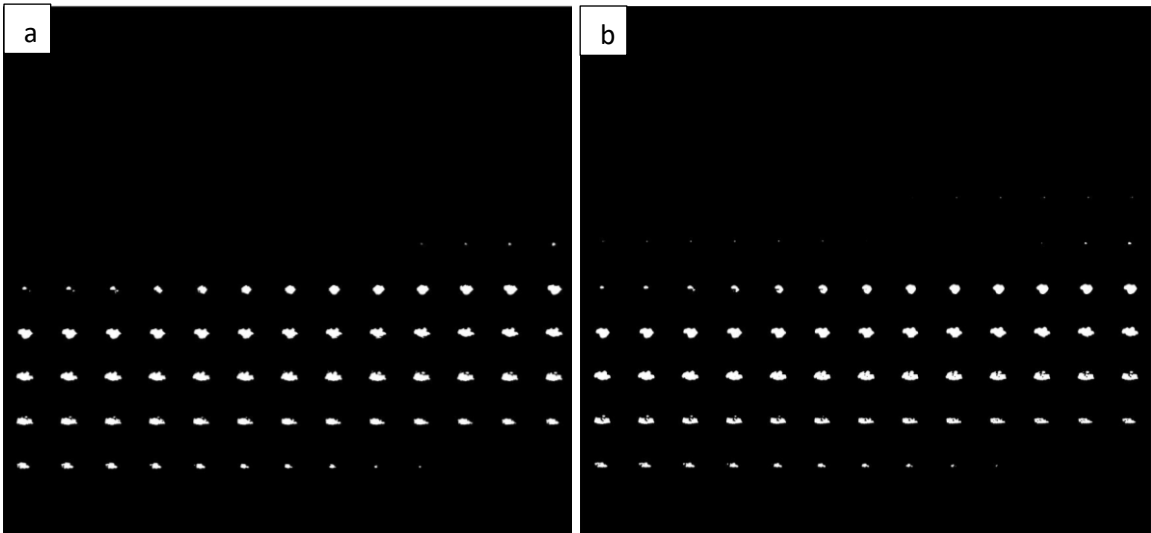
Figure 4.72. Binary versions of ground truth (a) and predicted (b) labels for the fourth image

Dice Index = 0.99884	Dice Index = 0.9978	Dice Index = 0.99709	Dice Index = 0.99611	Dice Index = 0.99618
Slice #1	Slice #2	Slice #3	Slice #4	Slice #5
Dice Index = 0.99705	Dice Index = 0.99817	Dice Index = 0.99727	Dice Index = 0.99733	Dice Index = 0.99703
Slice #6	Slice #7	Slice #8	Slice #9	Slice #10
Dice Index = 0.99734	Dice Index = 0.99762	Dice Index = 0.99781	Dice Index = 0.99819	Dice Index = 0.9985
Slice #11	Slice #12	Slice #13	Slice #14	Slice #15
Dice Index = 0.9982	Dice Index = 0.99802	Dice Index = 0.99753	Dice Index = 0.99732	Dice Index = 0.9971
Slice #16	Slice #17	Slice #18	Slice #19	Slice #20

Figure 4.73. Dice scores of ground truth and predicted labels for the fourth image

Figure (slices 1 to 81): Each slice from #1 through #74 has "Slice area = 0".

Slice	Area
#1–#74	0 (each)
#75	34.625
#76	72.625
#77	134.75
#78	221.375
#79	309.75
#80	415.75
#81	614.875
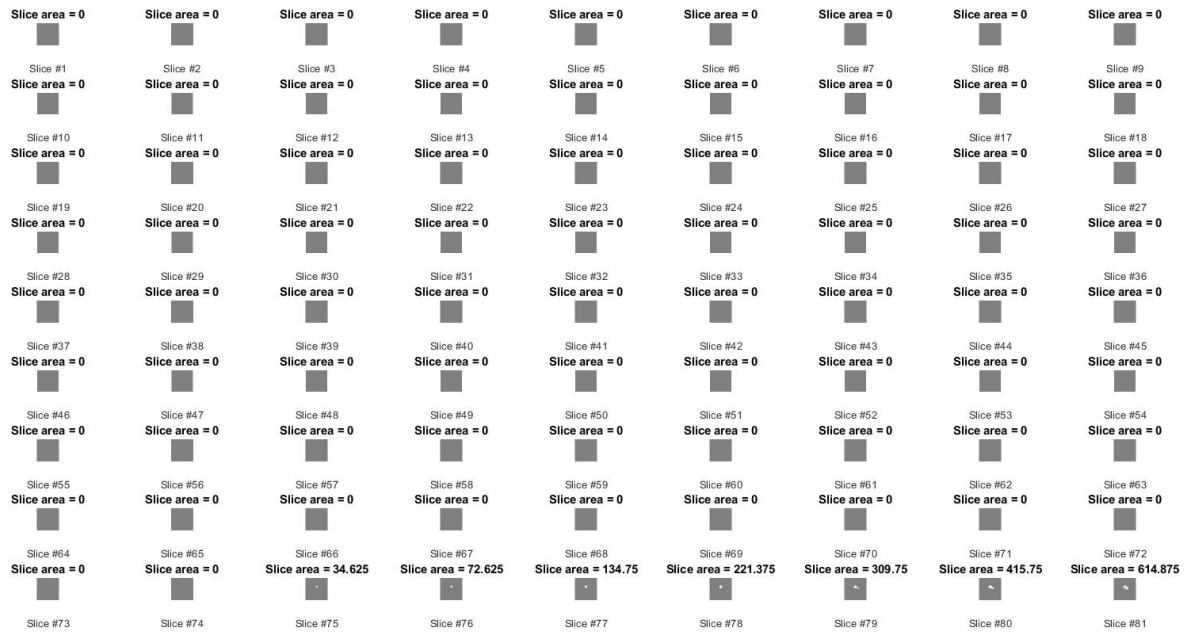
Figure 4.74. Area calculation of ground truth labels for the fourth image(slices from 1 to 81)

Slice	Area
#82	1115.875
#83	1561.625
#84	1793.5
#85	1921.125
#86	2134.5
#87	2321.5
#88	2426.625
#89	2643
#90	2751.875
#91	2813.875
#92	2898.75
#93	2939.375
#94	2960.125
#95	2982.125
#96	2983
#97	3015
#98	3023.625
#99	3037.25
#100	3003
#101	2898.5
#102	2855.5
#103	2909.75
#104	2949.375
#105	2988.875
#106	3003.25
#107	3047.25
#108	3070.5
#109	3105.625
#110	3140.75
#111	3158.625
#112	3212.75
#113	3148
#114	3056.25
#115	2973.875
#116	2932.75
#117	2849.625
#118	2716.75
#119	2624.25
#120	2525.25
#121	2427.5
#122	2319.75
#123	2246.125
#124	2142.125
#125	2053.25
#126	1973.375
#127	1875.75
#128	1794
#129	1704
#130	1577.375
#131	1520
#132	1419.875
#133	1346.5
#134	1200.75
#135	971.5
#136	747.75
#137	638.125
#138	489.625
#139	155.75
#140	79.5
#141–#155	0 (each)

Figure 4.75. Area calculation of ground truth labels for the fourth image(slices from 82 to 155)

Surface area calculation for the fourth test image was also applied to obtain the volume of the real tumor. According to Figure 4.74 and Figure 4.75, ground truth labels that indicate the original tumor existence are shown between slices # 75 and #140.
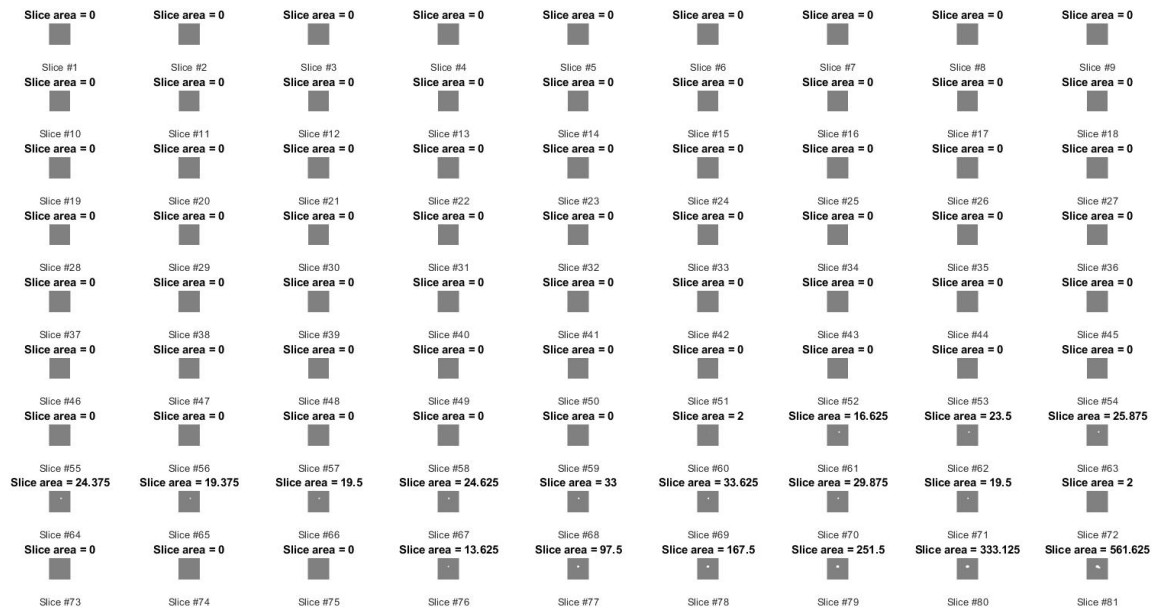
Figure 4.76. Area calculation of predicted labels for the fourth image (slices from 1 to 81)
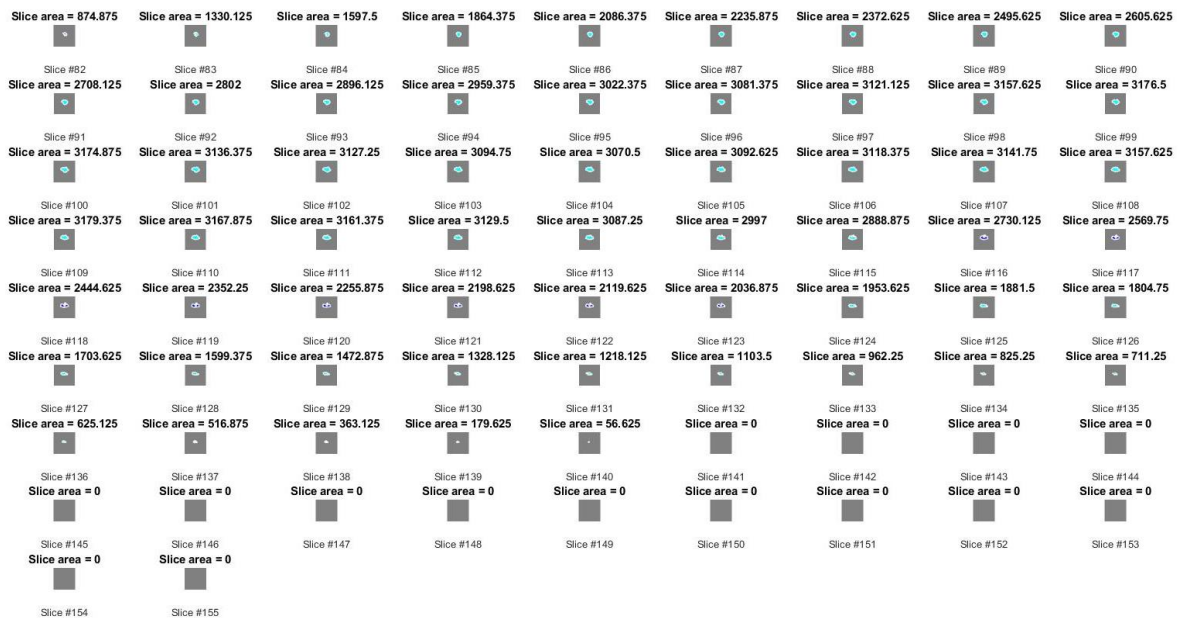
Figure 4.77. Area calculation of predicted labels for the fourth image (slices from 82 to 155)

Predicted labels which represent the prediction of tumor existence with the proposed method is shown in Figure 4.76 and 4.77. Even though there are some false predictions compared to ground truth labels, it is quite efficient to determine the volume of the tumor closed to the original image.

Figure 4.78. Area calculation of the brain for the fourth image (slices from 1 to 81)
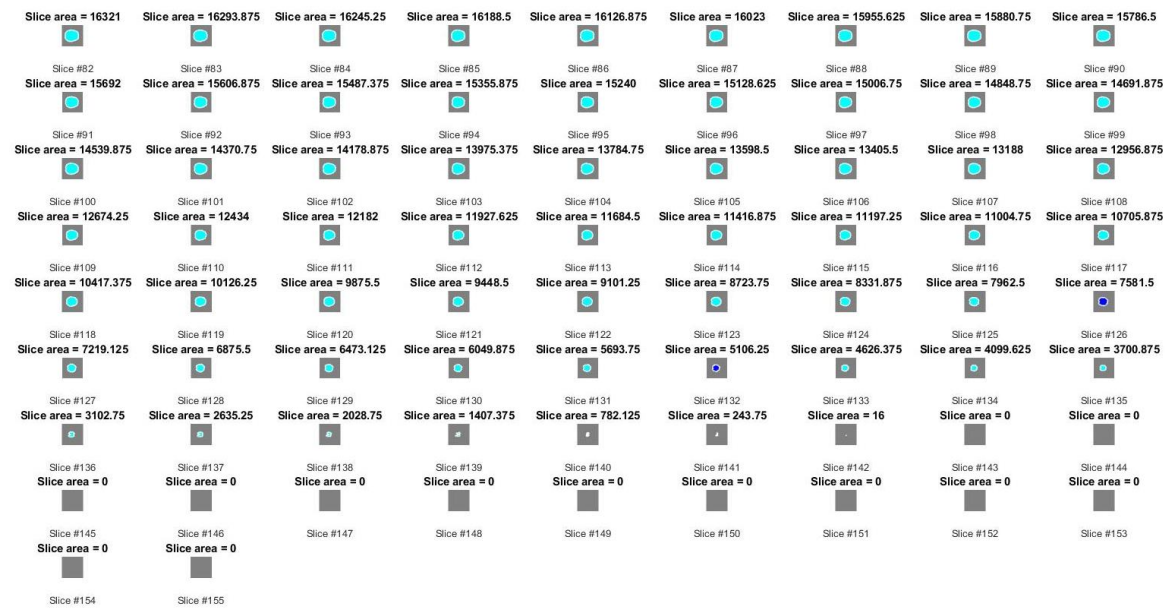
Figure 4.79. Area calculation of the brain for the fourth image (slices from 82 to 155)

In Figure 4.78 and Figure 4.79, surface areas of brain slices for the fourth test image to obtain the volume are presented.
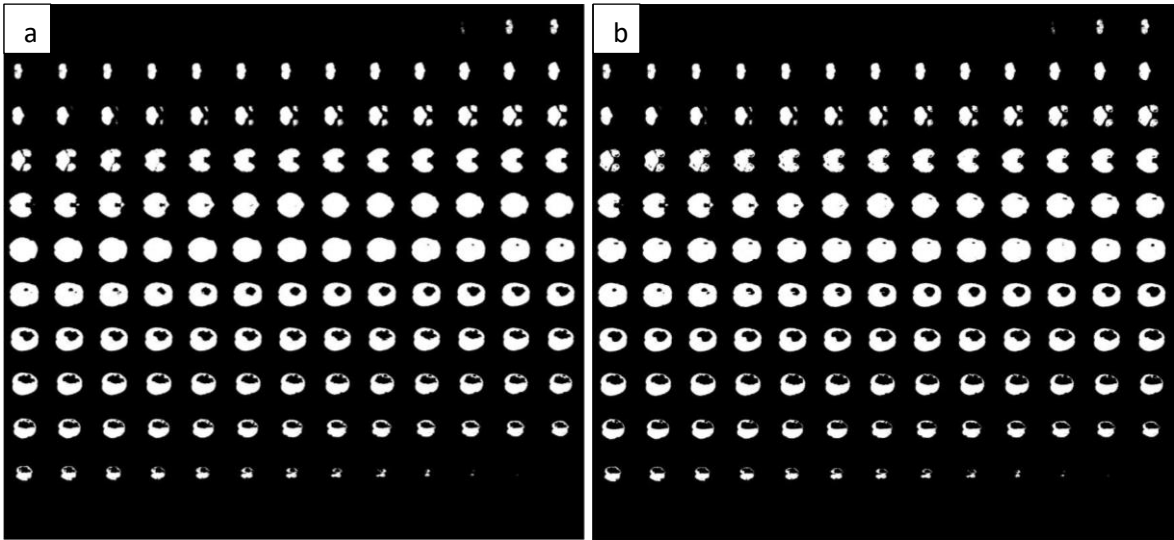
Figure 4.80. Label insertion into the segmented brain images for the fourth image,
a) ground truth, b) predicted
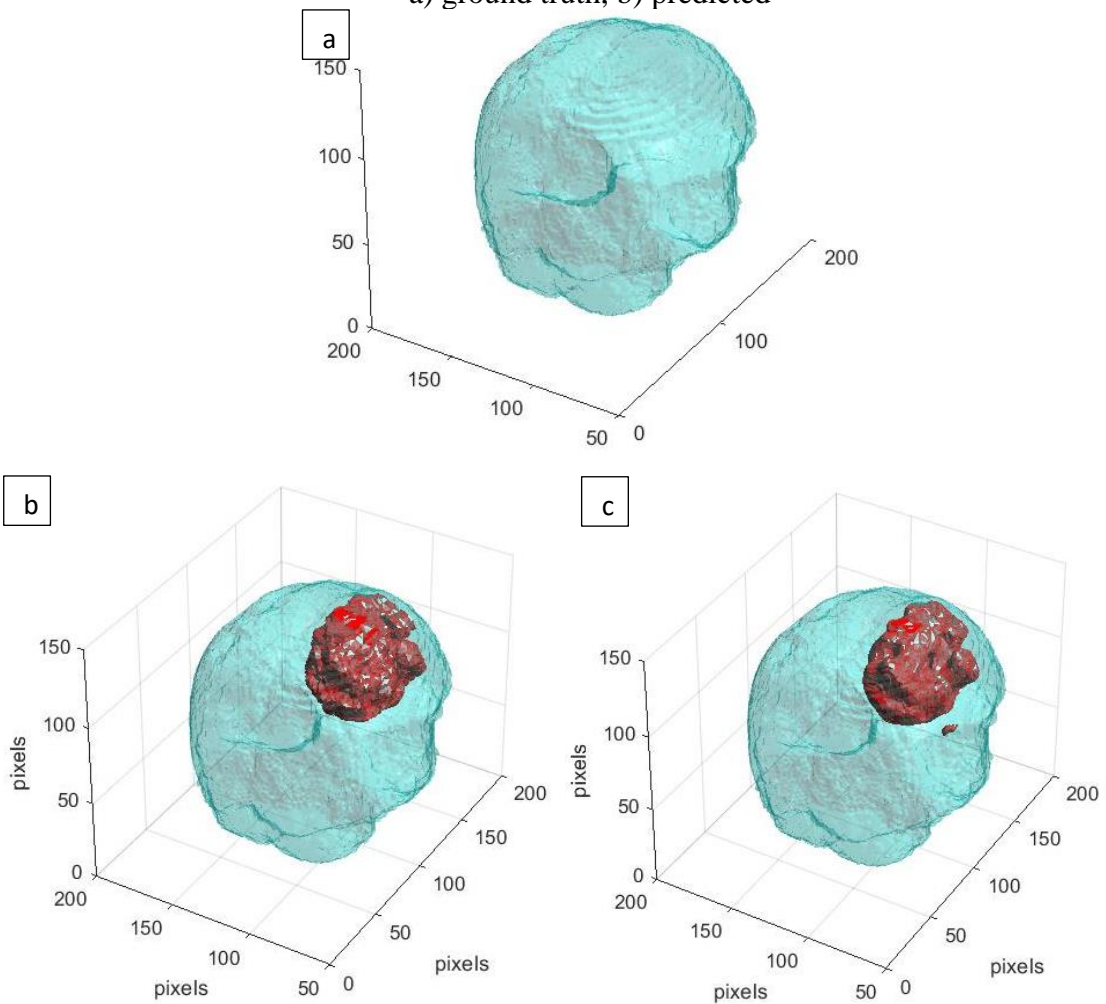
Figure 4.81. 3D imaging by using segmented brain and label images for the fourth image,
a) whole brain, b) brain with ground truth and c) brain with predicted labels
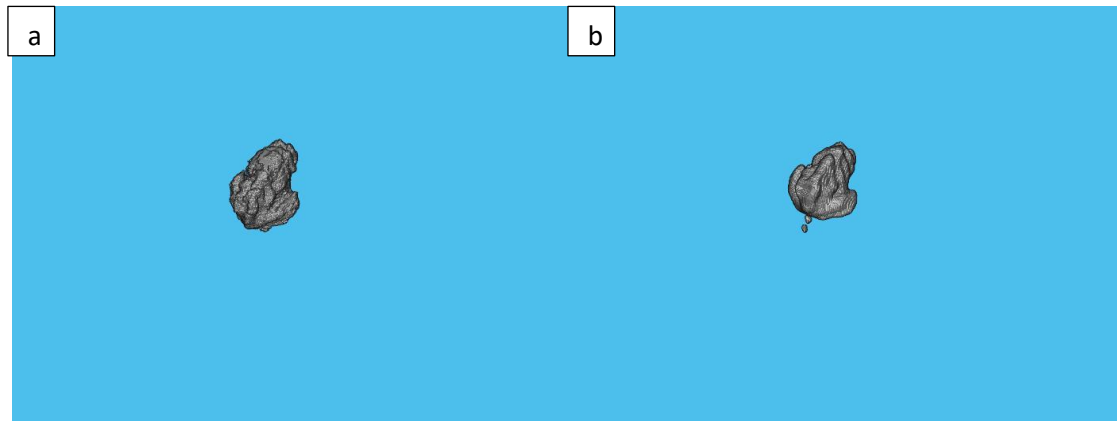
Figure 4.82. Brain tumor extraction in 3D for the fourth image, a) tumor with ground truth labels, b) tumor with predicted labels

5.DISCUSSION

This method is advantageous since it provides precise measurements of the tumor's diameter, height, and depth. When comparing the findings of reference studies to our suggested study, Table 5.1 demonstrates that our methodology has a substantial F-score when compared to other methodologies. Despite the fact that our accuracy ratio is reasonable, it might be increased with more memory space or the use of an external GPU device.

Our approach stands out because it uses a custom neural network rather than a pre-trained network. Furthermore, a contrast with the majority of similar studies reveals high tumor prediction precision and F-score ratios. Despite some memory problems, we were able to obtain these impressive results by analyzing 5 MR brain images. Our dice index numbers display expressive results in terms of evaluating the resemblance between ground truth and predicted labels, as we discussed earlier in this study. With the ability to use more memory, our system can become even more effective, allowing us to improve our segmentation metrics even further. Furthermore, 3D brain imaging with precise tumor location will help surgeons develop treatment options and extend academic studies in the field of medical imaging.

By using semantic segmentation with a deep learning network, we attempted to analyze whole-brain tumor existence. Our assessment metrics indicate that we are capable of recognizing brain tumors with remarkable precision and accuracy. In addition, 3D imaging of the brain tumor area was done using three different imaging planes. This method can be used to investigate MR brain images in a novel way.

Table 5.1. Comparison between the proposed method and other related methods

Studies	Accuracy	F- Score
Alqazzaz et al.,2019	-	0.85
Li Sun et al.,2019	0.61	0.909
Baid et al.,2020	-	0.88
Maharjana et al.,2020	0.98	-
Ataloglou,et al.,2019	-	0.90
Mathiyalagan,et al., 2021	0.98	-
Biswas,et al.,2021	-	0.942
Liu, et al., 2020	-	0.81
Biratu, et al., 2021	-	0.89
Reddy, et al., 2021	0.95	-
Baid, et al., 2017	-	0.80
Proposed method	0.957	0.93

As can be seen in Table 5.1, the results of our method are compared with several different studies regarding brain tumor prediction. In terms of calculating the accuracy, the proposed study has an accuracy ratio of around 96% which can be evaluated as efficiently as the other studies. In addition, F-score results were also compared which is beneficial to evaluate the brain tumor existence in even more detail. Our suggested method has one of the highest F-score at 0.93 among these studies. These metrics are meaningful to understand the outcome of different types of segmentation applications.

Furthermore, another application that distinguishes our study from other studies is the calculation of brain tumor volume. As mentioned in the previous section, the calculation of the brain tumor volume is obtained by calculating the surface areas of each slice in the MR images and summing them up. The total surface area provides information about the volume of the brain tumor. In addition, the comparison of the actual tumor sizes with the estimated tumor sizes and the calculation of how much of these tumors correspond to the brain make our study stand out.

There are some limitations of the proposed method. Solving the memory problem will allow working with more training data and will also allow more test images to be evaluated. At the same time, the designed deep learning network will be more detailed and contain more layers. This means that better results can be obtained at the output of the network. The proposed study correctly identified the region of tumors in the brain and was effective. In addition, the similarity rates of predicted brain tumors with real tumors were also quite accurate. However, although the detection of very small tumors was successful regarding their regions, the similarity rates of the predicted tumors and real tumors were calculated less accurately. This problem might be prevented by adding more convolution layers that contain more filters into the neural network to carry out a more detailed application. Even though there are some restrictions such as lack of memory, the suggested method has been successful in 3D imaging of brain tumors and calculating their volume. The study differs from many studies in the literature, especially in this aspect in addition to the effective results of the semantic segmentation network.

6.CONCLUSION

We introduced a new method for diagnosing whole-brain tumors and showing the exact tumor area in 3D in this study. Even though our model is highly successful at accurately predicting brain tumors in MR images, the system's efficiency can be enhanced by incorporating more class identifications to obtain more knowledge about the type of brain tumor, as well as increasing the number of training and test data to obtain more results to improve tumor prognosis. Nevertheless, supplying surgeons with a 3D model of the ground truth and predicted labels implanted in the brain will help them determine the exact region and dimensions, such as height, width, and depth.

In conclusion, the suggested approach specifies two separate types, such as 'background' and 'tumor.' Images were fed into a deep learning network using the random patch extraction process. The mean context prediction ratio was 91.718, while the mean tumor prediction ratio was 99.756. Other semantic segmentation metrics, such as mean precision, mean IoU, mean BF score, and dice index, were also used to conduct a thorough analysis. These evaluation criteria have shown positive results. Much more accurate findings can be obtained in future studies by increasing the number of test images. In addition, 3D imaging of the brain tumor was completed successfully. As a result, 3D imaging will provide a wide variety

of testing for brain tumor analysis in addition to segmentation findings. Finally, in terms of brain tumor identification and imaging, our research is very successful and promising.

To evaluate this study in general, the fact that brain tumor is a threat to human health and that it is detected with high accuracy with deep learning techniques has gained great importance in the light of technological developments in this field. Diagnosis, segmentation, and classification of brain tumors by physicians is time-consuming and mostly based on their knowledge and experience. Thanks to the advancing artificial intelligence technologies, accurate and precise diagnosis of the tumor minimize human-induced errors.

The deep learning network and semantic segmentation technique used in this study were used to detect tumors with high sensitivity, similarity, and accuracy. In addition, using segmented brain sections and predicted labels obtained at the final layer of this deep learning network, they were compared with ground truth labels, and very promising results were obtained. After comparing the similarities of these labels, they were placed in segmented brain sections. 3D visual comparisons were made with these images.

Finally, in order to obtain volumetric information, the surface areas of all sections in each MR test image were calculated and the total surface area values were obtained for the brain, ground truth labels, and predicted labels. These data were very informative about the size of the brain tumor and about the size of the brain tumor and how much of the total volume the brain occupies. As stated in the previous section, calculating the surface areas of the brain, real and predicted labels, and applying this process to all sections is very useful in terms of comparing tumor volume information. In addition, the volumetric sizes of the actual label and the predicted labels are calculated in percentage, showing how much of the brain is covered by the tumors obtained with real labels and predicted labels. As a result, the estimated volume values are very close to the actual volume values, showing that this study can determine the presence of tumors by the deep learning method and tumor size by surface area algorithm.

The motivation of this study was determined as automatic detection of tumors in the brain with high accuracy using a deep learning network. Also, calculating the volumes of brain tumors and how much these tumors correspond to the total brain volume are among other purposes of the study. This study can provide a significant advantage in brain tumor diagnosis as it enables brain tumors to be detected automatically. In addition, the calculation

of the brain tumor volume and 3D modeling will facilitate clear visualization of the tumor region and understanding the size of the tumor.

In conclusion, the application of such automatic segmentation techniques for tumor detection using deep learning networks is increasing day by day. It may be possible to further increase diagnostic accuracy by using pre-trained or hybrid networks. Creating the necessary memory space to use even more training and test image data can also have positive effects.

REFERENCES

[1] T. B. Mohamed , G. Zahia , M. Smaine , C. Stephane ve M. Mohamed , «A stochastic multi-agent approach for medical-image segmentation: Application to tumor segmentation in brain MR images,» *Artificial Intelligence In Medicine 110,* p. 101980, (2020).

[2] A. Y. A. Sabaa, T. A. Imad Fakhri ve M. Abdulrazzaq, «MRI brain tumor medical images analysis using deep learning techniques: a systematic review,» *Health and Technology,* cilt 11, p. 267–282, 2021.

[3] . J. Yeganeh, . F. Mansoor, R. Mohsen, A. Vahid ve H. A. Mohammad , «ResBCDU-Net: A Deep Learning Framework for Lung CT Image Segmentation,» *Sensors ,* cilt 21, p. 268, 2021.

[4] T. K. Aurelle , T. Daniel , K. Romanic , T. Z. Djoufack , . A. A. Ngo Mouelas ve T. René, «An optimal big data workflow for biomedical image analysis,» *Informatics in Medicine Unlocked,* cilt 11, p. 68–74, 2018.

[5] L. Geert , K. Thijs , E. B. Babak , A. A. S. Arnaud , C. Francesco , G. Mohsen , J. W.M. van der Laak, G. Bram van ve . I. S. Clara, «A survey on deep learning in medical image analysis,» *Medical Image Analysis,* cilt 42, p. 60–88, 2017.

[6] L. TRESTIOREANU, «Holographic Visualisation of Radiology Data and Automated Machine Learning based Medical Image Segmentation,» *Technology and Communication,* 2018.

[7] M. Emad , A. Ahmed , R. Yara ve H. Abdel-Rahman, «Immune system programming for medical image segmentation,» *Journal of Computational Science,* cilt 31, p. 111–125, 2019.

[8] R. C. Gonzalez ve R. E. Woods, Digital Image Processing, Pearson, 2010.

[9] A. Mumtaz , S. Le Hoang , M. Khan ve N. Thanh Tung, «Segmentation of dental X-ray images in medical imaging using neutrosophic orthogonal matrices,» *Expert Systems With Applications,* cilt 91, p. 434–441, 2018.

[10] Z. Xiaoli , L. Xiongfei ve F. Yuncong , «A medical image segmentation algorithm based on bi-directional region growing,» *Optik,* cilt 126, p. 2398–2404, 2015.

[11] E. Smistad, T. L. Falch, M. Bozorgi, A. C. Elster ve F. Lindseth, «Medical image segmentation on GPUs – A comprehensive review,» *Medical Image Analysis,* cilt 20, p. 1–18, 2015.

[12] Bahadure N, Kumar Ray A ve Pal Thethi H., «Image analysis for MRI based brain tumor detection and feature extraction using biologically inspired BWT and SVM.,» *Int J Biomed Imaging,* p. 1– 12, 2017.

[13] El-Dahshan ESA, Mohsen HM, Revett K, ve Salem A-BM, «Computer-aided diagnosis of human brain tumor through MRI: a survey and a new algorithm.,» *Expert Syst. Appl,* cilt 41, p. 26–45, 2014.

[14] Mahmoud Khaled Abd-Ellah, Ali Ismail Awad, Ashraf A.M. Khalaf ve Hesham F.A.Hamed, «A review on brain tumor diagnosis from MRI images: Practical implications,key achievements, and lessons learned,» *Magnetic Resonance Imaging,* cilt 61, p. 300– 318, 2019.

[15] Anjali Wadhwaa, Anuj Bhardwaj ve Vivek Singh Verma, «A review on brain tumor segmentation of MRI images,» *Magnetic Resonance Imaging,* cilt 61, p. 247–259, 2019.

[16] Gordillo N, Montseny E ve Sobrevilla P., «State of the art survey on MRI brain tumor segmentation,» *Magn. Reson. Imaging,* cilt 31, p. 1426–38, 2013.

[17] Maier A, Syben C,, Lasser T ve Riess C, «A gentle introduction to deep learning in medical image processing,» *Z. Med. Phys,* cilt 29, p. 86–101, 2019.

[18] Ben Rabeh A, Benzarti F ve Amiri H, «Segmentation of brain MRI using active contour model,» *Int J Imaging Syst Technol,* cilt 27, p. 3–11, 2017.

[19] Kamnitsas K, Ledig C, Newcombe V F, Simpson J P, Kane A D ve Menon D K, «Efficient multi-scale 3D CNN with fully connected CRF for accurate brain lesion segmentation,» *Med Image Anal,* cilt 36, p. 61–78, 2017.

[20] Vaishnavee K B ve Amshakala K, «An automated MRI brain image segmentation and tumor detection using SOM-clustering and proximal support vector machine classifier,» %1 içinde *IEEE Int.Conf. Engineering and Technology*, 2015.

[21] N. Sharma ve L.M. Aggarwal, «Automated medical image segmentation techniques,» *J. Med. Phys./Assoc. Med.Phys,* cilt 35, p. 3–14, 2010.

[22] W. Zhang, R. Li, H. Deng, L. Wang, W. Lin, S. Ji ve D. Shen, «Deep convolutional neural networks for multi-modality isointense infant brain image segmentation,» *NeuroImage,* cilt 108, p. 214–224, 2015.

[23] Rarasmaya Indraswari, Takio Kurita, Agus Zainal Arifin, Nanik Suciati ve Eha Renwi Astuti, «Multi-projection deep learning network for segmentation of 3D medical images».

[24] Jasmine Paul ve T. S. Sivarani, «Computer aided diagnosis of brain tumor using novel classification techniques,» *Journal of Ambient Intelligence and Humanized Computing,* 2020.

[25] A. Maharana, D. Patra ve S. Pradhan, «Robust spatial information based tumour detection for brain MR images,» *ELECTRONICS LETTERS,* cilt 56, p. 1398–1400, 2020.

[26] Van G, Robert-Jan M,, Piotr AW, Hein GB, Benno RJ, Peter O, Marc H, Matthijs O ve Pim JF, «Basic principles of magnetic resonance imaging,» *Prog Cardiovasc Dis,* cilt 42, p. 149–156, 1999.

[27] Sindhu Devunooru, Abeer Alsadoon, P. W. C. Chandana ve Azam Beg, «Deep learning neural networks for medical image segmentation of brain tumours for diagnosis: a recent review and taxonomy,» *Journal of Ambient Intelligence and Humanized Computing,* cilt 12, p. 455–483, 2020.

[28] Chen S, Ding C ve Liu M, «Dual-force convolutional neural networks for accurate brain tumor segmentation,» *Pattern Recogn,* cilt 88, p. 90–100, 2019.

[29] Kaplan Kaplan, Yılmaz Kaya, Melih Kuncan ve H. Metin Ertunç, «Brain tumor classification using modified local binary patterns (LBP) feature extraction methods,» *Medical Hypotheses,* cilt 139, 2020.

[30] Amber L. Simpson, Michela Antonelli, Spyridon Bakas, Michel Bilello, Keyvan Farahani, Bram van Ginneken, Annette Kopp-Schneider, Bennett A. Landman, Geert Litjens, Bjoern Menze, Olaf Ronneberger, Ronald M. Summers, Patrick Bilic, Patrick F. Christ, Richard K. G. , Marc Gollub, Jennifer Golia-Pernicka, Stephan H. Heckers, William R. Jarnagin, Maureen K. McHugo, Sandy Napel, Eugene Vorontsov, Lena Maier-Hein ve M. Jorge Cardoso, «A large annotated medical image dataset for the development and evaluation of segmentation Algorithms,» *Archive,* 2020.

[31] Prabhjot Kaur Chahal, Shreelekha Pandey ve Shivani Goel, «A survey on brain tumor detection techniques for MR images,» *Multimedia Tools and Applications,* cilt 79, p. 21771–21814, 2020.

[32] «https://www.mathworks.com/help/images/ref/niftiread.html,» [Çevrimiçi].

[33] L. Wang, F. Shi, G. Li, Y. Gao, W. Lin, J.H. Gilmore ve D. Shen, «Segmentation ofneonatal brain MR images using patch-driven level sets,» *NeuroImage ,* cilt 84, p. 141–158, 2014.

[34] Salma Alqazzaz, Xianfang Sun, Xin Yang ve Len Nokes,, «Automated brain tumor segmentation on multi-modal MR image using SegNet,» *Computational Visual Media,* cilt 5, p. 209–219, 2019.

[35] Li Sun, Songtao Zhang, Hang Chen ve Lin Luo, «Brain Tumor Segmentation and Survival Prediction Using Multimodal MRI Scans With Deep Learning,» *Frontiers in Neuroscience,* cilt 13, 2019.

[36] Ujjwal Baid, Sanjay Talbar, Swapnil Rane, Sudeep Gupta, Meenakshi H. Thakur, Aliasgar Moiyadi, Nilesh Sable, Mayuresh Akolkar ve Abhishek Mahajan, «A Novel Approach for Fully Automatic Intra-Tumor Segmentation With 3D U-Net Architecture for Gliomas,» *Frontiers in Computational Neuroscience.*

[37] Sunil Maharjana, Abeer Alsadoona, P.W.C. Prasada, Thair Al-Dalaina ve Omar Hisham Alsadoon, «A novel enhanced softmax loss function for brain tumour detection using deep learning,» *Journal of Neuroscience Methods,* cilt 108520, p. 330, 2020.

[38] Logeswari T ve Karnan M, «An improved implementation of brain tumor detection using segmentation based on hierarchical self organizing map,» *Int J Comput Theory Eng,* cilt 2, p. 591, 2010.

[39] «https://www.aans.org/en/Patients/Neurosurgical-Conditions-and-Treatments/Brain-Tumor,» [Çevrimiçi].

[40] «https://braintumor.org/brain-tumor-information/understanding-brain-tumors/tumor-types/,» [Çevrimiçi].

[41] Michael James Strong, Juan carlos Vera, Mansour Mathkour, Juanita Garces ve Mansour Mathkour, «Brain Tumors: Epidemiology and Current Trends in Treatment,» *Brain Tumors Neurooncol,* 2015.

[42] Soonmee Cha, «Neuroimaging in neuro-oncology,» *Neurotherapeutics,* cilt 6, pp. 465-77, 2009.

[43] Brandsma D, Stalpers L, Taal W, Sminia P ve van den Bent MJ, «Clinical features, mechanisms, and management of pseudoprogression in malignant gliomas,» *Lancet Oncol,* cilt 9, pp. 453-461, 2008.

[44] Debashis Ganguly, Srabonti Chakraborty, Maricel Balitanas ve Tai-hoon Kim, «Medical Imaging: A Review,» *SUComS,* cilt 78, p. 504–516, 2010.

[45] Webb, S, The Physics of Medical Imaging Medical Science Series, 1988.

[46] C. A. Roobottom, G. Mitchell ve G. M. Hughes, «Radiation-Reduction Strategies in Cardiac Computed Tomographic Angiography,» *Clinical Radiology,* cilt 65, pp. 859-867, 2010.

[47] K. K. Shung, M. B. Smith ve B. Tsui, Principles of medical imaging, New York: Academic Press, 1992.

[48] «http://en.wikipedia.org/wiki/Medical_imaging,» [Çevrimiçi].

[49] Sayan Kahali, Sudip Kumar Adhikari ve Jamuna Kanta Sing, «A two-stage fuzzy multi-objective framework for segmentation of 3DMRI brain image data,» *Applied Soft Computing,* cilt 60, p. 312–327, 2017.

[50] D.L. Pham, C. Xu ve J.L. Prince, «A survey of current methods medical image segmentation technical reports,» *Annu. Rev. Biomed. Eng ,* pp. 99-01, 1998.

[51] J. Nayak, B. Naik ve H.S. Behera, «Fuzzy c-Means (FCM) Clustering Algorithm: A decade Review from 2000 to 2014,» *Computational Intelligence in Data Mining,* cilt 2, p. 133–149, 2015.

[52] Toan Duc Bui, Jitae Shin ve Taesup Moon, «Skip-connected 3D DenseNet for volumetric infant brain MRIsegmentation,» *Biomedical Signal Processing and Control ,* cilt 54, p. 101613, 2019.

[53] Y. LeCun, Y. Bengio ve G. Hinton, «Deep learning,» *Nature,* cilt 521, p. 436–444, 2015.

[54] D. Shen, G. Wu ve H.-I. Suk, «Deep learning in medical image analysis,» *Annu. Rev. Biomed. Eng,* cilt 19, p. 221–248, 2017.

[55] Alexander Selvikvåg Lundervold ve Arvid Lundervold, «An overview of deep learning in,» *medical imaging focusing on MRI,* p. 26, ZEMEDI.

[56] Işin A, Direkoğlu C ve Şah M, «Review of MRI-based brain tumor image segmentation using deep learning methods,» *Proc. Comput. Sci,* p. 317–24, 2016.

[57] Mohan G ve Subashini MM, «MRI based medical image analysis: survey on brain tumor grade classification,» *Biomed. Signal Process. Control,* cilt 39, p. 139–61, 2018.

[58] Pawel Mlynarski, Hervé Delingette, Antonio Criminisi ve Nicholas Ayache, «3D Convolutional Neural Networks for Tumor Segmentation using Long-range 2D Context,» *Computerized Medical Imaging and Graphics,* cilt 73, pp. 60-72, 2019.

[59] Patterson J ve Gibson A, «Deep Learning a Practitioner's Approach,» p. 1–40, 2017.

[60] Saqib Qamar, Hai Jin, Ran Zheng, Parvez Ahmad ve Mohd Usama, «A variant form of 3D-UNet for infant brain segmentation,» *Future Generation Computer Systems,* cilt 108, pp. 613-623, 2020.

[61] Simonyan K ve Zisserman A, «Very deep convolutional networks for large-scale image recognition,» %1 içinde *ICLR*, 2014.

[62] C. Szegedy, W. Liu, Y. Jia, P. Sermanet, S. Reed, D. Anguelov, D. Erhan, V. Vanhoucke ve A. Rabinovich, «Going deeper with convolutions, in: Proceedings of the IEEE conference,» *computer vision and pattern recognition,* p. 1–9.

[63] He, Kaiming, «Deep residual learning for image recognition,» %1 içinde *IEEE Conference on Computer Vision and Pattern Recognition*, 2016.

[64] TongxueZhou, SuRuan ve StéphaneCanu, «A review: Deep learning for medical image segmentation using multimodality fusion,» *Array,* pp. 100-004, 2019.

[65] «https://www.mathworks.com/help/deeplearning/ug/layers-of-a-convolutional-neural-network.html,» [Çevrimiçi].

[66] «https://towardsdatascience.com/a-comprehensive-introduction-to-different-types-of-convolutions-in-deep-learning-669281e58215,» [Çevrimiçi].

[67] «https://towardsdatascience.com/a-comprehensive-guide-to-convolutional-neural   networks-the-eli5-way-3bd2b1164a53,» [Çevrimiçi].

[68] «https://leonardoaraujosantos.gitbook.io/artificialinteligence/machine_learning/deep_learning/pooling_layer,» [Çevrimiçi].

[69] «https://www.mathworks.com/help/deeplearning/ref/nnet.cnn.layer.batchnormalizationlayer.html,» [Çevrimiçi].

[70] «https://www.mathworks.com/help/deeplearning/ref/transposedconv3dlayer.html,» [Çevrimiçi].

[71] «https://developers.google.com/machine-learning/crash-course/multi-class-neural-networks/softmax,» [Çevrimiçi].

[72] «https://www.mathworks.com/help/vision/ref/nnet.cnn.layer.pixelclassificationlayer.html?s_tid=doc_ta,» [Çevrimiçi].

[73] Eduardo Fernandez-Moral, Renato Martins, Denis Wolf ve Patrick Rives, «A New Metric for Evaluating Semantic Segmentation,» *Global and Contour Accuracy,* 2021.

[74] M. Sokolova ve G. Lapalme, «A systematic analysis of performance measures for classification tasks,» *Inf. Process. Manag,* cilt 45, p. 427–437, 2009.

[75] G. Csurka, D. Larlus, F. Perronnin ve F. Meylan, «What is a good evaluation measure for semantic segmentation,» *BMVC,* cilt 27, 2013.

[76] «https://www.jeremyjordan.me/evaluating-image-segmentation-models/,» [Çevrimiçi].

[77] Abdel Aziz Taha ve Allan Hanbury, «Metrics for evaluating 3D medical image segmentation analysis, selection, and tool,» *BMC Med. Imaging,* cilt 15, p. 29, 2015.

[78] «https://ilmonteux.github.io/2019/05/10/segmentation-metrics.html,» [Çevrimiçi].

[79] «http://medicaldecathlon.com/.,» [Çevrimiçi].

[80] A. Hasan, F. Meziane, R. Aspin ve H. Jalab, «Segmentation of brain tumors in MRI images using three- dimensional active contour without edge,» *Symmetry,* cilt 8, p. 132, 2016.

[81] L. Tonarelli, «Magnetic Resonance Imaging of Brain Tumor,» *CEwebsource.com,* 2021.

[82] Youlian Zhu ve Cheng Huang, «An adaptive histogram equalization algorithm on the image gray level mapping,» *Physics Procedia,* cilt 25, p. 601–608, 2012.

[83] «https://www.mathworks.com/help/deeplearning/ref/trainnetwork.html,» [Çevrimiçi].

[84] «https://www.mathworks.com/help/deeplearning/ug/monitor-deep-learning-training-progress.html,» [Çevrimiçi].

[85] «https://towardsdatascience.com/stochastic-gradient-descent-clearly-explained-53d239905d31,» [Çevrimiçi].

[86] «https://en.wikipedia.org/wiki/Stochastic_gradient_descent,» [Çevrimiçi].

[87] «https://www.mathworks.com/help/deeplearning/ref/nnet.cnn.trainingoptionssgdm.html,» [Çevrimiçi].

[88] Zhiqiang Liu, Paul Chow, Jinwei Xu, Jingfei Jiang Yong Dou ve Jie Zhou, «A uniform architecture design for accelerating 2D and 3D CNNs on FPGAs,» *Electronics,* cilt 8, p. 65, 2019.

[89] Aykut Erdamar ve Mehmet Feyzi Aksahin, «Multi- scale classification of single-cell gel electrophoresis assay usingdeep learning algorithm,» *Biomed. Signal Process. Control,* cilt 56, p. 101672, 2020.

[90] «https://medium.com/analytics-vidhya/downsampling-and-upsampling-of-images-demystifying-the-theory-4ca7e21db24a,» [Çevrimiçi].

[91] Abdou Youssef, «Image Downsampling and Upsampling Methods,» *National Institute of Standards and Technology.*

[92] Gabriel Jim´enez ve Daniel Racoceanu, «Deep learning for semantic segmentation vs. classification in computational pathology: application to mitosis analysis in breast Cancer grading,» *Front. Bioeng. Biotechnol,* cilt 21, p. 145, 2019.

[93] V.K. Devika, V. Meena ve S. Sindhu Ramachandran, «Semantic Segmentation of Brain Tumor from MRI Images,» *IEEE,* 2021.

[94] «https://www.mathworks.com/help/images/ref/bwarea.html,» [Çevrimiçi].

[95] Gomathi Mathiyalagan, Dhanasekaran Devaraj, A machine learning classification approach based glioma brain tumor detection, Int J Imaging Syst Technol., ,p.1–13, 2021

[96] Ankur Biswas, Paritosh Bhattacharya, Santi P. Maity & Rita Banik, Data Augmentation for Improved Brain Tumor Segmentation, IETE JOURNAL OF RESEARCH, 2021

[97] Hong Liu, Haichao Cao, Enmin Song, Guangzhi Ma, Xiangyang Xu, Renchao Jin, Tengying Liu, Lei Liu and Daiyang Liu, A new data augmentation method based on local image warping for medical image segmentation, Med. Phys. 48 2021

[98] Erena Siyoum Biratu , Friedhelm Schwenker , Taye Girma Debelee , Samuel Rahimeto Kebede, Worku Gachena Negera and Hasset Tamirat Molla, Enhanced Region Growing for Brain Tumor MR Image Segmentation, J. Imaging, 7, 22., 2021

[99] A. Srinivasa Reddy, P. Chenna Reddy, MRI brain tumor segmentation and prediction using modified region growing and adaptive SVM, Soft Computing 25:4135–4148, 2021

[100] Ujjwal Baid, Shubham Talbar, S. N. Talbar, Novel Approach for Brain Tumor Segmentation with Non Negative Matrix Factorization, IEEE, 2017

[101] Hafiza Iqra Javaid, Asra Roheen and Farjad Afzal, Anatomy and Physiology of Brain in Context of Learning: A Review from Current Literature, Biomed J Sci & Tech Res, 26, 2020

[102] «https://mayfieldclinic.com/pe-anatbrain.htm»

[103] «https://en.wikipedia.org/wiki/Human_brain»

[104] «https://www.kenhub.com/en/library/anatomy/normal-brain-mri»

[105] Matthias Rottmann, Kira Maag, Robin Chan, Fabian Huger, Peter Schlicht, Hanno Gottschalk, Detection of False Positive and False Negative Samples in Semantic Segmentation, 2019